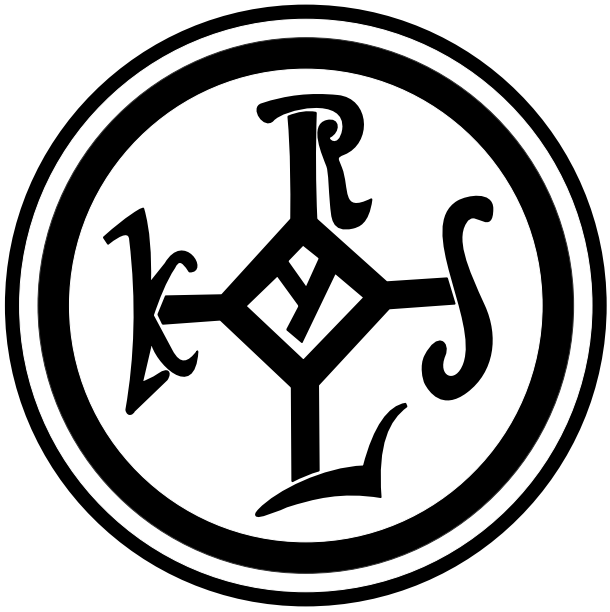

RWTH AACHEN

III. PHYSICS INSTITUTE A

OCTOBER

2005

Search for Excited Muons in $p\bar{p}$-Collisions at $\sqrt{s}$=1.96 TeV

von

Jan Willem Coenen

Diplomarbeit in Physik

vorgelegt der

Fakultät für Mathematik, Informatik und Naturwissenschaften
der Rheinisch-Westfälischen Technischen Hochschule Aachen

im
Oktober 2005

angefertigt im

III. Physikalischen Institut A

bei

Prof. Dr. Thomas Hebbeker

TO MY MOTHER
Helga E. Coenen
† 13.10.2004

ABSTRACT

The first search for single excited muon production at the DØ-Experiment is performed since the beginning of the Run II period. The search is focused on production via contact interactions and the final state $\mu\mu\gamma$ is considered to be the dominant one. Mass limits are determined, based on the theoretical, k-factor corrected, leading order cross section from `Pythia`. Run II data collected from April 2002 to August 2004 are analyzed, representing an integrated luminosity of $\mathcal{L}$= (377 $\pm$ 24) pb^{-1}. Since no excess is observed in data, lower limits on the excited muon mass are calculated. We exclude at 95% CL masses below $m_{\mu^*} = 696$ GeV, assuming that the scale parameter Λ equals m_{μ^*}.

Contents

Chapter 1

Introduction

Ever since sentient human beings began exploring the world, curiosity was one of their most powerful stimuli. In modern science this has not changed at all. In this ongoing exploration high energy physics tries to decipher the origin of matter and its structure down to the smallest scale.

The goal of particle physics is not only to decipher the structure of the fundamental particles and the interactions betweens them, but also to get a better understanding of the universe itself. The last hundred years brought improvement in this understanding of unexpected extent, especially the progress in quantum mechanics as well as the technological improvements such like modern computing tools and accelerator technology caused a huge leap forward. Today, our knowledge about the structure of matter is combined in the Standard Model of particle physics (SM) which evolved from a very intense dialog between theory and experiment.

When, in the beginning of the last century, one finally established the old greek idea of the so called atoms, the door for new discoveries was being pushed wide open. The atom as the smallest constituent of matter and the first theories describing its properties evolved very soon into very complex theories leading to more general approaches in particles physics, introducing quantum physics and a stringent theory of electromagnetic and weak force. Years later quarks were discovered as the fundamental building blocks of matter and the carriers of the electromagnetic, weak and strong force are the massless photon, the massive W and Z bosons and eight massless gluons, respectively.

The electromagnetic and weak force are combined into the electroweak gauge field theory. The quantum chromodynamics (QCD) gauge field theory is nowadays accepted as the theory of strong interactions and even though the Standard Model has proven experimentally its tremendous reach in tests with colliding electron-positron (e^+e^-), electron-proton (ep) and proton-anti proton ($p\bar{p}$) beams, giving complementary contributions, there is still more to discover.

The Z mass for example has been measured at the Large Electron-Positron storage ring (LEP) at CERN (Centre Européenne pour la Recherche Nucléaire) giving a Z mass of 91.1876 ± 0.0021 GeV [81].

Also QCD predictions have been thoroughly tested by measuring the running of the strong coupling α_s at LEP and at the Hadron-Elektron Ring Anlage (HERA) in Hamburg. The proton structure is being probed to the shortest accessible distances using ep collisions at HERA. The Standard Model of Particle Physics (SM) has successfully predicted the τ-neutrino, discovered in July 2000 and the top quark in 1995, both at the Fermi National Laboratory.

All these fact show the success of the Standard Model while there are still unresolved problems and not understood facts.

There is no explanation for the wide range of masses of the leptons and quarks for example:
From less than $1\ eV$ for neutrinos to $\approx 178\ GeV$ for the top quark [83]. Also the origin of the masses themselves is not yet understood and the concepts of the family structure of the basic fermions lacks a meaningful explanation. Another unsolved riddle is the excess of matter over antimatter in our universe. CP (charge conjugation, parity) violating processes are not enough to account for this excess.

Finally, the question of hierarchy between the scale of electroweak physics and the scale of gravity is still unanswered and gravity is far away from being brought close to the other forces, but steps in the direction of a grand unification of all fundamental forces are today underway. Many modern theories like supersymmetry, compositeness models or string theory try to explain some of these aspects but still lack any satisfying solution.

This analysis utilizes data from the DØ experiment at the Tevatron collider at Fermilab near Chicago, USA.

The Tevatron collides protons and anti-protons at a center of mass energy of $\sqrt{s} = 1.96\ TeV$ at a frequency of about 1.7 MHz. Multi-purpose detectors like DØ and the Collision Detector Facility (CDF) provide a precise measurement of leptons as well as hadronic showers, usually called jets. About $380\ pb^{-1}$ of data are analyzed to search for excited muons. These particles appear in some of the possible extensions of the SM, which describes leptons as point like particles. In a compositeness model this concept of point like leptons is abandoned, new strong interactions and constituents of leptons are postulated.

These excited states are assumed to be unstable and therefore decay into ordinary fermions and bosons, which then can be detected with the normal means of the DØ detector. In this analysis the focus is laid on the dimuon+photon signal channel, an electroweak decay channel of the Excited Muon.

Chapter 2 gives an introduction to the theoretical foundations and Standard Model physics, followed by a description of the Tevatron accelerator and the DØ detector in chapter 4. In chapter 5 the properties of Excited Muons are discussed.

While chapter 6 gives an overview of the Monte Carlo simulations for SM backgrounds and the excited muon signal as well as the implementation of excited muons into the event generator `Pythia`, the dataset and selection steps are summarized in chapter 7.

Corrections and systematic uncertainties are described in chapter 8.

Finally, chapter 10 presents the results of the search for these new particles, showing results on the cross section $\times$ branching ratio and evaluating a mass limit.

The analysis is summarized in chapter 11 together with an outlook on current and future analyses.

Chapter 2

Theoretical Foundations

This chapter introduces the use of natural units and explains abbreviations used throughout this document and introduces the Standard Model of particle physics. In the last part an overview on some properties of proton anti-proton collisions is given, as well as an introduction of the interesting kinematic variables.

2.1 Natural Units and Conventions

For reasons of simplicity high energy physics usually uses “natural units”.

In this system the two fundamental constants

$$c = 2.9979 \cdot 10^8 \frac{m}{s} \quad \text{and} \quad \hbar = \frac{h}{2\pi} = 1.054571596 \cdot 10^{-34} Js$$

are set to one:

$$c = \hbar = 1 \qquad \text{resulting in: } [length] = [time] = [energy]^{-1} = [mass]^{-1}$$

The mass (m) of a particle therefore is identical to its rest energy (mc^2) and its inverse Compton wavelength (mc/$\hbar$), showing once more the relevance of special relativity,

$$E = mc^2.$$

This Thesis will use the usual conventions of relativistic physics, introducing the metric tensor as $g^{\mu\nu} = g_{\mu\nu}$, with the Greek indices running over 0, 1, 2, 3 or t(time), x y z (space). γ^μ represents the gamma matrices with $\mu = 0, ..., 3$. Also implicitly used in some cases is the summation convention, meaning the summation of repeated indices in all cases.

As an example for a particle with mass m one can write the energy momentum relation:

$$p^2 = p^\mu p_\mu = E^2 - |\vec{p}|^2 = m^2.$$

Mostly both, particles and anti particles will be denominated with the name of the corresponding particles, special indices showing the respective charge are omitted. For example $Z^0 \to \mu^+\mu^-$ is written as $Z \to \mu\mu$.

2.2 The Standard Model

Even though this analysis goes beyond the borders of the Standard Model of Particle physics it is still the fundamental theory from which to start, hence has to be explained in some detail. In this section a short overview will be given about the fundamental constituents of matter and the interacting forces as well as a short insight into the huge relevance of the Standard Model SM. Since this analysis is concerned with the potential substructure of the fundamental particles, the theory is more or less described from the particle's point of view, even though the fundamental language describing the SM is the description via a gauge theory. One generally differentiates between fermions and bosons, spin-1/2 particles and Spin-1 particles.

Gauge Theories One of the most powerful theoretical concepts, concerning the explanation of conserved properties like momentum, angular momentum and energy was formulated by Emmy Noether(1882-1935). She connected in general invariances and conservation of certain properties. That is, the Noether Theorem: For every invariance of the Lagrangian under a global symmetry transformation $U(\alpha) = e^{i\alpha}$ there is a conserved quantity.

All fundamental particles and forces are described by gauge theories based on local gauge invariances, described with an $\alpha(x)$. The phase is now depending on time and space. As one will see in the case of the electroweak and strong theory, they can all be explained via this approach, introducing special groups and therefore quantities (like e.g. isospin), which correspond to the generators of the corresponding group.

2.2.1 The Reach of the Standard Model and "Beyond"

The Standard Model of Particle Physics tries to bring order in to the very large number of particles and the theories describing the interaction between them. This very detailed model describes particle production and decay at very different energies and scales. It is delivering a description of processes very close to the beginning of the universe as well as processes concerning "simple" excited atom states.

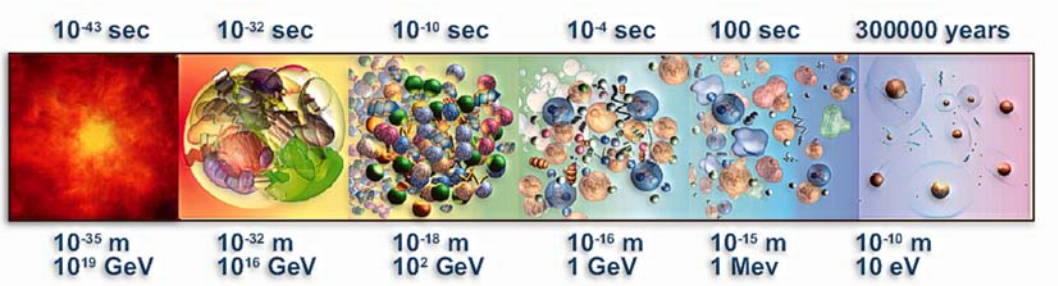

Figure 2.1: Scales through time [84]

The Evolution of the Universe and High Energy Physics Without going into detail one can easily see from Fig. 2.1 how large the scale of the SM or in the end a "Unified Theory" has to be, to describe the scale of around $10^{-35}\ m\hat{=}10^{19}\ GeV$ at $10^{-43}\ s$ after the BIG BANG to about eV relevant for nuclear physics and chemistry.

Modern High Energy Physic tries to probe as much of these energy regions as possible and unify (Fig. 2.2) the different forces.

Modern colliders like the Tevatron and the LHC with high "Center of Mass" energies ($2 \cdot 10^3\ GeV - 14 \cdot 10^3\ GeV$) can reach into physical environments similar to those, which were present only picoseconds after the Big Bang. Therefore these accelerators represent some of the most powerful instruments for acquiring knowledge of fundamental physics.

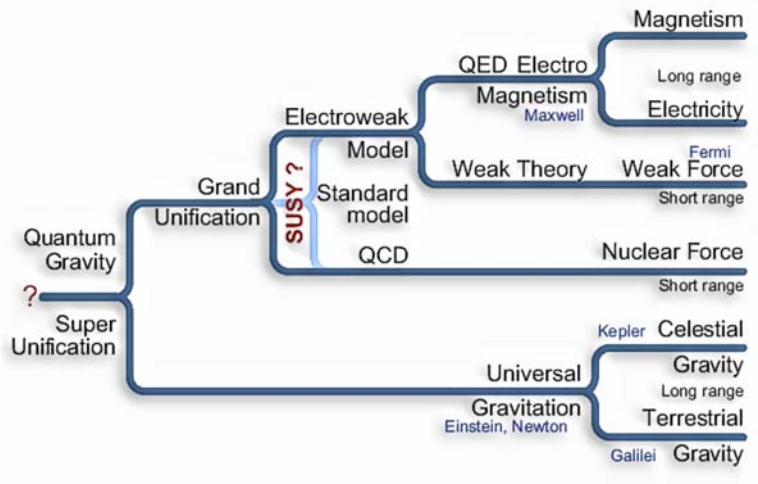

Figure 2.2: The final goal, Theory of Everything [84]

One can not only check the properties described by the SM and compare them to the actual measured values, but one can try to reach beyond this description and maybe find new and better ways to overcome certain problems of the SM mentioned above, like e.g. mass hierarchy, family structure matter anti-matter ratio and more.

The final goal is to unite all forces (sect. 2.2.3) including gravity and to find a theoretical description, as one might say: the "Theory Of Everything". The unified force would then include short ranged interaction like the weak force as well as long ranged interactions in particular gravity (Fig. 2.2).

2.2.2 Fundamental Constituents of Matter

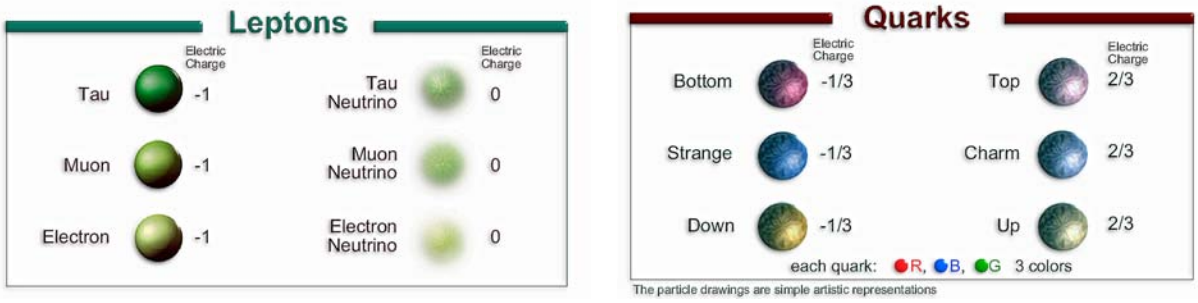

Figure 2.3: Fundamental particles, left: leptons[84] right: quarks[84]

Today two kinds of fundamental particles are known in the Standard Model. Beyond these leptons and quarks no further substructure has yet been found. Leptons like the electron can exist as free particles, but quarks are constituents of hadrons.

Leptons

Leptons are six point-like spin-$1/2$ particles, organized in three generations or families (Fig. 2.3). The first generation consists of the electron (e) and the electron neutrino (ν_e). The second and third containing the muon (μ), tau (τ) and their respective neutrinos. Each family can be categorized by a lepton quantum number: $L_e,\ L_\mu\ and\ L_\tau$. For any particle there exists an anti-particle with the same mass and spin, but opposite sign of all internal quantum numbers like e.g. charge.

Table 2.1 shows the basic properties of these leptons and their corresponding anti-particles, as well as the forces throgh which they interact. There are some other interesting properties including the parity, which

	first generation		second generation		third generation	
	e	ν_e	μ	ν_μ	τ	ν_τ
Mass[MeV][54]	0.511	<3 eV	105.66	<0.19	1776.99	<18.2
Spin	1/2	1/2	1/2	1/2	1/2	172
Charge[e]	-1	0	-1	0	-1	0
L_e	1	1	0	0	0	0
L_μ	0	0	1	1	0	0
L_τ	0	0	0	0	1	1
Lifetime [54]	∞	∞	2.197µs	∞	2.91fs	∞
Interact. Forces	EM,Weak	Weak	EM,Weak	Weak	EM,Weak	Weak

Table 2.1: Lepton properties

describes the behavior of a system under inversion, ($\vec{x} \rightarrow -\vec{x}, t \rightarrow -t$) as well as the helicity which describes the alignment between the spin and the direction of motion, + for parallel alignment - for anti-parallel. Particles with helicity + are called “right-handed” and particles with helicity - are “left-handed”. These properties are especially important for leptons since it is known that the weak interaction violates the conservation of parity and that all neutrinos are “left-handed”.[1]

Other quantum numbers for leptons include :

- Weak Isospin(T), with 3rd component T^3
  - Left handed leptons: $T = 1/2$
  - Right handed leptons:$T = 0$
- Weak Hypercharge(Y)
  - Left handed leptons: $Y = -1$
  - Right handed leptons:$Y = -2$

The 3rd component of the weak isospin is different for example electron (-1/2) and neutrino (1/2). Both quantities (T and Y) are connected through the electric charge with $Q = T^3 + Y/2$. Those quantum numbers, even though some of them, like the electric charge were known long before any coherent description was found, arise from invariances under certain transformations, and which is described by group theory. The charge Q for example is invariant under transformations of the U(1) group.

One particularly interesting class of leptons are the neutrinos. If neutrinos were to be massless, the lepton number conservation would be realized in all interactions, but recent experiments like Super-Kamiokande[10] have shown that neutrinos must have a mass, since they tend to oscillate between the different generations. Therefore Lepton family number conservation is not realized in weak interactions.

[1] Helicity is only equivalent to chirality for massless particles

Quarks

Quarks as mentioned before have never been observed as a free particle and exist only as constituents of hadrons like the proton and neutron, which together with the leptons are the constituents of the known matter.

Similar to leptons quarks exist in six flavors, ordered in three generations or families. The first one comes with the quark flavors up (u) and down (d), the second consists of charm (c) and strange (s) and the third one of top (t) and bottom (b) quark. Quarks as fermions have also spin-1/2 and their charge is n/3 depending on the quark flavor. Quarks interact via electromagnetic, weak and strong interaction.

One important property of these quarks is the violation of the flavor quantum number in weak interactions. Quarks can mix in between their flavors (their mass eigenstates do not fall together with their flavor eigenstates) which is described by the CKM[2]-matrix.

The basic properties of quarks can be found in Table 2.2.

Quark	Mass[MeV][54]	Spin	Charge[e]
d	4-8	1/2	-1/3
u	1.5-4	1/2	+2/3
s	80-130	1/2	-1/3
c	1150-1350	1/2	+2/3
b	4100-4400	1/2	-1/3
t	174300±5100	1/2	+2/3

Table 2.2: Quark properties, including the inferred bare mass of the quarks.

Like the Leptons quarks have several quantum numbers such as weak isospin and hypercharge, related through $T^3 = Q - Y/2$. The values of the quantum numbers depend on whether the quark is left or right handed.

In contrast to the leptons, quarks have an additional quantum number connected to the strong force, the color charge. This color is necessary to explain that:"Quarks do not exist as 'free' particles".

This property is known as the quark confinement.

There are three different color charges: **red**, **green** and **blue**. Since quarks can never be observed as free particles they only exist in two types of hadrons, mesons and baryons,which consist of two or three quarks respectively, in a way that the final object is colorless. There is no such thing like a free and colored particle. Because of this, the bare masses in Tab. 2.2 are inferred masses based on the quarks' influence on hadrons. Only the mass of the top-quark can be directly measured since this quark is so heavy that it decays before being bound into a hadron. The top's mass can be measured from its decay products.
A typical baryon is a proton consisting of (uud). One quark would be red, another green and the last blue. A typical meson for example is the π^+ ($u\bar{d}$) with a mass of ∼139.6 MeV and opposite colored quarks (red and anti-red). One interesting thing about hadrons is that, since they are bound states, there are excited states. While the π^+ is denoted with $J^P = 0^-$, where J is the total angular momentum and P the Parity, there is also a state $J^P = 1^-$ of ($u\bar{d}$). This particle is called the ρ and has a mass of about ∼700 MeV.
These excited states are not unique to the u$\bar{d}$- configuration, there also exist excited states of the (uud) bound state, one might say an excited proton.

[2]Cabbibo Kobayashi Maskawa (1963,1973)

Summary: Fundamental Fermions

Generations 1	2	3	T	T^3	Q	Y
Leptons						
$\begin{pmatrix} \nu_e \\ e \end{pmatrix}_L$	$\begin{pmatrix} \nu_\mu \\ \mu \end{pmatrix}_L$	$\begin{pmatrix} \nu_\tau \\ \tau \end{pmatrix}_L$	$1/2$	$+1/2$ $-1/2$	-1 0	-1
e_R	μ_R	τ_R	0	0	-1	-2
Quarks						
$\begin{pmatrix} u \\ d \end{pmatrix}_L$	$\begin{pmatrix} c \\ s \end{pmatrix}_L$	$\begin{pmatrix} t \\ b \end{pmatrix}_L$	1/2	$+1/2$ $-1/2$	$+2/3$ $-1/3$	$1/3$
u_R	c_R	t_R	0	0	$+1/3$	$+2/3$
d_R	s_R	b_R	0	0	$-1/3$	$-2/3$

Table 2.3: Summary of weak isospin, electric charge and weak hypercharge for the fundamental fermions.

As is obvious, one can understand leptons and quarks as fundamental fermions, with similar properties like weak isospin and hypercharge, both come in flavors and are ordered in families with a distinct mass hierarchy (Tab. 2.1-2.3). There are properties which need to be explained, going beyond the SM. Are there really no "right-handed neutrinos" (do neutrinos have mass?), but up type quarks? And what is the reason for the mass hierarchy? The question of hierarchy will be addressed later on in Section 5, where one possible explanation, the compositeness of fundamental fermions is introduced. Like the prediction of quarks lead to a stringent theory of hadrons, explaining the observed patterns of hadrons(e.g. masses, spin, charge and more), a new substructure might lead to a further understanding of matter.

2.2.3 Gauge Bosons and Forces

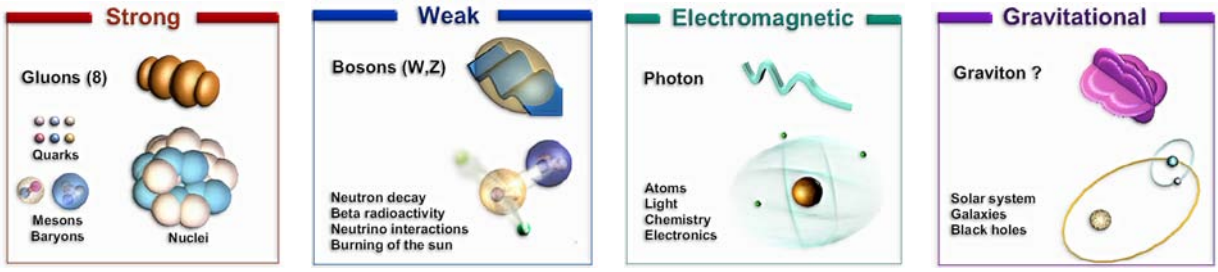

(A) (B) (C) (D)

Figure 2.4: A simple representation of the four basic forces and their carriers: Strong Force(QCD) (A), Weak Force (B), Electromagnetic Force (C), Gravitation (D) [84]

The four forces (2.4) manage the interaction between subatomic particles like quarks and leptons. Even though the SM describes only the weak, the electromagnetic and the strong interactions it is necessary in the end to introduce the gravitation for a complete description of physics.

In the theory gravity becomes comparable in strength as it approaches the "Planck Scale", which, unfortunately, is based on assumptions as to how gravity works over short distances. The "Planck Scale" ($10^{19}\ GeV$ and $10^{-35}\ m$) is out of experimental reach of particle accelerators, which currently achieve 100 - 1,000 GeV, in which case gravity is still negligible.

Each of these forces is mediated by a carrier (Fig. 2.4(A)-(D)), named gauge boson (from gauge theories). The bosons have spin 1 and their masses reach from the massless Photon (γ) to the three heavy gauge bosons of the weak force $W^{\pm}$ and Z. The strong interaction is mediated through massless gluons. The $SU(3)_C$ symmetry group, forms nine color eigen-states: One "color-octet" and one "color-singlet". These states lead to the eight gluons (from the octet), distinguished by their color-charge:

$$r\bar{g}, r\bar{b},\ b\bar{g}, b\bar{r}, g\bar{r},\ g\bar{b},\ \frac{1}{\sqrt{2}}\left(r\bar{r} - b\bar{b}\right), \frac{1}{\sqrt{6}}\left(r\bar{r} + b\bar{b} - 2g\bar{g}\right)$$

The last, 9th, singlet state $\frac{1}{\sqrt{3}}\left(r\bar{r} + b\bar{b} + g\bar{g}\right)$ seems not to be realized in nature, since a colorless free gluon has not been observed [11]. The undiscovered carrier of the fourth force, gravitation, is called "graviton". Since it has not yet been discovered it remains a theoretical concept.

The different properties of the gauge bosons can be found in Tab. 2.4. With these gauge bosons and

	γ	W	Z	g
Force	Neutral EM	Charged Electroweak	Charged Electroweak	Strong
Mass[GeV][54]	$< 6 \cdot 10^{-26}$	80.425 ± 0.038	91.1876 ± 0.0021	0
Lifetime τ[s][11]	∞	$\sim 3 \cdot 10^{-25}$	$\sim 3 \cdot 10^{-25}$	∞
Spin	1	1	1	1
Charge[e]	0	1	0	0

Table 2.4: Summary for the gauge bosons quantities, including mass, and lifetime τ

the forces they mediate one now has a handle to describe the processes of the SM, from the only weakly interacting neutrinos, the electroweak interacting leptons to hadronisation (sec. 3.1.2) processes involving quarks interacting strong, electromagnetic and weak.

Even we are representing a search for excited leptons, a short introduction into Quantum Chromodynamics, the theory of the strong interaction, and into the electroweak theory will be given, since they play an important role in colliding beam experiments.

Quantum Chromodynamics (QCD)

Quantum Chromodynamics is a "non-Abelian" gauge theory describing the strong interaction of quarks, their asymptotic freedom and confinement.

The interactions between two quarks can be approximately described by a potential [11] of the form:

$$V(r) = -\frac{4\alpha_s}{3r} + F \cdot r \tag{2.1}$$

α_s is the strong coupling constant and r is the distance between the two quarks.

As one can see directly from Eq. 2.1, the potential energy increases with the distance, leading to the domination of the last term at distances of about $1fm$, causing the quarks to hadronize: a new quark anti-quark pair is produced. The $SU(3)_C$ is non "abelian" ,the gluons, the carriers of the strong force can, due to their own color-charge, interact with each other.

This is one of the most astonishing aspects of the QCD, it explains why quarks are never found free or in colored combinations, but only in colorless hadrons.

The gluon gluon interaction also influences the strong coupling constant α_s, as it is this self interaction which causes the " running of α_s, i.e. the coupling's dependence on the energy scale ς at which it is used [11]:

$$\alpha_s(\varsigma) = \frac{\alpha_s(\varsigma_0)}{1 - \beta_0^s \cdot \alpha_s(\varsigma_0) \cdot ln(\varsigma^2/\varsigma_0^2)} \tag{2.2}$$

Here $\alpha_s(\varsigma_0)$ represents the value of α_s at a reference scale. One knows that for the QED (Sec. 2.2.3) a similar running is caused by vacuum polarization effects. The difference here is, that the self interacting gluons affect those vacuum polarization corrections, leading to [11]:

$$\beta_0^s = \frac{1}{6\pi} \cdot [N_F - 16.5] \tag{2.3}$$

N_F represents the number of quark flavors with a mass smaller than ς, the second negative term exists due to the gluon corrections. Therefore β_0^s is always negative, meaning the coupling strength of the strong force decreases with higher energy (Fig. 2.5). This is the explanation for the confinement of the quarks and their asymptotic freedom inside the atom, since small distances relate to large energy transfers.

One complicating aspect of this running is, that - especially at high energy transfers - QCD is non-pertubative, which makes calculating QCD processes much more complicated than for example in QED, where calculations are far more advanced.

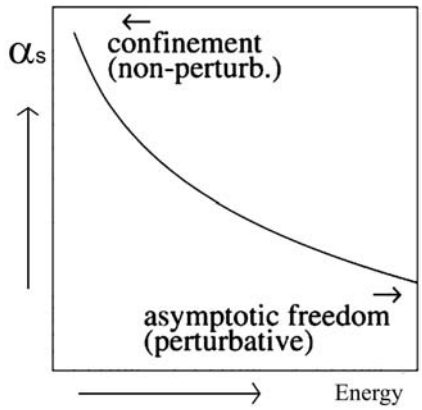

Figure 2.5: The running of α_s[11]

Electroweak Model

The origins of the electroweak theory lie in the beginning 20th Century.
By observing radioactivity,especially the β-decay, Hahn and Meitner (1911) concluded from the non mono-energetic electron energy spectrum that the β-decay could not be a 2-body decay. The continuous spectrum was observed 1914 by James Chadwick, yet it took another 20 years until Pauli postulated the existence of a new particle, the neutrino (which he called neutron). Then finally Fermi formulated the first theory for the weak interaction. Weak because a strongly interacting neutrino would have been observable at that time. Fermi explained the weak interaction through a four fermion vertex. This description made it possible to calculate cross sections and flight ranges for neutrinos. The neutrinos seemed to have ranges of order light years, which made it impossible to detect them with the detectors of those years.

It was not until 1956, when Cowan and Reines finally observed neutrinos in a reactor experiment, despite the weakness of neutrino interactions.

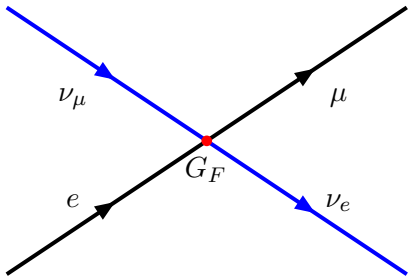

Figure 2.6: Electroweak Interaction (Fermi)

In the 1960 the modern electroweak theory was developed by Glashow, Salam and Weinberg (GWS), uniting the electromagnetic theory with the weak theory. From this point of view Fermi's 4 fermion interaction is now only a low energy limit. The new theory includes effects like C and P violation. It describes the interactions through the exchange of particles (Fig. 2.7) like the photon and the W, and made a prediction for the Z boson, giving rise to the so called neutral currents. The GWS electroweak model combines the

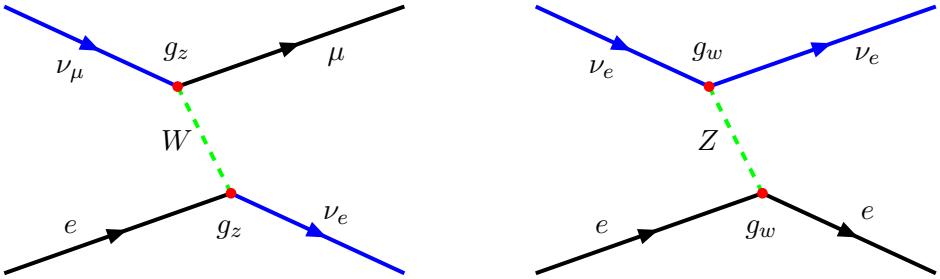

Figure 2.7: Electroweak Interaction (GWS)

abelian $U(1)_Q$ gauge with the non-abelian $SU(2)_L$ gauge weak isospin group, together forming the group $SU(2)_L \times U(1)_Y$. The $U(1)_Q$ represent the electromagnetic symmetry group which is generated by the electric charge Q. The weak isospin group $SU(2)_L$ acts on left-handed particles (parity-violation), while the $U(1)_Y$ represents the weak hypercharge acting on both, left handed and right handed particles.

The electroweak theory requires three weak isospin currents(J^i_μ) to couple to an isotriplet of massive vector gauge fields(W^i_μ) with coupling strength g, while the weak hypercharge current(j^Y_μ) couples to the neutral gauge field (B_μ), an isosinglet, with coupling strength $g'/2$.

Therefore the electroweak interaction can be written as[12]:

$$-ig\left(J^i\right)^\mu W^i_\mu - i\frac{g'}{2}\left(j^Y\right)^\mu B_\mu \tag{2.4}$$

The observed fields are superpositions of these gauge fields W^i_μ and B_μ.

$$W^\pm = \sqrt{\frac{1}{2}} \cdot (W^1_\mu \mp iW^2_\mu) \tag{2.5}$$

$$A_\mu = B_\mu \cdot cos(\theta_w) + W^2_\mu \cdot sin(\theta_w) \tag{2.6}$$

$$Z_\mu = -B_\mu \cdot sin(\theta_w) + W^2_\mu \cdot cos(\theta_w) \tag{2.7}$$

2.5-2.7 represent the $W^{\pm}$ boson, the photon (γ) and Z^0 boson the respectively.
The angle θ_w is the electroweak mixing angle, describing the existence of the neutral Z and γ as a mixing of the neutral gauge fields.

This mixing angle can not be calculated by the SM, and is therefore measured:

$$sin^2(\theta_w) = 0.23$$

Since the theory combines electromagnetic and weak forces the different couplings can also be related:

$$e = g \cdot sin(\theta_w) = g' \cdot cos(\theta_w). \tag{2.8}$$

The couplings of Z and W bosons are directly expressed through the electromagnetic coupling with:

$$g_w = \frac{e}{sin(\theta_w)} \tag{2.9}$$

$$g_z = g_w \cdot cos(\theta_w) = \frac{e}{sin(\theta_w)cos(\theta_w)} \tag{2.10}$$

The coupling describing the 4-fermion vertex in Fig. 2.6 is then:

$$G_F = \frac{\pi}{\sqrt{2}} \cdot \frac{\alpha}{m_W^2 \cdot sin^2(\theta_w)} \tag{2.11}$$

Where α is the fine-structure constant and m_W the W boson mass.

One interesting fact beyond the Standard Model is, that super symmetry can calculate the electroweak mixing angle with a good precision

Chapter 3

Important Quantities Of High Energy Physics

Every different kind of collider has its special properties and presents a unique physical environment. The next chapter summarizes some common properties and specialties of proton anti-proton machines like the Tevatron. The Tevatron and the DØ detector will be discussed in chapter 4.

3.1 Hadronic Collisions

In the following a short introduction shall be given about a few properties especially important when protons collide with anti- protons, both of which are composite particles.

3.1.1 Proton Structure and Parton Density Functions

A hadron collider like the Tevatron operates at high energies with protons and anti-protons, therefore one has to consider the inner structure of the particles.

Quantum mechanics prohibits a description of what the exact situation inside a composite structure of this size is, but one can still get to a formal description. One has to substitute the simple picture of a proton consisting of three quarks (uud) with a more complicated one, where "valence" quarks and "sea" quarks, as well a various gluons make up one proton. This then leads to the introduction of the formal structure functions of the proton.

The proton is consisting of a combination of all quarks, anti-quarks and gluons. Usually one would only think of the valence quarks uud, but there are also "sea" quarks. Both types of quarks are constituents of the proton, meaning that there is a probability for the proton to indeed contain charm or strange quarks, which are usually thought to be produced by gluons which keep the proton together.

Instead of gluons exchanging between the valence quarks one can also think of gluons converting into quark and anti quark pairs. As a consequence of these processes even the heavy quarks can be produced. In a simplified description one could say, that the nearer the observer comes (higher momentum trasnfer Q^2) the more details are visible.

In this context the variable x, called the "Bjorken x", is introduced. It is defined by $k^\mu = x \cdot P^\mu$ with the four-momentum of the incoming Proton P^μ and the momentum of the parton k^μ. This complicates physics immensely. First, not all of the center of mass energy of the collider is available for the reaction, and secondly the detector does not represent the rest frame, meaning most of the events are boosted along the axis of the reaction (z)

It is found that not only the quarks carry momentum of fraction x but gluons as well. Experimental data shows that gluons take about 1/2 of the initial proton momentum P^μ. Figure 3.1 shows the different parton densities densities, measured as well as parametrized, showing especially a large portion of sea quarks and gluons at low x.

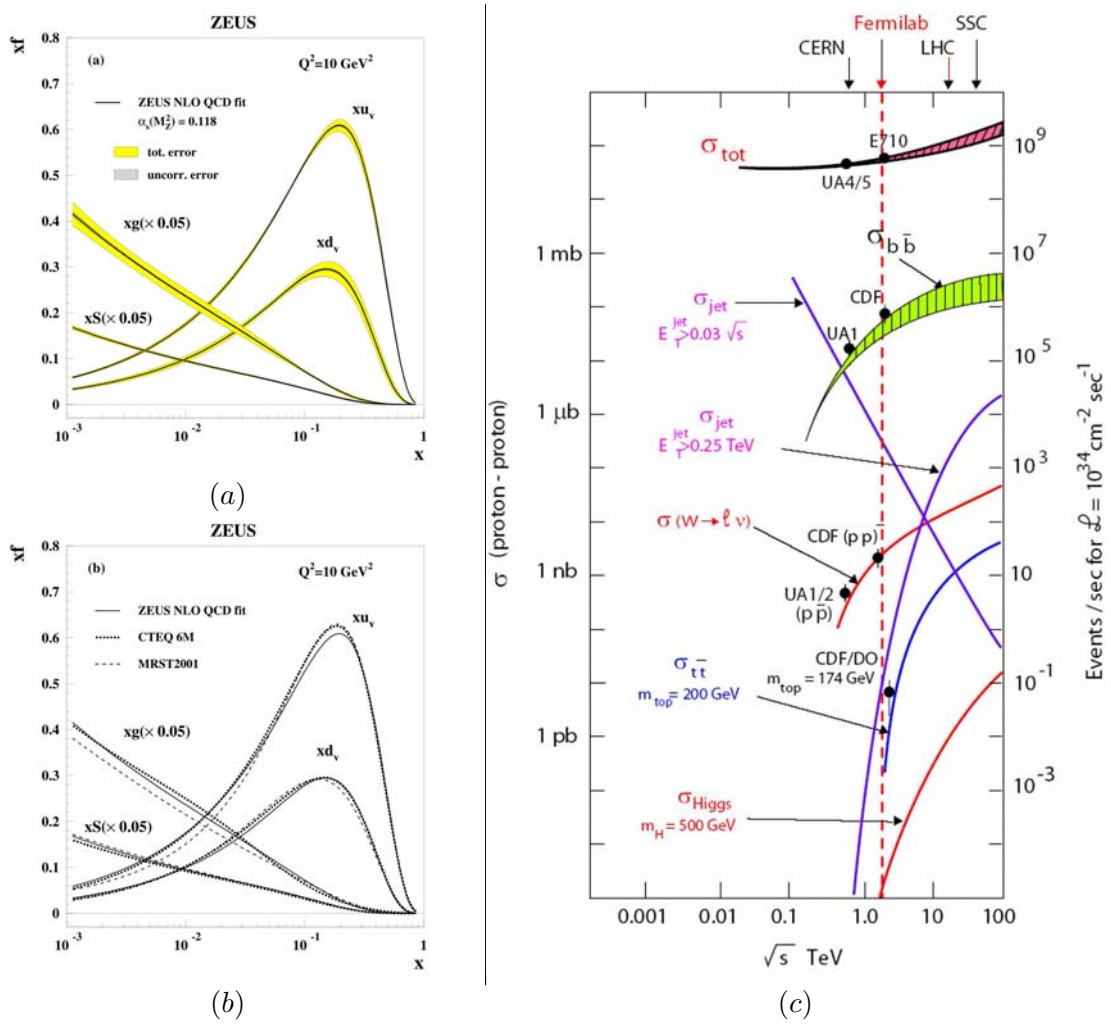

Figure 3.1: (a) The gluon, sea, and u and d valence distributions extracted from the standard ZEUS-S NLO QCD fit at $Q^2 = 10GeV^2$. The error bands in this Figure show the uncertainty from statistical and other uncorrelated sources separately from the total uncertainty including correlated systematic uncertainties. (b)The gluon, sea, and u and d valence distributions extracted from the ZEUS-S NLO QCD fit at $Q^2 = 10GeV^2$, compared to those extracted from the fits MRST2001 and CTEQ6 [13]. (c) Different cross sections as a function of $\sqrt{s}$ for hadron colliders, including the total cross section.

Parton Density Functions) (PDFs) An interesting aspect of these PDFs is the dependency on Q^2,which is called scaling violation. This violation results in a shift to smaller values of x as the momentum transfer increases. More "details" become visible. As the momentum transfer increases more gluon radiation takes

place such that the proton is dominated by gluons and sea quarks. This is relevant for high energy hadron colliders like the Tevatron where the interactions are dominated by processes including sea quarks and it gets more and more important at the later LHC where most of the processes will be gluon dominated.

One problem about these density functions is that they cannot be calculated theoretically, since the strong coupling constants complicates or even prohibits perturbative calculations. Since the usual MC simulation requires a set of these functions to describe the interaction processes accurately, one has to measure the PDFs at experiments like e.g. Hera in Hamburg (Germany). Figure 3.1(b) shows the data measured at Zeus in comparison with different parameterizations of the parton density functions.

The cross section (depends on the assumption of a special PDF) can be described for the process

$$p\,\bar{p} \rightarrow \text{“}F_{inal}\,\text{”}$$

and any arbitrary final state by:

$$\frac{d\sigma_F(\sqrt{s},Q^2)}{dQ^2} = \sum_{i,j} \int dx_i dx_j \; f_i(x,Q^2) f_j(x,Q^2) \cdot \frac{d\sigma_F^{i,j}(x_i,x_j,Q^2)}{dQ^2} \tag{3.1}$$

This includes all processes between two partons (f_i and f_j the respective densities) leading to the final state F. These processes are included with their respective differential cross sections and are then multiplied (weighted) with the density of the respective parton pairing.

Fig. 3.1 shows the total cross section σ_{tot} as well as a selection of some interesting processes with e.g. jet final states or some SM processes e.g. $W \rightarrow l\nu$. It is pretty obvious that QCD processes dominate the total cross-section at hadron colliders and they appear to be a large background for certain analyses but they themselves also represent an interesting field of study.

3.1.2 Hadronisation

Since quarks are produced in collisions of protons and anti-protons one has to come up with a mechanism that can sufficiently explain their further evolution through time.

To describe the process

$$q\bar{q}\;(\rightarrow q\bar{q}) \rightarrow hadrons$$

completely - since quarks can not stay free - one introduces the concept of hadronisation.

This simply means that new quark anti-quark pairs are produced, until all quarks are bound into mesons and baryons. These processes take places at a low energy scale, meaning that, as mentioned before, QCD calculations are extremely complicated. To overcome this problem, several models are used to describe the process of hadronisation.

The commonly used Monte Carlo Generator `Pythia` is based on the LUND string fragmentation model as is illustrated in Fig. 3.2. The concept of this model can simply be compared to a rubber band (color string). The energy between two quarks increases when they move away from each other, just as the tension of a rubber band increases, because more and more potential energy is stored in it. The strong interaction increases and eventually the energy is large enough to produce a new quark anti-quark pair; the rubber band in analogy would break.

The fragmentation continues until all quarks are bound in mesons and baryons. This model, as well as the other models, has to be compared to measured data, and then be tuned to reality which is still complicated, because of many adjustable parameters.

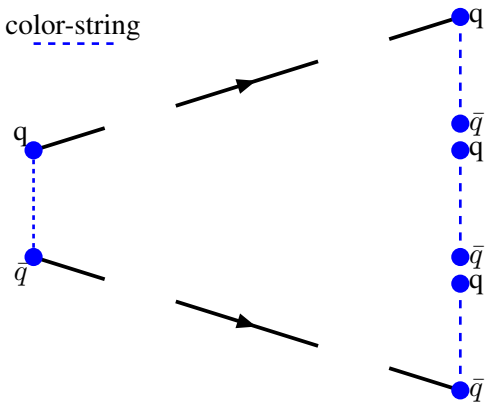

Figure 3.2: Sketch: String Fragmentation

3.2 Coordinate System and Kinematic Variables

To perform actual physical measurements, one of the first things to do is to choose a coordinate system describing the kinematics of the initial and final state particles within the detector. In order to do this the nominal interaction point, where the $p\bar{p}$ collision should take place by design, is set to be the origin of the coordinate system. Starting from this center the $z-$axis is chosen to be the axis parallel to the colliding beams coinciding with the direction of the proton beam, whereas the abscissa and the ordinate describe the transverse plane of the detector. For the DØ detector x is chosen to point to the center of the Tevatron ring and y upwards.

Especially this transverse plane is of uttermost importance for the measurements, since quantities described in these coordinates are not subject to the boost, e.g. p_T the transverse momentum (sec. 3.2.5). For a complete description of the physical process, especially the momentum, one needs the polar angle θ as well.

The direction of particles can be given by two variables, the azimuthal angle ϕ, which is per se Lorentz invariant and the polar angle θ. Since the latter is not invariant under a relativistic Lorentz boost in z, the pseudorapidity η (sec.3.2.1) is used instead.

3.2.1 Pseudorapidity η

The pseudorapidity is only defined in the high energy limit, where the rest mass can be neglected.
It is defined as :

$$\eta = -\ln\left[tan\left(\frac{\theta}{2}\right)\right] \tag{3.2}$$

For particles escaping with an angle of about 90° to the beam pipe the value of η is zero, while particles flying at $+z$ or $-z$ direction have positive or negative values of η, which will become infinite at θ near 0° and 180°. The quantity is used, since $\Delta\eta$ is Lorentz invariant.

3.2.2 The Azimuthal Angle ϕ

The above mentioned azimuthal angle is given by:

$$x = r \cdot cos(\phi) \tag{3.3}$$
$$y = r \cdot sin(\phi), \tag{3.4}$$

r representing the respective radius in the $x-y$-plane. Due to its definition, perpendicular to the direction of the boost, $\Delta\phi$ is Lorentz invariant.

3.2.3 Particle Distance ΔR

Since every parton is undergoing a Lorentz boost in z one needs the above defined variables to describe their interactions correctly. Combining these two quantities, one can define a Lorentz invariant spatial distance between two objects within the detector; similar to the normal Euclidean distance it is given by:

$$\Delta R = \sqrt{\Delta\phi^2 + \Delta\eta^2} \tag{3.5}$$

As crucial as a Lorentz invariant way to describe directions, particle flight and interaction in the detector, is a set of invariant kinematic variables. These are describing the properties like momentum, energy and mass of particles, which are of interest and are usually also boosted in the $\pm$ z direction.

3.2.4 Center of Mass Energy $\sqrt{s}$

One of the basic kinematic constraints is the center of mass energy. It actually is not a free parameter, as it is usually fixed for a given experiment and given by the maximal possible energy of the revolving particles as long as one has point like particles.

Since particles with an underlying substructure are used at the Tevatron, the parton which actually participate in the hard scatter have different center of mass energies depending on the parton distribution functions (PDFs) (3.1.1). The center of mass energy of two "identical" particles in a head on collision would simply be their energy sum. Since this is mostly not the one can write for two particles the Lorentz invariant:

$$\sqrt{s} = \left[(E_1 + E_2)^2 - (\vec{p}_1 + \vec{p}_2)^2\right]^{1/2} \tag{3.6}$$

3.2.5 Transverse Momentum

One of the often used properties is the transverse momentum p_T, which by definition is perpendicular to the boost. It is defined as:

$$p_T = \sqrt{{p_x}^2 + {p_y}^2} = p \cdot sin(\theta) \tag{3.7}$$

The center of mass energy (Sec. 3.2.4) is limited to the maximum of the experimental setup (collider, used particles) therefore objects with large transverse momenta are typically well measurable, due to their small η, which locates them in the well instrumented central region of the detector (sec. 4).

Since the $p\bar{p}$ bunches move along the z-axis, one can formulate momentum conservation for the x-y plane before and after the interaction.

$$\left(\sum_{\text{init. particles}} p_{x,y}\right)_{\text{before}} = \left(\sum_{\text{fin. particles}} p_{x,y}\right)_{\text{after}} = 0 \tag{3.8}$$

This transverse momentum balance can be used as an extra constraint and as a calibration tool for the detector. It is not easily possible to apply the same for the z-component of the components (beam remnants might disappear through not instrumented parts near/ along the beam pipe).

3.2.6 Missing Transverse Energy (MET)

Another quantity in many analyses is the missing transverse energy. This term describes not actually "missing" energy, but energy that the detector is unable to measure, e.g. neutrinos or non-SM particles which do not interact with the detector material. Using the transverse momentum balance (Eqn. 3.8) it is possible to infer the contribution of missing transverse energy (MET) in the $x-y$-plane.

$$\left(\sum_{\text{fin. particles}} p_{x,y}\right)_{\text{after}} + MET_{x,y} = 0 \tag{3.9}$$

3.2.7 Invariant Mass

The invariant mass characterizes the rest mass of a particle, which is an invariant under Lorentz transformation. This quantity is often used to find new particles, which manifest themselves as peak (resonance) in the invariant mass spectrum of two or more particles. A very prominent resonance would be the Z boson, which can be found as a clear "peak" in several di-lepton invariant mass spectra from decays like $Z \rightarrow ee$ or $Z \rightarrow \mu\mu$. The invariant mass for two particles is given by:

$$m = \sqrt{(E_1 + E_2)^2 - (\vec{p_1} + \vec{p_2})^2} \tag{3.10}$$

The similarity to $\sqrt{s}$ is obvious, which means, only particles with masses below the center of mass energy can be produced.

The invariant mass can quite easily be calculated for any number i of particles:

$$m = \sqrt{(\sum_i E_i)^2 - (\sum_i \vec{p_i})^2} \tag{3.11}$$

3.3 Luminosity and Cross Section

The most important properties of colliding beam experiments are the center of mass energy $\sqrt{s}$ and the instantaneous luminosity l. The luminosity is so important because it represents the direct connection between the eventrate ($R = \frac{dN}{dt}$), with which certain events occur, and the associated cross section σ.

$$R = \sigma \cdot l \tag{3.12}$$

3.3.1 Cross Section

The cross section is a simply representation of how often a certain event occurs. Since Quantum mechanics prohibits the exact knowledge of processes at small scales without interfering in the process, one has to rely on a descriptive probability approach.

To describe the probability for certain final states, the concept of the cross section is introduced.

A generalized description of a scattering process,without any given geometrical assumptions would lead to the following approach:

$$\sigma = \frac{A \cdot p}{N_{target}} \tag{3.13}$$

This formula combines several properties: A the impact surface, p the interaction probability and N_{target} the number of target particles.

A common form of the cross section is the differential cross section, which normally includes the dependency from some kind of kinematic variable x like e.g momentum.

$$\frac{d\sigma}{dx} = \frac{dp}{dx} \cdot \frac{A}{N_{target}} \tag{3.14}$$

Since cross section measured in cm^2 are fairly small one normally uses the unit barn.

$$[\sigma] = b = 10^{-24} cm^2 \; = \; 2580 \mathrm{GeV}^{-2} \tag{3.15}$$

The cross section of a certain process at a $p\bar{p}$ collision depends on the center of mass energy,$\sqrt{s}$, and connects, the event rates with the luminosity.

The σ of a given SM process, e.g. Z or W boson production, characterizes exactly how probable this kind of interaction is if the two initial particles collide. Cross sections are normally given in $\mathrm{p}b$ and are measure for of how often certain interactions take place.

3.3.2 Luminosity

Basically, luminosity describes the intensity of the two colliding beams and their mutual penetration. Since one usually prefers a large probability for hard processes, many particles should meet in an area as small as possible.

If one assumes a Gaussian profile for the proton anti-proton bunches of the beams containing $n_p/n_{\bar{p}}$ particles, the luminosity is given by:

$$l = \frac{f \cdot B \cdot (n_p n_{\bar{p}})}{4\pi\sigma_x\sigma_y}, \tag{3.16}$$

with f the beams' revolution frequency and $\sigma_{x,y}$ the beam width in x and y B the number of bunches.

To ensure an intense and focused beam within the detector beam optics focus the beam.

The quantity that is normally used to quantify the amount of data (events) that are recorded at an experiment over a given amount of time is called the integrated luminosity, which is given as

$$\mathcal{L} = \int_{t_1}^{t_2} l dt,$$

measured in $[1\mu\mathrm{b}^{-1} = 10^{30} cm^{-2}]$.

Chapter 4

The Tevatron and the DØ Experiment

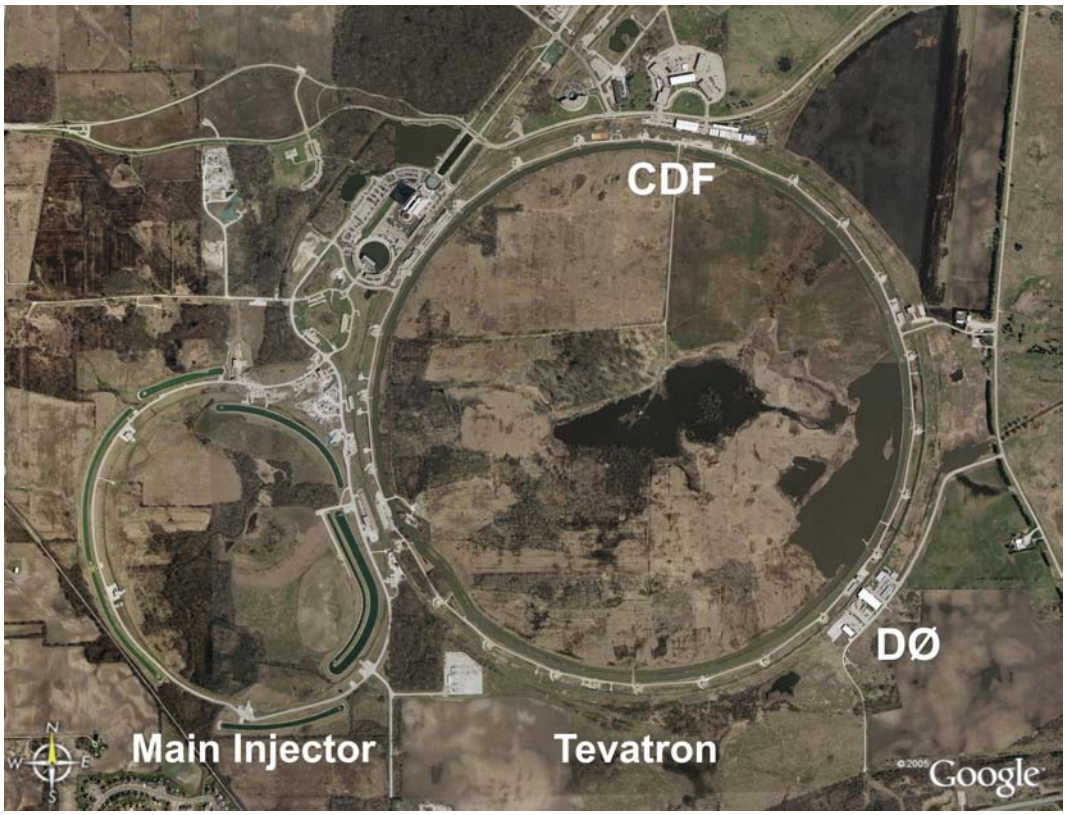

Figure 4.1: The Tevatron from 10000 ft [21]

The Tevatron proton anti-proton collider represents at the moment the highest energetic facility in operation, located at the Fermi National Accelerator Laboratory (Fermi-Lab) west of Chicago (USA).

Beginning operations in 1967 as the National Accelerator Laboratory it was 1974 officially named after Nobel Prize Winner Enrico Fermi (†1954).

During the operation of the Lab fundamental discoveries like the Bottom and the Top quark as well as the verification of the tau neutrino existence are the highlights of a long list of successes in modern high energy physics.

Figure 4.1 shows a view on the Tevatron part of the 27.5 km^2 large Fermilab site. One can see the Tevatron, the large ring structure with its two detectors CDF (North) and DØ (East).

The so called Run I period of the Tevatron Collider at $\sqrt{s}$ =1.8 TeV ended after about five years of operations in 1996 to start a major upgrade on the accelerator (with the newly built main injector ring) and the detectors to the now operating 1.96 TeV accelerator (Run II). In Run I an integrated luminosity of about 130 pb^{-1} was recorded. The main reason for the Run II is the possibility of much higher luminosities and therefore being able to study processes at low cross sections, like top or W/Z processes. With the Run II operations starting 2001 the Tevatron continued its efforts on filling the holes of modern High Energy Physics (HEP), finding the Higgs, searching the supersymmetric partners of the known matter and keeping an eye on physics beyond the known realms.

So far the operations of Run II were a success with a delivered luminosity of about 1 fb^{-1} as of October 2005. It is expected for Run II to reach about 4-9 fb^{-1} until the Tevatron's expected shutdown in 2009, depending on accelerator and detector evolution.

In the following a short overview about the accelerator systems as well as well as the DØ detector and its most important subsystems are given.

4.1 The Tevatron Accelerator Chain

In the year 1983 the Tevatron was built as the worldwide first Synchrotron with superconducting magnets and represents the only operating machine exept for the Hera Collider in Hamburg until the Large Hadron Collider (LHC) at CERN will start its operations around Juli 2007 with a startup phase for the accelerator.

Even though the Tevatron main ring with a circumference of around 6.28 km (3.9 miles) is the most prominent feature, the whole accelerator chain consists of much more than that. A series of different machines is used to bring the protons (p) and anti-protons($\bar{p}$) to their final energy of about 980 GeV, leading to the center of mass energy of 1.96 TeV.

The whole setup is shown in Fig. 4.2.

For protons(p) it all starts with the ionization of hydrogen gas, in this case producing negative hydrogen ions with two electrons and one proton. In the Cockcroft-Walton accelerator these ions are accelerated by a us of a positive charge up to 750 keV, here the ions are bunched and afterwards handed over to the next stage accelerator, a 150m Linac (linear accelerator), which boosts their energy via oscillating electrical fields up to 400 MeV. In order to obtain "blank" protons the ions pass now a carbon foil to strip the electrons off, leaving only the positive proton. In the next step these protons are passed over to the Booster, a synchrotron 150m in diameter, bringing the protons to an energy of about 8GeV. The Booster uses magnetic fields to hold the particles en route and uses electric fields in order to speed up the protons during revolution cycle. The protons are now sampled into bunches of $\mathcal{O}(10^{10})$ and enter the Main Injector, another synchrotron with 3 km in circumference, which can now boost the particles to 150 GeV.

In addition to accelerating protons to 150 GeV, the main injector is used for three further purposes. First and most important, it sends 120 GeV protons to a nickel/copper target producing anti-protons. About 10^5 protons are needed to produce one anti-proton with the necessary energy of ≈ 8 GeV. This delivers about 10^{11} $\bar{p}$ per hour, which are collected, de-bunched, stochastically cooled, focused, and stored. Second, it is used to get also the anti-protons up to 150 GeV. Finally, the Main Injector injects the protons and anti-protons into the main storage ring, the Tevatron. An interesting property of both the main injector and the

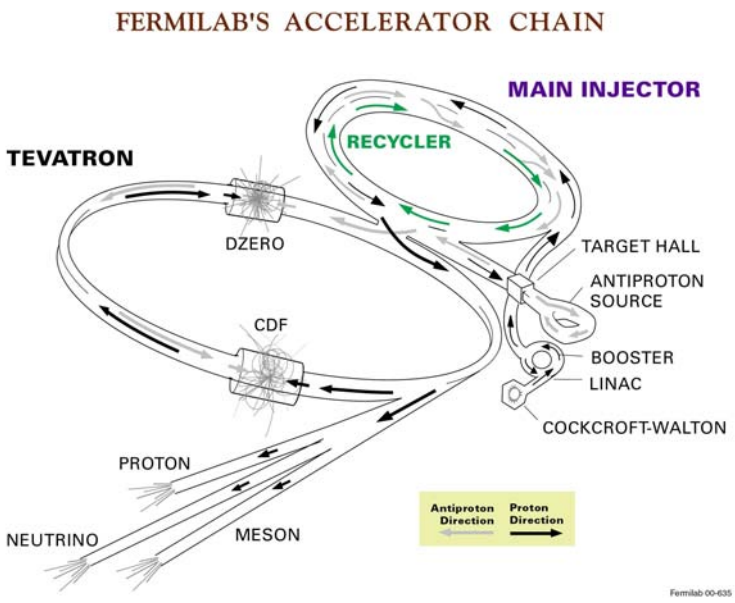

Figure 4.2: Fermilab Accelerator Chain - Schematic drawing of Accelerator Complex [22]

Tevatron itself is the use of only one ring to accelerate protons as well as anti-protons, which is possible due to their opposite charge.

The Tevatron at least brings the protons and anti-protons to the final energy of 980 GeV.

To ensure the passage of the particles within the storage ring on their circular path a magnetic field of 4.2 T is used. This field is produced by a complex system of superconducting dipole and quadrupole magnets arranged along the whole ring. The cooling system of the Tevatron supplies the operating systems with a temperature of 4.2 K in order to maintain super conduction within the magnets.

The two experiments are located at two separate interaction points along the Tevatron ring, B0 for the CDF experiment, and D0 for the DØ experiment. At these location proton and anti proton bunches penetrate each other.

A Few Facts[29]

- Protons and anti-protons circulate in three trains through the Tevatron, each containing 12 bunches (36x36 bunches overall).
  - Train separation: 7 μs
  - Bunch separation: 396 ns
- The momentary Peak Luminosity : $120 \times 10^{30} cm^{-2} s^{-1}$
- The ultimate goal for Run II instantaneous Luminosity : $200 \times 10^{32} cm^{-2} s^{-1}$
- Number of Interactions per bunch crossing is about 2.3 (luminosity depended)

4.2 The DØ Detector

The DØ detector was built in the early 1990's together with the start of Run I of the Tevatron and then upgraded for Run II. The upgrade was necessary to match the new requirements of the Collider now delivering much more luminosity than before. Therefore many of the subsystems were overhauled or even replaced. The trigger systems were improved to compensate for the much higher event rates, a new tracker system including the new solenoid magnet was put in place in order to get a more precise tracking, and the muon system was improved but its full coverage of the detector was kept.

"Multi purpose" because of its capability of detecting almost every particle arising from high energy collisions as is explained in Figure 4.3. As every modern HEP Detector the DØ detector can be divided in different layers, each beeing abled to fulfill a different function.

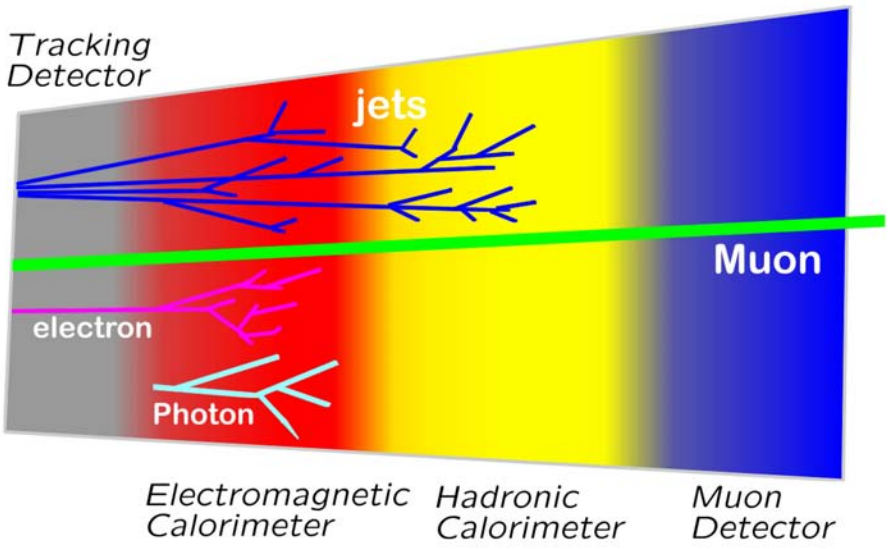

Figure 4.3: The principle layers of a multi purpose detector in high energy physics

Beginning in the innermost core of the detector, there is the tracking system (sec.4.2.1), used to measure particle tracks, equipped with a magnet to bend charged particle tracks for momentum measurements.

Following this central part one usually finds a calorimeter (Sec. 4.2.3), used to measure electromagnetic particles energy as well as hadronic particle energy deposition. Electromagnetic particles normally are covered with the electromagnetic calorimeter, producing distinct shower shapes depending on the character of the particle (e.g photon,electron),while the hadronic jets usually start showering in the electromagnetic calorimeter but are usually not stopped until they reach the outer coarse hadronic calorimeter regions. The minimum ionising particles like muons go directly through the innermost parts of the detector and are the only particles that are measured in the outer muon system (Sec. 4.2.4). "Non"-interacting particles like neutrinos can not be detected directly and are inferred from the measured energy depositions.

In order to get a hand on the particles momentum and charge one usually covers the whole detector with a magnetic field which bends the track of charged particles. The upgrade for the DØ detector lead to the modern multipurpose detector which can be seen in Figure 4.4. The detector as is shown contains

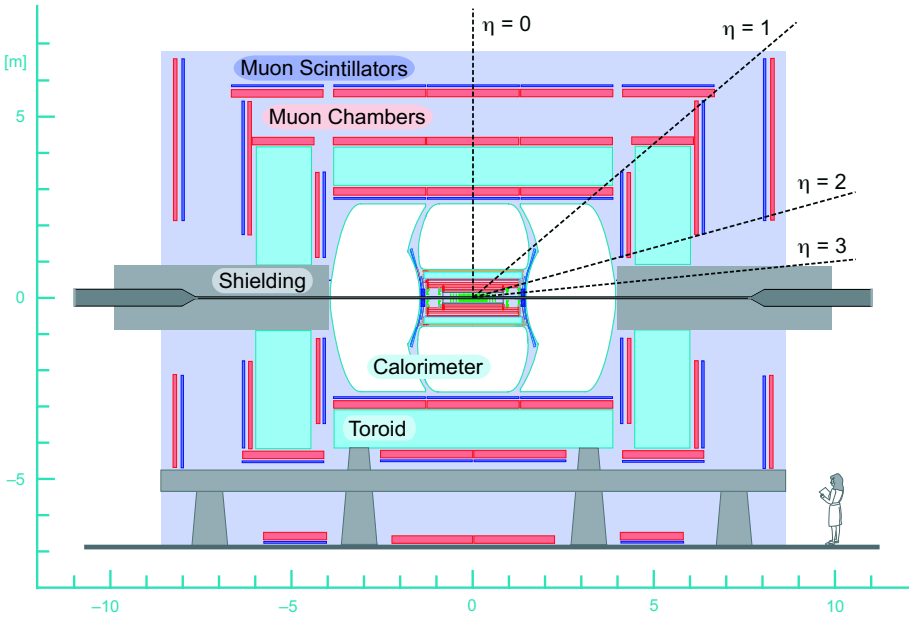

Figure 4.4: The DØ detector with inner tracking, calorimeter, magnets and muon system[24]

two different magnets. The inner solenoid covers the tracking system with a 2 T magnetic field and the outer Toroid provides a 1.8 T magnetic field within the muon detector, leading to an extra momentum measurement capability for the muons outside the tracker. The whole detector measures 20 m in length and around 11m in diameter. The coordinates, shown in Fig. 4.4, are in accordance with the description in Section 3.2, which is set to zero at the nominal interaction point in the center of the detector.

All systems of the DØ detector are build, to deliver a very precise measurement of the particles emerging from the primary interaction zone. This includes the determination of their primary properties, e.g energy, momentum and direction. For special b-physics requirements this also means to reconstruct displaced secondary vertices, which can be quite difficult since the primary interaction point varies around 60 cm along the z-axis.

In the following a short introduction on the different subsystems will be given.
More detailed descriptions are given in [4, 19, 20].

The detector itself and the Tevatron undergo smaller upgrades on a regular basis to ensure and improve their functionality; since the start of Run II several upgrades have been made on the detector, including electronics and software and further upgrades are planned for the 2006 shutdown period, e.g. integration of a new silicon tracker layer called “Layer Zero.”

4.2.1 The Tracking System

The Tracking systems was one of the major parts, that were upgraded for Run II. This upgrade included the new 2 T Solenoid as well as the Silicon Vertex Detector (SMT) and eight surrounding layers of scintillating fibers (CFT) (Fig.4.5).

The main reason for the replacement of the old tracking system were the introduction of a new solenoid magnet in order to improve the tracking since the tracker of Run I had no magnetic field. In addition it was necessary to deal with enhanced requirement on radiation hardness due to the increased luminosity and the

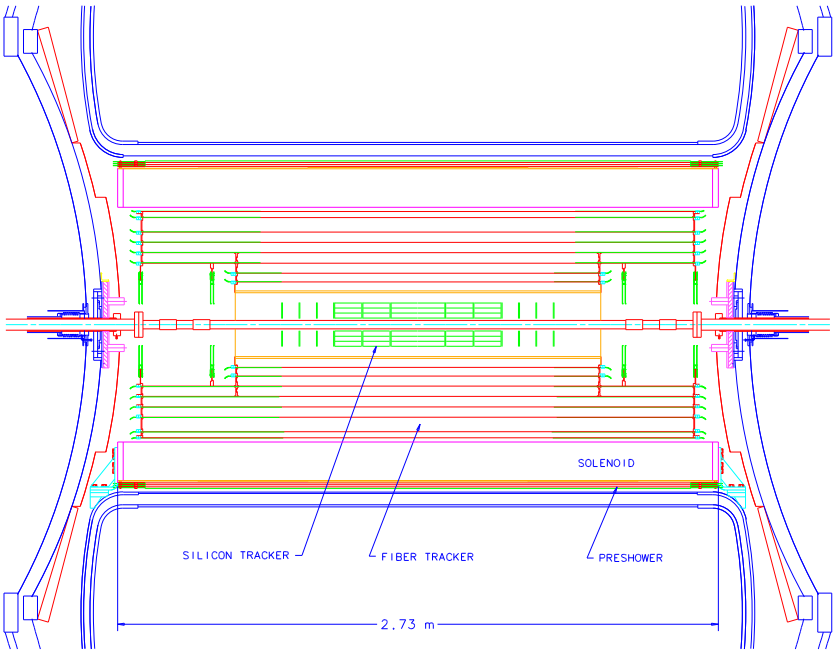

Figure 4.5: The DØ-Tracking system with silicon and fiber tracker, solenoid as well as the preshower detector [25]

need to extend the tracking capabilities up to around $\eta \approx 2$. The SMT together with the new solenoid was integrated in order to increase the tracking capabilities. The superconducting solenoid is 2.8m in length and located around the tracking system. It is cooled by liquid helium provided from the DØ cryogenic services.

Even though the newly added magnet together with the cryostat accounts for another 0.9 radiation lengths to the detector material, it is crucial to the tracking. The tracker has, due to the homogeneous magnetic field inside, a momentum resolution [74] of

$$\frac{\Delta p_T}{{p_T}^2} = 0.002 GeV^{-1}$$

, given for the inner tracker. A sketch of the tracker system is shown in Figure 4.5 and 4.4, which also displays the range of the tracking capabilities up to $\eta \approx 2$ due to the CFT (cf. Sec. 4.2.1).

Tracking Subsystems

Silicon Microstrip Tracker (SMT)[14] The Central Silicon Detector is the first detector to be encountered by particles coming from the interaction zone.

The detector consists of six barrels around the beam axis, each containing four layers arranged axial around the beam pipe. The innermost layer as well as the third layer are single sided detectors equipped with axial strips, while the other two layers are two sided, one equipped with axial strips, the other with 2° stereo strips. Each barrel segment is 12cm in length and separated by 8mm gaps which contain the so called "F-disk"s, which are also positioned at the end of the barrel (cf. Fig. 4.6). In addition there are two more "H-Disk"s located at $z = (\pm 110$ and $\pm 120)$ cm.

The "F-" and "H-disk"s are double sided Detectors with 30° and 15° stereo setup respectively.

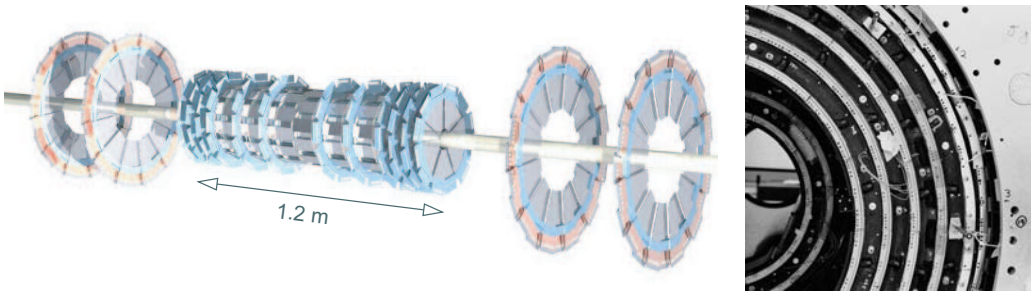

SMT *CFT*

Figure 4.6: L: Silicon vertex detector with its structure, barrel and discs [25]; R: Central Fiber Tracker at assembly [26]

This configuration allows to measure collisions along the whole 25 cm of the interaction "zone". The barrel measures basically $r - \phi$ while the disk can measure $r - \phi$ as well as $r - z$ for the particle tracks. Vertices with high η are reconstructed in three dimensions, mainly by the disks, while at small η the barrels are used. Depending on particle origin and direction the SMT can account for up to 20 hits.

The silicon part of the Tracker consists of 800.000 individual strips and readout channels. It has a spatial resolution of 10 µm in the transverse plane and 100 µm along the $z-$axis [18].

Central Fiber Tracker (CFT)[15] The CFT as the second part of the tracking system is made up of layers of scintillating fibers. This device serves two main purposes, on the one hand it provides additional tracking information and on the other hand it is used for fast Level 1 track triggering.

It is made up of about 74000 scintillating fibers of 0.8 mm in diameter. These fibers are mounted on eight concentric cylindric shells with radii of 19.5 cm up to 51.5 cm. Each of these shells supports two fiber doublets, one parallel to the z-axis and the other one tilted by around 2° to deliver stereo information. To convert the photonic signals into electronic ones, one first uses waveguides to get visible photons which then are counted by Visible Light Photon Counters. These VLPC are silicon based converters which change the incoming light into an electrical pulse.

As many of the other systems of the detector these VLPCs have to be cooled to reach acceptable quantum efficiencies for the conversion. When operating at temperature between 6 and 15 K the efficiency reaches about 80% and the gain is 20,000 up to 50,000.

The CFT reaches pseudo-rapidities up to 2 and therefore is the limiting part of the tracking system, similar to the SMT it has a resolution of approximately 100 µm.

4.2.2 The Central and the Forward Preshower Detectors

The Central Preshower Detector is placed in the gap between the solenoid coil and the central calorimeter cryostat and covers a region of $|\eta| < 1.2$. It is designed to aid for electron identification and by making precision position measurements. It supports triggering and corrects electromagnetic energies for the ievitable effects of the showering in the solenoid. Together with an additional lead absorber, the material before these 3 layers of scintillating strips totals two radiation lengths. The Forward Preshower Detector at $1.4 < |\eta| < 2.5$ is constructed similarly, with additional lead absorbers accounting for the absence of the solenoid. Both

detectors can be seen in Figure 2.6 outside the inner tracker. The data analysed in this paper do not make use of both of these Preshower Detectors as they are still under commissioning and the software is not completed yet.

4.2.3 The Calorimeter [17]

The Calorimeter(CAL) measures the energies of electrons, photons and hadronic jets and their properties. In the case of DØ it consists of layers of absorber material like uranium copper and steel and liquid argon flows through this system. Particles like electrons, photons and hadrons all loose their complete energy in

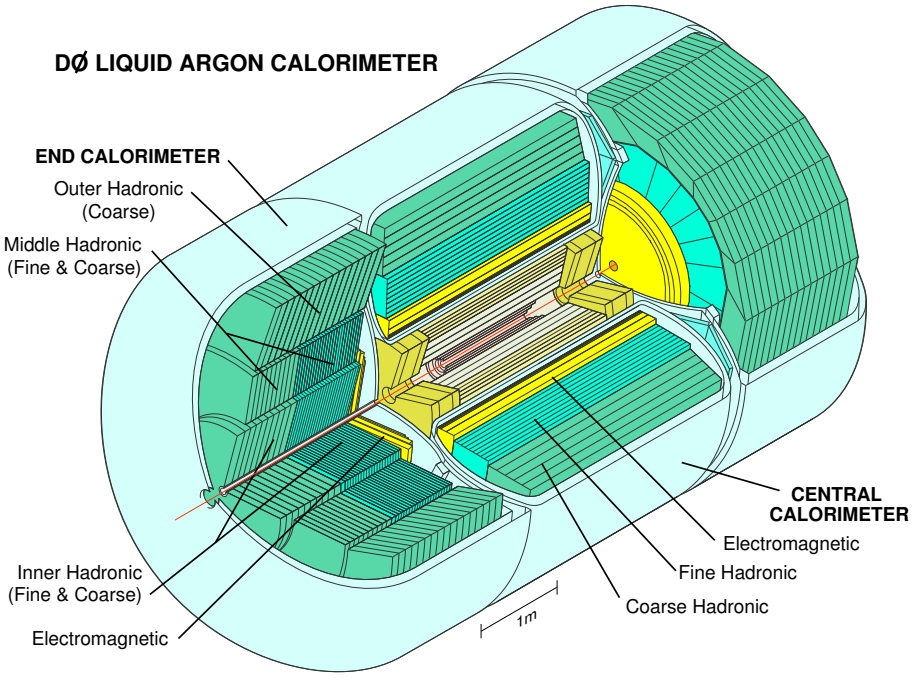

Figure 4.7: Sketch of the DØ liquid argon calorimeter [24]

the calorimeter due to the interaction with the calorimeter material (showering). Electrons or photons for example loose their energies in showers originating from pair production and bremsstrahlung, while hadrons interact inelasticly with the absorber material of the calorimeter and produce hadronic showers.

Both kind of showers ionize the active medium of the calorimeter, in case of DØ liquid argon. This ionization is being collected on metal plates and then gives an electrical signal to the readout electronics. By measuring the electric response as well as the position of the calorimeter cells, in which this response occurred, one can reconstruct energy and momentum of the incoming particles. Since the calorimeter is able to detect charged as well as neutral particles the total amount of the energy coming from the original particle can be determined. In addition the Calorimeter provides information about the shower shape and size with helps to distinguish electromagnetic and hadronic objects.

Due to the low temperature requirement of the liquid argon, the whole calorimeter has to be hosted inside a cryostat. In order to keep the tracking system as well as the other innermost parts of the detector accessible, the cryostat is divided into three parts, the central part (CC) covering $|\eta| < 1.2$ and the two End Cap calorimeters (ECN/ECS) in the northern and southern parts of the detector(as can be seen in Fig. 4.7), which extend the coverage in $|\eta|$ from 1.4 to 4.0.

The calorimeter consists of three cylindrical shells, with 32 electromagnetic modules in the inner ring, and 16 fine hadronic (FH) and coarse hadronic (CH) modules, respectively. The Calorimeter cells are read out in pseudo projective towers as is displayed in figure 4.8, meaning the towers lie on virtual rays coming from the nominal interaction point of the detector. The EM-CAL is divided into four layers in depth (CC&EC),

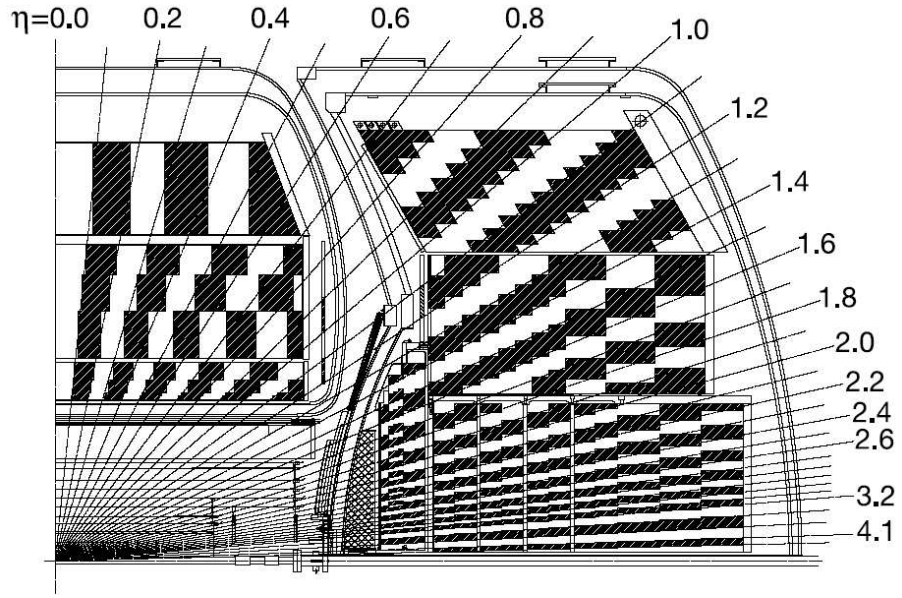

Figure 4.8: Sketch of the DØ liquid argon calorimeter [24] showing the projective tower design

the fine hadronic part is divided in three layers (CC) and four in the End Caps. The Coarse hadronic part contains one and three layers, respectively.

The cells of the calorimeter are composed of alternating layers of signal boards, absorber material, divided by 2.3 mm of the active medium (liquid argon). Between the absorber and the signal board a 2kV high voltage is applied.

Even though the liquid argon is used in every part of the calorimeter, the absorber material is different for various parts of the calorimeter, while the innermost, electromagnetic part of the calorimeter is only using 3 or 4 mm thick plates of depleted uranium to initiate the showering, the fine Hadronic section is equipped with a 6mm thick uranium alloy containing 2% of niobium. The coarse hadronic module sections contain relatively thick (46.5 mm) plates of either copper (CC) or stainless steel (EC). Electrical connections to all absorber plates were made by percussive welding of thick niobium wires to the edges of the plates.

The calorimeter cells are all segmented in $\Delta\eta \times \Delta\phi$ in 0.1×0.1 except the third layer of the EM-Cal which is segmented even finer into 0.50×0.05 cells since usually the electromagnetic shower maximum is expected here. A summary about the radiation lengths and nuclear absorption lengths of the different parts of the calorimeter is given in Tab. 4.1, and at much more detail in [19, 20].
To measure energies correctly, based on the electrical output pulses from the read out electronics, a calibration has been done. The energy resolution for both parts can be described via three terms as:

$$\left(\frac{\Delta E}{E}\right)^2 = C^2 + \frac{S^2}{E} + \frac{N^2}{E^2} \tag{4.1}$$

- C represents a systematic term including calibration errors
- S accounts for statistical uncertainties due to sampling fluctuations

Layer	CC[54]	EC
EM 1, 2, 3, 4 d=25cm	X_0: 1.4, 2.0, 6.8, 9.8 3 mm Uranium	X_0: 1.6, 2.6, 7.9, 9.3 4mm Uranium
FH 1, 2, 3,(4)$_{EC-only}$ d=75cm	λ_A: 1.3, 1.0, 0.76 6mm Uranium	λ_A : 1.3, 1.2, 1.2, 1.2 6mm Uranium
CH 1, (2, 3)$_{EC-only}$ d=60cm	λ_A: 3.2 46.5mm Copper	λ_A : 3, 3, 3 46.5mm Steel

Table 4.1: Radiation lengths (X_0) for the four Electromagnetic layers, as well as the absorption length for the fine (FH) and coarse (CH) hadronic parts of the central (CC) and the endcap (EC) modules of the calorimeter. Given is the absorber material and the thickness d of the respective layers at $|\eta| = 0$ [19, 20, 4]

- N is the noise term, describing the residual radioactivity of the uranium and electronic noise

The values of the three parameters are measured, or based on simulations, since one cannot simply deduce them from the calorimeter design itself. C,S,N are listed in Table 4.2. In the case of the pion the resolution is quite good, while for hadronic showers in most cases the resolution is worse since the particle shower contains much more than "simple pions". A few other effects can lead to a decreased resolution of the

Particle	C	S[$\sqrt{GeV}$]	N [GeV]
e	0.04	0.20	0.29
π	0.03	0.42	1.28

Table 4.2: Resolution parameters for the electrons (e) and pions (π), resulting from Monte Carlo studies of the DØ EM-ID group[41] and test beam experiments, respectively[19]

calorimeter, since the detector is divided in quite a few parts, there are regions where the resolution is much worse.

For the EM-CAL for example the fiducial regions are defined as the most reliable ones. Particles which go through the EM-Cal outside of the transition regions of the modules and in a certain z range ($|z|$ <110cm) in the 3rd layer are reconstructed best.

Inter Cryostat Detector (ICD)

Since the calorimeter consists of three parts (Fig. 4.7) there is a gap between the cryostats ($1.1 < |\eta| 1.4$), a region which is not so well instrumented. A so called Inter Cryostat Detector is inserted here to compensate these deficiencies and improve measuring of jets and connected properties. It is made of a single layer of scintillating tiles (384) for each end cap.

4.2.4 The Muon System [16]

The DØ detector has a seperate muon system (Fig. 4.9), the outermost detector. Even though the DØ central muon system is basically the same since Run I of the Tevatron. It was upgraded with e.g. a new shielding in order to reduce background from scattered proton or anti-proton remnants, and the forward muon system was replaced completely. The muon system consists of more then one component, e.g there are differences between the forward and the central part of the muon system. The wide angle muon spectrometer (WAMUS)

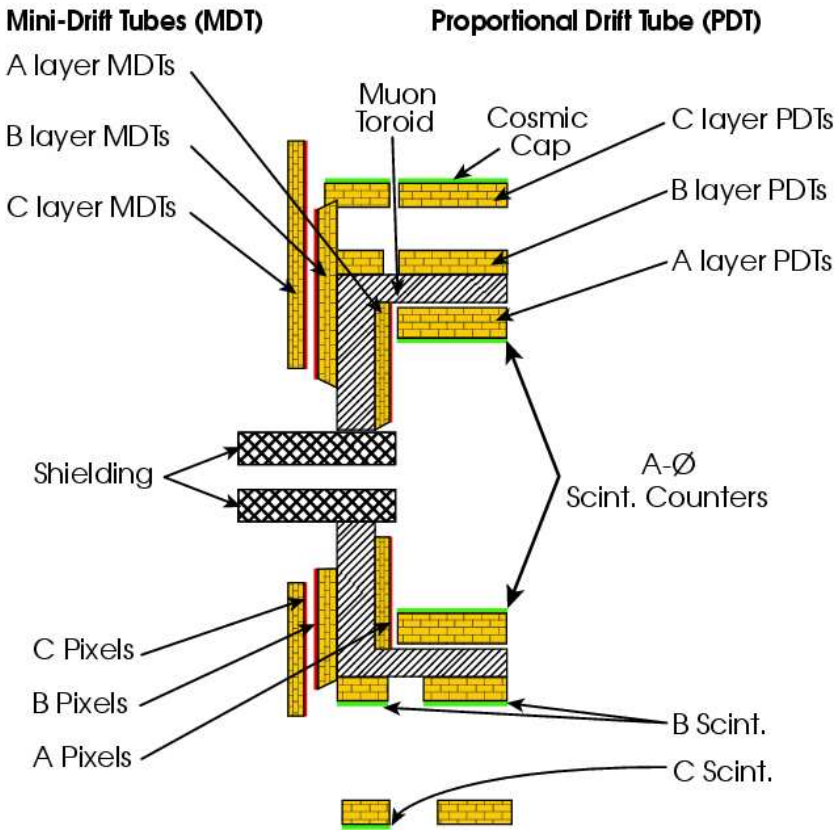

Figure 4.9: Sketch of the Muon System and its components [27], shown are the forward and central muon detector components

covers the central region of the detector up to $|\eta| < 1$, while the forward muon spectrometer (FAMUS) covers muons between $|\eta| > 1$ and $|\eta| < 2$.

WAMUS and FAMUS are both made of three layers (A,B,C), while they differ in design and used detector types. Some details are given below.

WAMUS

The A layer of the central region lies between the calorimeters' cryostat and the 1.9 Tesla Toroid. It is made up of the four layers of Run I proportional drift chambers (PDT) at the top and 3 layers at the bottom part of the detector and contains 630 new scintillation counters from the Run II upgrade. The scintillation counters are mostly used to have better triggering capabilities, since the PDT's maximum drift time is 450ns and therefore too slow for Run II operations. The PDTs are rectangular, tubes with 5.7×10 cm cells. They use a gas mixture of 80% argon, 10% tetrafluoromethane and 10% methane. The Toroid is positioned right inside the muon system, enabling an independent measurement of the muon p_T. The Toroid is 1 m thick which means that muons with energies above 3.5 GeV can cross the iron toroid at $\eta = 0$, while they even higher energies at larger η.

The layers B and C are positioned behind the Toroid and consist both of 3 layers of PDTs and on top of layer C another layer of scintillation counters (except bottom part, Fig. 4.2.4). Both mentioned scintillation layers (A,C) are segmented in ϕ and z with a granularity of 4.5° and 0.85 m respectively.

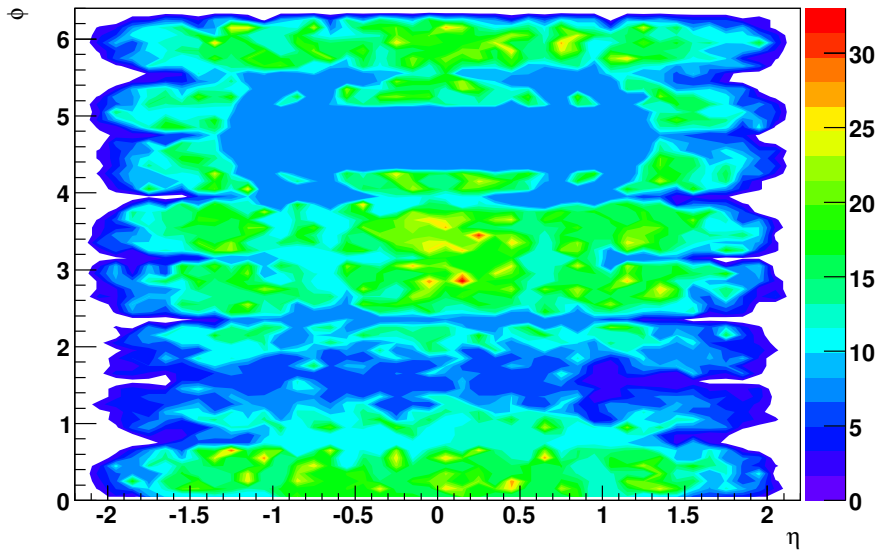

Figure 4.10: $\eta - \phi$-plot for the two highest energetic muons, showing the not instrumented region at the bottom of the detector (Colors represent the number of entries)

Figure 4.9 shows that there is not only the segmentation from the different PDT chambers in ϕ but also a significant "hole" in the bottom area of the detector. This hole is due to a not instrumented region of the detector which holds the support feet for the detector. This region is only instrumented with some scintillation counters, but as far as this analysis goes the data does not include these "scintillator only" muons.

FAMUS

The forward PDTs from Run I suffered from severe radiation damage and were hence replaced by mini-drift proportional tubes (MDTs) with a maximum drift time of ~ 60 ns and an increased coordinate resolution of ≈ 0.8 mm (PDT $\approx$1 mm). The mini-dift tubes are made of 1×1 cm extruded aluminum combs and contain the same gas like the PDTs of the central region.

The A layer of the forward system is made of 4 decks of MDTs, the B and C layer of 3 decks each.The MDTs were chosen, in order to withstand more radiation then the original Run I PDTs, since they have to operate within a detector used for much higher luminosities.

In addition of theses drift tubes, the 3 layers also contain 4608 scintillation counters which cover mostly the same in η like the MDTs and are segmented in ϕ and η ($\Delta\phi \approx 4.5^\circ$ and $\Delta\eta \approx 0.1$). They have a size of about 20×30 cm^2 and assist in triggering of muons.

Momentum Resolution

The momentum resolution for the muon system is different for FAMUS and WAMUS. A 100 GeV muon for example could be measured within the central region with a resolution of about 30%,

Because of the toroid filed the muon tracks are bended and the resolution ia about

$$\frac{\Delta p_T}{{p_T}^2} = 0.004 GeV^{-1},$$

hence two times worse compared to muons measured with the central tracking system. This resolution can be parameterized as

$$\frac{\sigma(\frac{1}{pt})}{\frac{1}{pt}} = \sqrt{A^2 \cdot p_T^2 + B^2}, \tag{4.2}$$

with A=0.00437 the resolution term, and B=0.348 accounting for multiple scattering in the toroid (see [75]).

In general the momentum resolution is far better with the central tracking than with the local muon system. The muon resolution at low p_T is limited by multiple scattering and limited at high p_T since the momentum is derived from the curved track inside the toroidal magnetic field. The measured parameter for these tracks is the sagitta, which represents basically the maximum deviation from the straight line between two points of the track.

Under the assumption of a constant magnetic field and a muon track perpendicular to this field, one can express the momentum of the muon as :

$$p[GeV] = 0.3 \cdot \frac{B[\text{Tesla}] \cdot (L[\text{m}])^2}{8s[\text{m}]} \tag{4.3}$$

s[in m] the sagitta, B the magnetic field [in Tesla], p the muon momentum [in GeV], L [in m] the distance between the two track points.

As one can see the momentum resolution is constrained through the exact measurements of the sagitta analogue to the tracker. The higher the muon energies, the straighter the track and therefore the smaller the sagitta. Since the spatial resolution of the muon system is naturally not as good as the one in the silicon tracker and also takes into account the multiple scattering, one can see the difficulty in the local muon system p_T measurement.

Since many analyses require a good resolution the central track is normally used for the p_T measurement.

Finally, the muon system includes a shielding of iron and lead surrounding the beam pipe from the calorimeter to the accelerator tunnel. This shielding is meant to decrease the probability for fake tracks and to slow down aging of the detector due to beam remnants.

4.3 Luminosity and Triggers

4.3.1 Luminosity

The characteristic parameters of the high energy experiments are luminosity (sec.3.3) and center of mass energy (sec.3.2.4). This leaves the problem of actually measuring the luminosity for the interaction at DØ. The measurement is performed with two luminosity monitors (Fig. 4.11), which are located at the end of the cryostat at ≈ 1.4 m in z from the center of the detector.

The luminosity monitors (4.11) consist of 24 hodoscopes containing scintillator pixels which cover a pseudo rapidity from $\pm$2.6 up to $\pm$4.5.

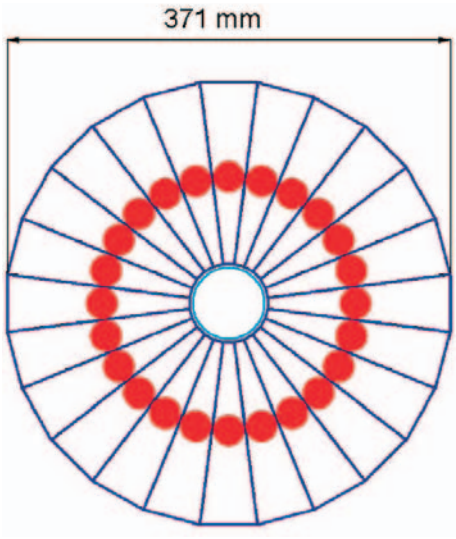

Figure 4.11: Geometry of one of the luminosity monitors. The photomultipliers are represented by the red dots, the beam pipe is in the center [3]

In principle these detectors measure rates of three processes which together account for the total rate of inelastic $p\bar{p}$ collisions. These processes are "single diffractive" (1),"double diffractive" (2) and "hard" (3) scattering at low angles:

1. One of the initial particles breaks into pieces.
2. Proton and anti-proton fracture into hadron jets.
   Mesosons and baryons are formed through hadronisation of the interacting quarks.
3. The initial particles are building new particles.
   Proton and anti-proton remnants scatter at large η.

With the knowledge of the total cross section, the acceptance A_{cc} and efficiencies ϵ_l of the hodoscopes, the luminosity can be determined via:

$$\mathcal{L} = \frac{1}{\sigma_{p\bar{p},eff}} \frac{dN}{dt}(p\bar{p}) \tag{4.4}$$

$$\sigma_{p\bar{p},eff} = \epsilon_l \times A_{cc} \times \sigma(p\bar{p}) \tag{4.5}$$

With $\frac{dN}{dt}$ the given collision rate and $\sigma_{p\bar{p},eff}$ the luminosity constant.

The luminosity depends on which constant is used for the measurement. Since the beginning of 2004 CDF and DØ agreed [30] on adopting the same proton anti-proton cross section of (60.7 ± 2.4) mb this leads to a recalculated luminosity constant of (46 ± 3) mb.

The estimated uncertainty for the luminosity is 6.5% [30].

The luminosity information is stored in Luminosity Blocks (LBN). One luminosity block is typically 60 s long and is the smallest division of a data store at the Tevatron. These stores are divided into different Runs, which then consist of LBNs.

Integrating over every LBN gives the delivered luminosity of the accelerator. The interesting parameter based on this luminosity is the actually measured, good and recorded luminosity, meaning the events actually recorded on tape.

4.3.2 Triggers

The single proton and anti-proton bunches are by default 396 ns apart. This leads to a typical rate for the collisions at the interaction points of about 1.7 MHz. This rate is far too high, if one takes into account how much data would be delivered for every collision. Therefore the rate of recorded events has to be constricted to a manageable value. The operating rate for the DØ detector is 50Hz.

In order to succeed, the data has to be selected through various steps. These trigger levels (L1, L2, L3) select data based on different criteria and inputs.

The Level 1 trigger (L1) is a plain hardware trigger. Information on transverse energy deposition in the calorimeter as well as tracks of a certain p_T in the muon chambers are used. The second trigger level (L2) with its micro processors is able to perform a simple reconstruction and identification of physical objects itsself. The third an last Trigger Level, the L3 trigger, is a complete software trigger which performs a complete reconstruction of the event.

Both of the two "software trigger" L2 and L3 are constantly under development which leads from time to time to an update of the trigger software In addition a constant development is performed for the different triggers in oder to account for new physics requirements and changes in luminosity. This development is shown in the different trigger lists, in which the complete information about the different trigger types and requirements for the different runs can be found[64].

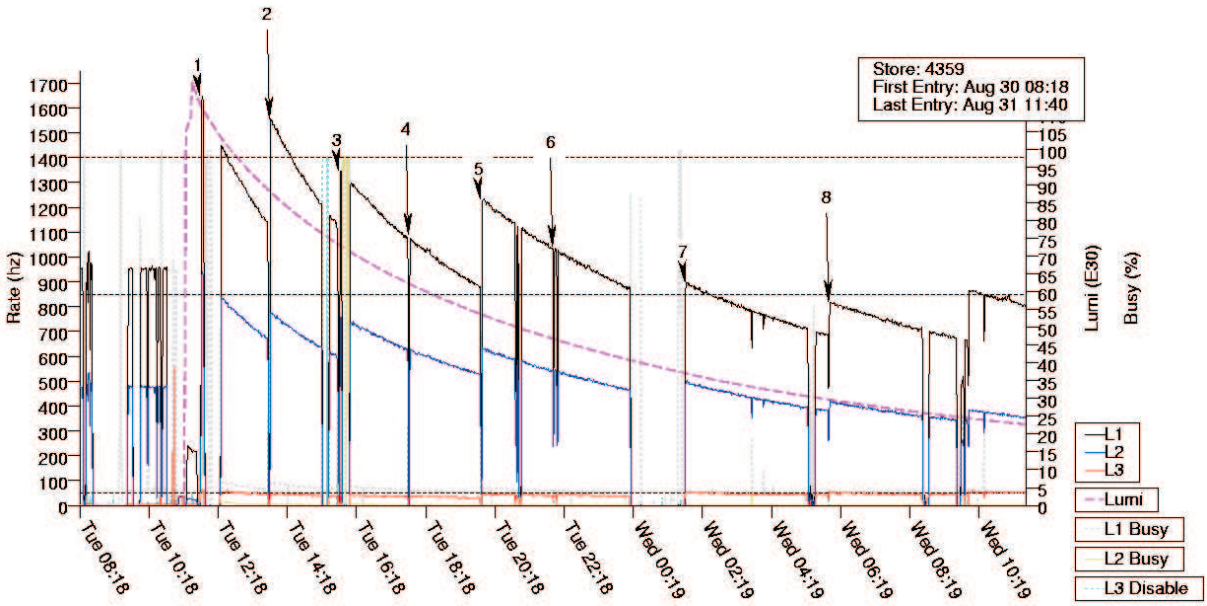

Figure 4.12: Plot for the Eventrate (left ordinate) and Luminosity (right ordinate) during a store. The different Runs are distinguishable due to their prescales[70]

Figure 4.12 shows the effects of the different trigger levels on the event rates. It is clearly to be seen, that the Level 3 rate is always below the required rate of 50Hz. The Plots shows a few other features constricting the

Level 1 and Level 2 rates during the store. The Lines at 1400 Hz and 850 Hz are restrictions for the upper frequency of the first two triggers L1 and L2 respectively.

Since the Luminosity shown as the pink line in Figure 4.12 is decreasing during the run one can simply use suppression or prescale factors. If the system of triggers should not be able to decrease the rate to the required 50Hz a prescale is used to deliver only every `nth` event even though the trigger requirement was met. Figure 4.12 displays very well how the prescales are adapted to the decreasing luminosity during the complete store.

Every change of these prescale factors marks the end of a run and is connected to an increase in the Level 1 rate.

Chapter 5

Single Excited Muon Production and Decay

The hierarchical structure (Fig.2.3) of the fermion families is one of the unsolved aspects of the STANDARD MODEL; it could be taken as an indication of quark and lepton substructure. Just as there exist "excited" states of mesons and baryons one could expect similar excited states of quarks and leptons to be produced at high energy collisions due to their compositeness. According to this substructure approach, a quark or lepton could be a bound state of three fermions [1, 7] or a fermion and a boson [2, 7]. In many such models, quarks and leptons are composed of scalar and spin-1/2 particles. These assumed constituents of quarks and leptons are usually refered to as *preons*, which are, in composite models, bound by a new strong interaction. This new interaction is often compared to QCD (Sect. 2.2.3) and would likely have similar properties: specifically non-abelian, asymptotic freedom, and infrared confinement.

Due to the underlying substructure, compositeness models [5, 7] give rise to a large spectrum of excited states [5, 6, 7]. Searching for the lowest excited states could thus give a rather direct clue to the preon hypothesis. The existence of a four-fermion contact-interaction(CI) (Fig. 5.1) would be a sign of new physics beyond the SM. Contact interactions are thought to be the lowest energy signal of quark and lepton substructure [32].

In the following an overview on the excited muon's theoretical basics are given.

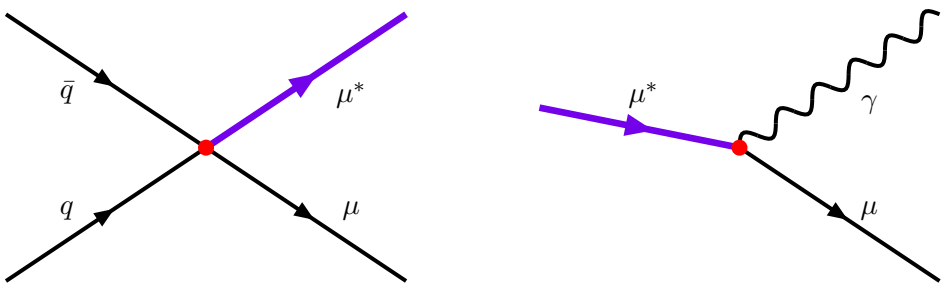

Figure 5.1: L: 4-Fermion interaction; R: Electroweak decay mode "$\gamma\mu$"[6, 61].

5.1 Excited Muon Models

Two mechanisms can contribute to excited muon production: Contact interaction (CI) and gauge mediated (GM) processes. Both models consider excited muons to be particles with spin and weak isospin equal to

$\frac{1}{2}$. In both cases the assumption is made that the excited muons do not differ from excited electrons except for their masses.

In this analysis only single production of excited muons via CI and the electroweak decay into muon and photon is considered (Fig. 5.1).

The CI model describes a particle reaction in which the underlying *preons* interact with one another. For energies below the compositeness scale Λ, these interactions can be described through an effective four-fermion Lagrangian [6]:

$$\mathcal{L} = \frac{g^2}{2\Lambda^2} j^\mu j_\mu \tag{5.1}$$

with the fermion current

$$j^\mu = \eta_L \bar{f}_L \gamma_\mu f_L + \eta'_L \bar{f^*}_L \gamma_\mu f^*_L + \eta''_L \bar{f^*}_L \gamma_\mu f_L + H.C + (L \to R) \tag{5.2}$$

and f and f^* representing the SM and excited fermions, respectively. In the calculations given in [6], g^2 is set to 4π and the η factors are set to one. For our application we obtain:

$$\mathcal{L} = \frac{g^2}{2\Lambda^2}([\bar{q}_L \gamma^\mu q_L][\bar{\mu^*}_L \gamma_\mu \mu_L] + (L \to R)) \tag{5.3}$$

The Lagrangian for gauge interactions involving leptons can be written as [6, 8]:

$$\mathcal{L} = \sum_{V=W^\pm,A,Z} \frac{e}{\Lambda} \bar{f^*} \sigma^{\mu\nu} (c_{V f^* f} - \gamma^5 d_{V f^* f}) V_{\mu\nu} f \tag{5.4}$$

with the vector boson fields $V_{\mu\nu}$, the leptons (excited leptons) l(l^*), and the coupling constants

$$c_{\gamma\mu^*\mu} = d_{\gamma\mu^*\mu} = F T_3 + F' \frac{Y}{2} \tag{5.5}$$

$$c_{Z\mu^*\mu} = d_{Z\mu^*\mu} = F T_3 \cot\theta_w - F' \frac{Y}{2} \tan\theta_w \tag{5.6}$$

$$c_{W^\pm\mu^*\nu} = d_{W^\pm\mu^*\nu} = \frac{F}{2\sqrt{2}\,\sin\theta_w} \tag{5.7}$$

$T_3 = -\frac{1}{2}$ is the third component of the weak isospin and $Y = -1$ represents the corresponding hypercharge of the excited muon. We adopt here the common convention to set $F = F' = 1$.

5.2 μ^* Production

For masses m_{μ^*} larger than the Z mass, the gauge mediated production cross section [6, 8, 54] can be neglected in comparison to the CI cross section. For higher excited muon masses the rate for gauge mediation is about 1% compared to the gauge medaited production rate [7].

The parton-level cross section for $\mu\mu^*$ production via CI is given by [6]:

$$\hat{\sigma}(q\bar{q} \to \mu\mu^*) = \frac{\pi}{6\hat{s}} \left(\frac{\hat{s}}{\Lambda^2}\right)^2 \left[1 + \frac{1}{3}\left(\frac{\hat{s} - {m_{\mu^*}}^2}{\hat{s} + {m_{\mu^*}}^2}\right)\right] \cdot \left(1 - \frac{{m_{\mu^*}}^2}{\hat{s}}\right)^2 \left(1 + \frac{{m_{\mu^*}}^2}{\hat{s}}\right) \tag{5.8}$$

Here $\hat{s}$ denotes the center of mass energy of the $q\bar{q}$ system.

5.3 μ^* Decay

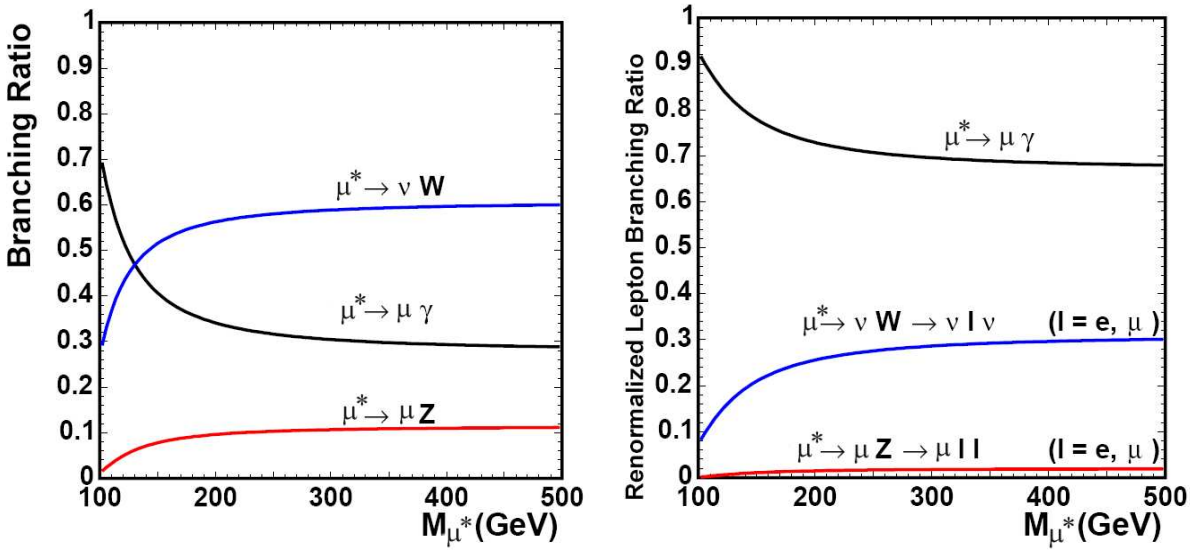

(A) (B)

Figure 5.2: (A) shows the the branching ratios for the different μ^* channels as a function of the excited fermion mass ; (B) shows the branching ratios renormalized for leptonic decays only [48]. (The branching ratios refer always to the total width of (GM) decays)

We search only for the decay mode $\mu^* \to \mu\gamma$ as illustrated in Fig. 5.1. This decay mode provides a very characteristic signal, which is not produced by many SM background processes. The only SM process producing this kind of signature in a relevant amount is $Z/\gamma^* + \gamma \to \mu\mu\gamma$. The contribution of further background processes is fairly small.

In order to calculate the branching fraction for the electroweak decay mode $\mu^* \to \mu\gamma$, the correspondig partial width and the total width must be computed.

The partial widths for the three electroweak decay modes

$$\mu^* \to \mu\gamma \quad \mu^* \to \mu Z \quad \mu^* \to \nu W \tag{5.9}$$

are given by [6]:

$$\Gamma(l^* \to lV) = \frac{\alpha}{4} c^2_{Vl^*l} \frac{m^3_{l^*}}{\Lambda^2} \left(1 - \frac{m^2_V}{m^2_{l^*}}\right)^2 \left(1 + \frac{m^2_V}{2m^2_{l^*}}\right) \tag{5.10}$$

V represents the vector bosons, and l(l^*) stands for the leptons (excited leptons), $\alpha = e^2/4\pi$ is the fine structure constant.

In the limit $m_{l^*} \gg m_V$, the overall width for gauge mediated processes is given as [6, 7]:

$$\Gamma_{GM}(\mu^* \to \text{all}) = \frac{1}{4} \frac{m^3_{\mu^*}}{\Lambda^2} (\alpha F^2_\gamma + \alpha_W F^2_W + \alpha_Z F^2_Z) \tag{5.11}$$

Here $\alpha_W = \alpha/\sin^2\theta_w$ and $\alpha_Z = \alpha_W/\cos^2\theta_w$. For F=F'=1 one can assume $(F_\gamma, F_W, F_Z) = (-1,\ 0.707,\ -0.269)$

Figure 5.2(A) shows the relative branching ratios of the three gauge mediated decay modes. For high excited muon masses the branching ratio for the channel $\mu^* \to \mu\gamma$ becomes constant at 0.3. In order to obtain a

clean signature with low background from the other two decay modes one would prefer leptonic decays like $Z \to ee/\mu\mu$ and $Z \to ee/\mu\mu$, but the respective branching ratios are quite low:

$$BR(Z \to ee/\mu\mu) = 0.0336$$
$$BR(W \to e\nu/\mu\nu) = 0.107.$$

These channels are obviously not as promising as the muon+photon channel (compare Fig. 5.2(B)). Even if the W decays leptonically, the signature would include two neutrinos, which is surely neither unique nor simple to detect. Therefore $\mu^* \to \mu\gamma$ is obviously the best choice for the μ^*-search.

Also CI decays $\mu^* \to \mu + f\,\bar{f}$ contribute significantly to the total width.

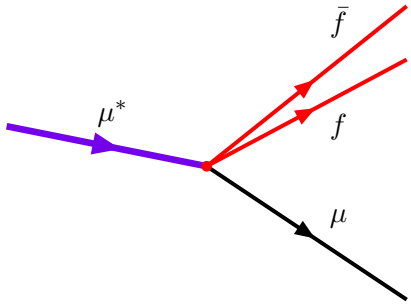

Figure 5.3: Contact Interaction Decay Mode, f and $\bar{f}$ representing fermions[6, 61].

The partial width is given for each decay mode by [6]:

$$\Gamma_{CI}(\mu^* \to \mu + f\,\bar{f}) = \frac{1}{96\pi}\frac{m_{\mu^*}^5}{\Lambda^4} \cdot N_C \cdot S \tag{5.12}$$

with color factor N_C (3 for quarks and 1 for leptons). S is a combinatorial factor:

$$S = 1 \quad \text{for} \quad f_{ermion} \neq \mu \tag{5.13}$$
$$S = 2 \quad \text{for} \quad f_{ermion} = \mu \tag{5.14}$$

Table 5.1 as well as Fig. 5.4 give an overview on the branching ratios.

$m_{\mu*}$	Γ_{GM}/Γ_{tot}	Γ_{CI}/Γ_{tot}
100	0.08 (0.97)	0.92 (0.03)
300	0.08 (0.80)	0.92 (0.20)
500	0.08 (0.59)	0.92 (0.41)
700	0.08 (0.42)	0.92 (0.58)
1000	0.08 (0.26)	0.92 (0.74)

Table 5.1: Branching ratios via gauge and contact interactions are shown, for $m_{\mu^*} = \Lambda$ and $\Lambda = 2$ TeV (in parenthesis).

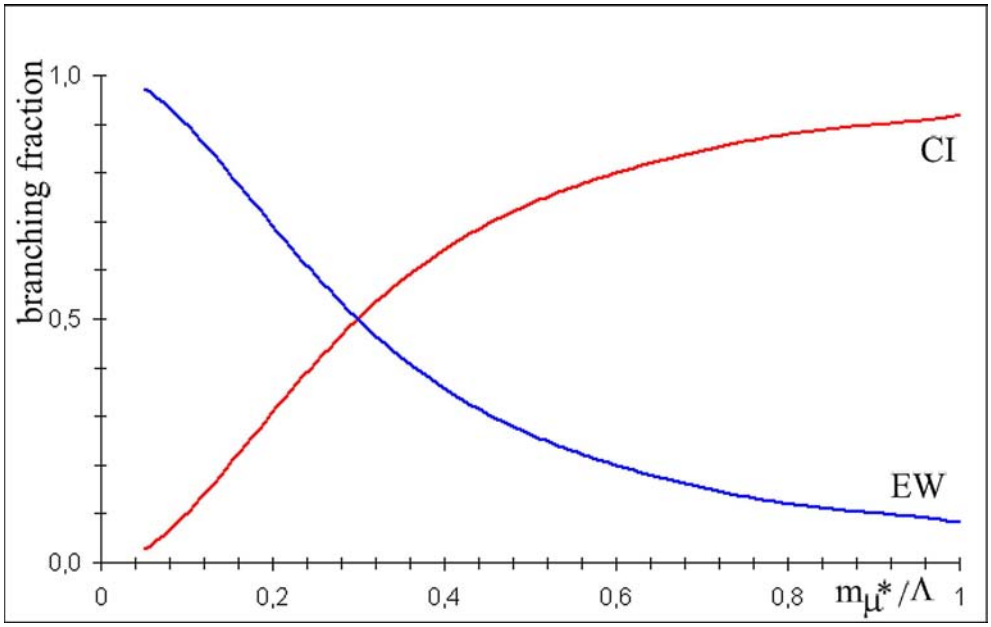

Figure 5.4: The plot shows the dependency of the branching ratio of CI and electroweak decay on m_{μ^*}/Λ

5.4 Other Excited Lepton Results

In the following a few results from excited lepton searches and analyses concerning compositeness are summarized. These results are taken from [54] and are all given at 95% CL.

Limits on Pair Production of Excited Leptons
The limits on excited electron pair production are deduced from the process

$$e^+e^- \rightarrow e^*e^*$$

via gauge coupling and assume a dominant decay into the channel $e^* \rightarrow e\gamma$, if not stated otherwise. The newest limit given from in [54] from OPAL [55] is

$$m_{e^*} > 103.2$$

GeV, with the assumption of F=F'.

The limit on excited muon pair production is given in the same paper[54, 55], originating from the process

$$e^+e^- \rightarrow \mu^*\mu^*$$

leading to

$$m_{\mu^*} > 103.2$$

.

Limits on Single Production of Excited Leptons
The newest limit on excited electron production come from the CDF collaboration [80]. in the channel $q\bar{q} \rightarrow ee^*$. This analysis performed a search for excited electron via the CI and EW production. The used decay channel in both cases is $e^* \rightarrow e\gamma$. The exclusion Limits for the CI model is

$$132GeV < m_{e^*} < 879GeV$$

for $m_{e^*} = \Lambda$, while the limit in the gauge mediated model the limit is given as

$$126GeV < m_{e^*} < 430GeV,$$

for $F/\Lambda = 10^{-2}GeV^{-1}$ This CDF result assumes dominant gauge mediated decays. In chapter 10 a more detailed comparison between the CDF limit and the presented result is given.

The latest result given in [54] from

$$e^+e^- \rightarrow ee^*,$$

for $F = F' = \frac{\Lambda}{m_{e^*}}$ is

$$m_{e^*} > 255GeV.$$

The latest result concerning excited single muon production is

$$m_{\mu^*} > 190GeV,$$

at $F = F' = \frac{\Lambda}{m_{\mu^*}}$.

These results show that, even though quite a lot of searches have been performed, there is still room for improvement. The high energy hadronic machines like the Tevatron and especially the LHC are candidates for covering more and more of the parameter space for excited lepton states.

Chapter 6

Monte Carlo Samples

In the following an overview is given, on the used generator taken to produce the Monte Carlo for the SM-process samples in this analysis. The Monte Carlo generator (`Pythia`) will be introduced as well as the detector simulation of the DØ experiment. In addition a section is dedicated to the generation of excited muon signal Monte Carlo based on a customized version of `Pythia`.

6.1 Pythia, Monte Carlo Generator

`Pythia` 6.2 [33] is a program for the generation of high-energy physics events, i.e. for the description of collisions at high energies between elementary particles such as e+, e-, p and $\bar{p}$ in various combinations. Pythia contains theory and models for a number of physics aspects, including hard and soft interactions, parton distributions, initial and final state parton showers, multiple interactions, fragmentation and decay. They are largely based on genuine research, but also borrow many formulae and other knowledge from the literature.

The physics in `Pythia` is gradually further developed in a number of directions. Additionally, the major current project is the complete rewriting of PYTHIA in C++, while all previous versions have been in Fortran 77.

The `Pythia` program is frequently used for the event generation at high energy physics experiments. Especially at the Tevatron with its 1.96 TeV multiple particle production needs to be simulated correctly. This typically includes processes where the strong force is involved directly or indirectly.

At current luminosities particle multiplicities can reach a few hundred and this number will increase for the future collider experiments. Pythias goal is to simulate whole events as accurate as the experimentally observable ones as far as the processes and the underlying physics are understood. The physics processes can be quite complex and a direct comparison between theory and experimental data can be quite a task. Therefore in order to simulate them one has to divide the physics processes into manageable tasks. The physics could be summarized like in the following:

1. Initially two beam particles (e.g. protons and anti-protons) are coming in toward each other. Normally each particle is characterized by a set of parton distributions, which defines the partonic substructure in terms of flavour composition and energy sharing.

2. One shower initiator parton from each beam starts off a sequence of branchings, such as $q \rightarrow qg$, which build up an initial-state shower.

3. One incoming parton from each of the two showers enters the hard process, where then a number of outgoing partons are produced, usually two. It is the nature of this process that determines the main characteristics of the event.

4. The hard process may produce a set of short-lived resonances, like the Z and W gauge bosons, whose decay to normal partons has to be considered in close association with the hard process itself.

5. The outgoing partons may branch, just like the incoming did, to build up final-state showers.

6. In addition to the hard process considered above, further semi hard interactions may occur between the other partons of two incoming hadrons.

7. When a shower initiator is taken out of a beam particle, a beam remnant is left behind. This remnant may have an internal structure, and a net color charge that relates it to the rest of the final state.

8. The QCD confinement mechanism ensures that the outgoing quarks and gluons are not observable, but instead fragment to color neutral hadrons.

9. Normally the fragmentation mechanism can be seen as occurring in a set of separate color singlet subsystems, but interconnection effects such as color rearrangement may complicate the picture.

10. Many of the produced hadrons are unstable and decay further.

This physics are usually simulated in three components.

The first components simulate the $2 \rightarrow 2$ hard process. Two partons from the incoming beam particles interact and leave behind two final state partons. The kinematics are calculated, based on leading order matrix elements. A typical process for example would be the process

$$q\bar{q} \rightarrow Z \rightarrow \mu\mu.$$

This simulation depends on the accuracy of the pdf[1] since one uses hadrons as beam particles.

The second component simulated by `Pythia` is modeling pertubative corrections. These corrections are typically based on pertubative calculations. Since these higher orders are difficult to calculate this is a most crucial component of the event simulation.

These higher order corrections could be gluon initial and final state radiation or final state photons from a charged particle like the electron. `Pythia` therefore only models these processes using so called "parton showers". Here branchings of one parton into several particles are described by approximating the full matrix-elements. This leads to quite reasonable agreement with the correct theoretical approach but has its deficiencies, when it comes to high jet multiplicities.

The last part is including the hadronisation, as mentioned in section 2.2.3. The quarks cannot exist freely and therefore have to fragment into enough quarks to build up colorless mesons and baryons. This is done with the string fragmentation model (sec.3.1.2)

In Addition to these hard processes, `Pythia` also takes care of the physics taking place beside this, like beam remnants, multiple interactions. An interesting insight into `Pythia` can be found at [31].

[1] Particle Density Fuction

6.2 The DØ Detector Simulation

`Pythia` generates events on the particle level, that is "particle jets" and leptons. These events are describes as if they were measured by a perfect detector without any deviations or resolution effects. The actually interesting objects are the objects reconstructed by the detector.

To simulate the effects of the detector, one has to simulate the interactions of the particle with the detector materials. Assuming a "particle" jet which contains a number of different hadrons: These hadrons obviously cross the detector material and have to build a hadronic shower inside of the calorimeter, due to their interaction with the material. It is therefore crucial to simulate the showering process, as well as the other interactions. This would be performed in a way that represents the actual detector response, as well as the effects of the magnetic field on the charged particles emerging from the generator or the processes later on.

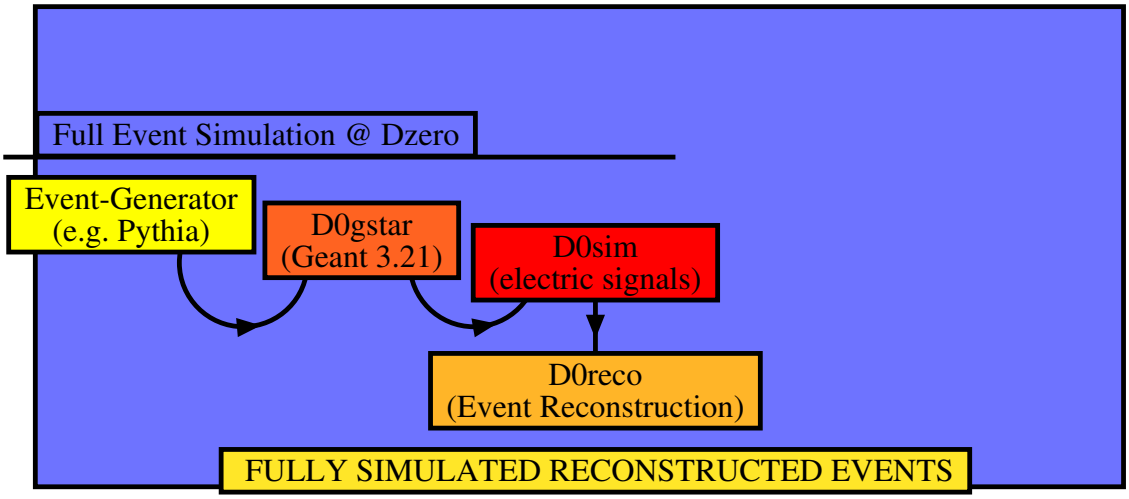

Figure 6.1: Monte Carlo Event Simulation and Reconstruction [46]

The complete simulation [46] consists of a chain of programs serving different purposes. Starting with the event generation the generator data is given to the simulating programs D0gstar [46] and D0sim[44, 46]. D0gstar[43, 46] is a program based on GEANT 3.21 [45, 46]. This part of the simulation determines the movement as well as the energy deposition of the particles inside of the actual detector. This is done by means of a software model detector, containing information about all components of the real detector and the materials used.

In the following the D0sim program simulates the electrical responses that would cause the energy depositions simulated by the D0gastar program, it also merges the hard scattering events with so called "minimum bias" events, and adds noise effects of the detector subsystems.

After this complex simulation the event data is now compiled into a form compatible with the reconstruction software of the DØ detector, which reconstructs the events like genuine data. The MC events are handled like normal data and contain the same informations.

The trigger is the only component of the detector which is not simulated. Therefore one has to correct the Monte Carlo events for the (in)efficiencies of the trigger requirements during the analysis.

6.3 Standard Model Background

$Z/\gamma^*(+\gamma)$, $Z + Z$ and $W + Z$

Three SM processes have to be considered, which produce also a dimuon plus photon signature.

6.3.1 $Z/\gamma^*(+\gamma)$

The first and also largest background is the $Z + \gamma$ production, which is discussed in connection with the Drell-Yan processes as $Z/\gamma^* + \gamma$ processes. Below in Fig. 6.2 the leading order Feynman diagrams for these processes are given. $Z+\gamma$ production can occur as initial state radiation from an incoming quark (Fig. 6.2 (A)(B)) or through final state radiation as it is shown in Fig. 6.2 (C), where one of the outgoing muons could emit a photon. But this is only the case for very high energetic muons.

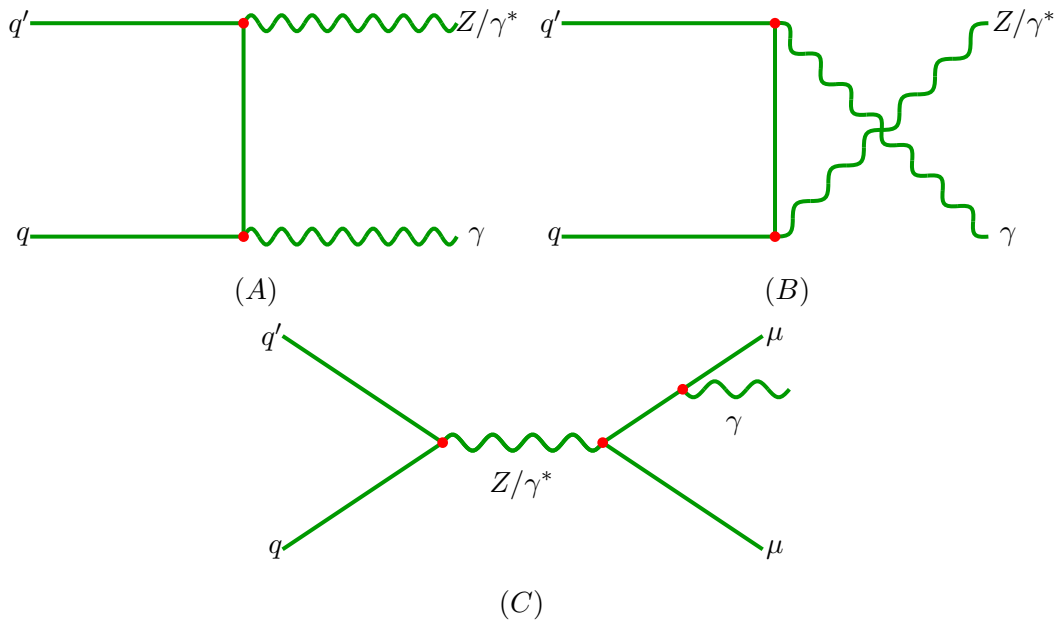

Figure 6.2: $Z/\gamma * +\gamma$ production including bremsstrahlung (final state radiation).

6.3.2 $W + Z$

The inclusive $W + Z$ production accounts for background events if the W boson decays in the electron channel

$$\begin{aligned} W &\rightarrow e\,\nu \\ Z &\rightarrow \mu\,\mu \end{aligned}$$

and the electron is misidentified as a photon due to the lack of a matching track which can be caused by the central tracking device. These processes represent a small background for the searched signature which is quite negligible in the final selection.

In this analysis an inclusive sample is used for the background description which includes jets and photons from initial and final state radiation, and therefore might quite easily produce such a background signature even without the W decaying into electron and neutrino.

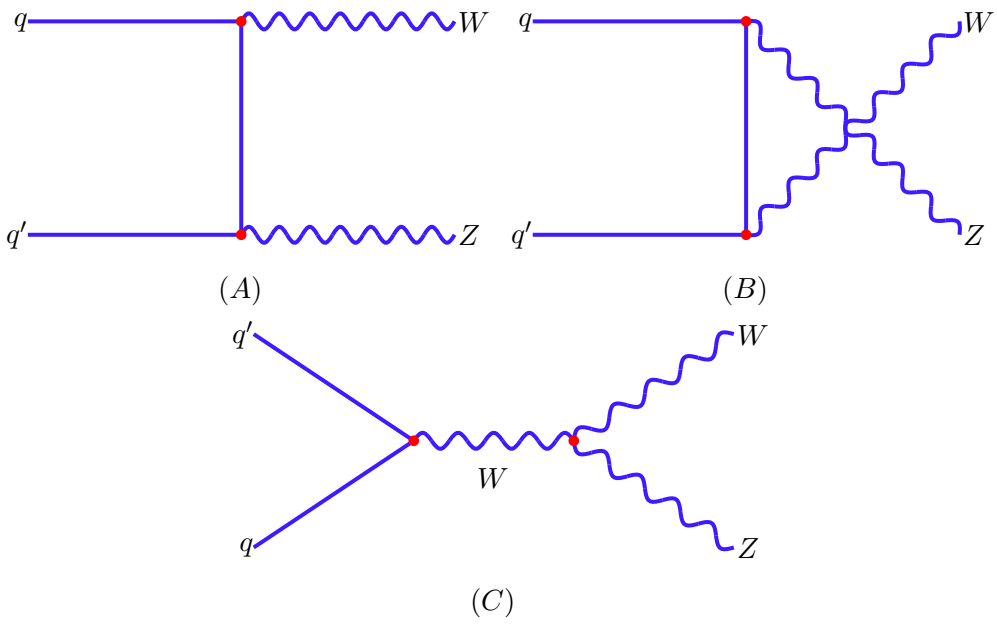

Figure 6.3: $W + Z$ production, leading order, exclusive diagramms

6.3.3 $Z + Z$

Like the above mentioned $W + Z$ production, $Z + Z$ events can be a source for background events. Inclusive production of Z+Z is assumed, including Z bosons decay into electrons. Z+Z can alone give rise to the $\mu\mu\gamma$ event signature, since one Z could decay into the electron channel and fake the extra photon. Fig 6.4 illustrates how Z+Z production is described by Feynman diagrams.

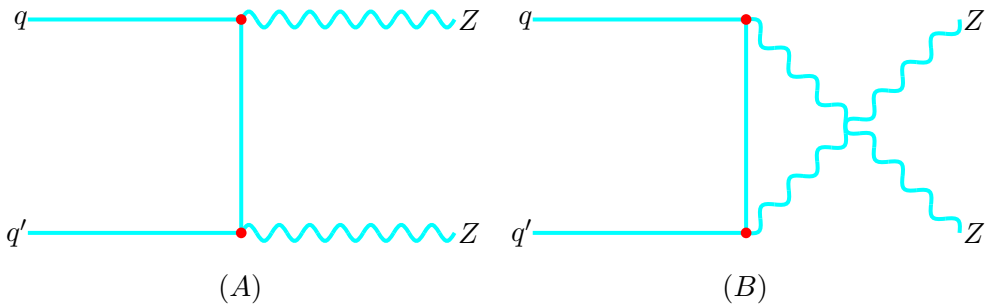

Figure 6.4: $Z + Z$ production, leading order, exclusive diagrams

6.3.4 DØ-Samples

For the background estimation a set of official DØ SM Monte Carlos generated with the event generator `Pythia` [33, 71] is used, produced with CTEQ4L/5L [35] Parton Density Functions. The samples are

"Sample"	SM Background samples		
	$\sigma_{prod} \times BR$[pb]	k-factor(NNLO/LO)	events
$Z/\gamma^* \to \mu\mu$ incl. 5-15 GeV	3558 (LO)	1.30	219250
$Z/\gamma^* \to \mu\mu$ incl. 15- 60 GeV	336 (LO)	1.30-1.36	432000
$Z/\gamma^* \to \mu\mu$ incl. 60-130 GeV	183 (LO)	1.36-1.39	460000
$Z/\gamma^* \to \mu\mu$ incl. 130-250 GeV	1.37 (LO)	1.41	10000
$Z/\gamma^* \to \mu\mu$ incl. 250-500 GeV	0.115 (LO)	1.41-1.39	18500
$Z/\gamma^* \to \mu\mu$ incl. >500 GeV	0.0047 (LO)	1.39-1.37	9500
WZ incl.	3.96 (NLO)	-	53000
ZZ incl.	1.56 (NLO)	-	53500

Table 6.1: SM background processes and their respective cross sections. In the analysis the Z/γ^* LO cross sections are multiplied by a k-factor, depending on the generated Z/γ^*-mass generated [38].

weighted with respect to luminosity and leading order cross section (`Pythia`).

The Monte Carlo weights are based on the LO cross sections from `Pythia` [33], except for WZ and ZZ, these are taken from [53].

These samples are all inclusive samples in the sense that they all include initial and final state radiation. In the analysis a Z/γ^*-mass dependent k-factor [38] is applied, leading to NNLO cross section. In addition other efficiency corrections [49] (Sect. 8.2) are applied.

The main sample is $Z/\gamma^* \to \mu\mu$ (60-130 GeV), since the $Z/\gamma^* + \gamma$ background is included and the Z-peak is by far the most dominant feature in the background of the DiMuon selection. But for high Excited Muon masses even this background is fairly small.

To correct the MC samples for the dimuon trigger efficiency, the top_trigger package [62] is used.

6.4 The Customization of Pythia

In this section some insights are given into the customization of `Pythia`, in order to implement excited muons. This is necessary because only the excited electron(e^*) production is already part of Pythia. In order to produce signal Monte Carlo, one needs single excited muon production as well as its decay modes.

The Implementation is shown schematically in Figure 6.5 and details are given in App. B.

6.4.1 Excited Muons in Pythia

There are a few things one might want to keep in mind regarding the introduction of an excited muon into the `Pythia` code:

1. What are the differences between original e^* `Pythia` events and custom μ^* events?
2. Which `Pythia` version should be used ?
3. How does the DØ framework handle such events?

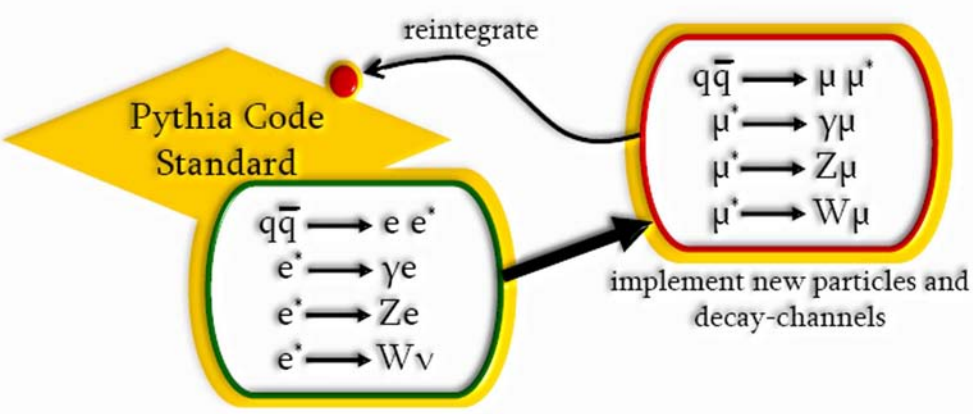

Figure 6.5: Schematic of how to customize `Pythia`

1. The main Task for producing an excited muon in the `Pythia` environment is the introduction of a new particle μ^* and of course its subsequent decay channels as well as the production process due to contact interaction. All of these routines can easily be taken from the existing e^* subroutines because in the used model [6], the production cross section of

$$q\bar{q} \rightarrow \mu\mu^*$$

is only dependent on the scale factor Λ and the excited lepton mass m_{l^*} (with $\hat{s}$ the effective center of mass energy of the $q\bar{q}$ system):

$$\hat{\sigma}(q\bar{q} \rightarrow \mu\mu^*) = \frac{\pi}{6\hat{s}}\left(\frac{\hat{s}}{\Lambda^2}\right)^2\left[1+\frac{1}{3}\left(\frac{\hat{s}-{m_{\mu^*}}^2}{\hat{s}+{m_{\mu^*}}^2}\right)\right]\cdot\left(1-\frac{{m_{\mu^*}}^2}{\hat{s}}\right)^2\left(1+\frac{{m_{\mu^*}}^2}{\hat{s}}\right) \tag{6.1}$$

2. For a correct description of the excited lepton cross section production via contact interaction one should use a `Pythia` version above 6.211. All earlier versions implement the cross section with an additional factor of two due to a misinterpretation of production modes. One also should be aware that Pythia does only simulates gauge decays and therefore the resulting branching ratios have to be adapted for a complete description according to Section 5.3

3. The integration of `Pythia` into the DØ framework introduces some additional problems when trying to integrate the complete code. Some of the `Pythia` routines are already included into the detector simulation D0gstar and have to be extracted from the customized code [37]. After the extraction of these subroutines,in order to avoid collision with the DØ-Framework and the Detector simulation, the customized `Pythia` can be compiled and used without any further problems.

In a comparison of e^* and μ^* events in the `Pythia` log files and on generator level root trees, no obvious deviations between both excited states have been found.

6.4.2 Using the Customized `Pythia`

The use of this "new" `Pythia` is in no way different from the common one, if the new subprocesses and particles are taken into account. It would indeed be possible to use this version with all the normal processes, since no changes have been made to the other parts of the `Pythia` code.

- New particle 4000013 (μ^*) ; New subprocess : 170 ($q\bar{q} \rightarrow \mu\mu^*$)
- New decay channels : 7998, 7999, 8000 ($\mu^* \rightarrow \mu\gamma$, $\mu^* \rightarrow \mu Z$, $\mu^* \rightarrow \nu W$)
- introducing necessary parameters for particle decay, cross section etc. to the parameter "arrays"

6.5 Signal Samples

The Monte Carlo samples for the excited muon's electroweak decays are generated with the customized `Pythia 6.225`, based on the CTEQ5L parton density function and LO cross section (App. 6.4). All samples are generated on the DØ analysis cluster cluedØ and are run through the full DØ detector simulation, including the full reconstruction. (D0gstar, D0sim, and D0reco p14.05.02) (sec. 6.2).

For each mass value around 10,000 events are produced (Tab. 6.2).

mass(μ^*)[GeV]	produced signal		
	$\sigma_{prod}(LO)$[pb]	BR(GM)	# events
100	38.2	0.73	11100
200	20.5	0.35	11100
300	10.5	0.31	10800
400	5.06	0.30	12000
500	2.14	0.30	12000
600	0.89	0.30	11400
700	0.35	0.30	12900
800	0.12	0.30	12600
900	0.04	0.30	8400
1000	0.01	0.30	9900

Table 6.2: σ_{prod} , BR and number of produced signal events . The compositeness scale Λ is set to 1000 GeV for this calculation. The leading order cross sections are taken from `Pythia` [33, 37]. The BR refers to the decay $\mu^* \rightarrow \mu\gamma$.

6.5.1 NNLO Corrections to the Signal Monte Carlo

k-factors for σ_{prod}					
mass(μ^*)[GeV]	NLO	NNLO	mass(μ^*)[GeV]	NLO	NNLO
100	1.366	1.430	600	1.258	1.413
200	1.373	1.468	700	1.229	1.392
300	1.352	1.468	800	1.201	1.367
400	1.321	1.456	900	1.173	1.341
500	1.289	1.436	1000	1.144	1.312

Table 6.3: NLO and NNLO k-factors for Excited Muon production. [39, 40]

The NLO and NNLO corrections (Tab. 6.3) for these processes are basically the same as for Z/$\gamma*$. They differ due to details depending on the coupling mechanism [39]. The k-factors have been calculated [39, 40] for the single excited muon production in equation 6.1.

6.5.2 Limitations concerning the Signal Monte Carlo

- Pythia only implements leading order excited muon production therefore higher order corrections to the production cross sections [39] have to be calculated.
- The choice of the structure functions $(p, \bar{p})$ has influence on the cross section which varies about 10% for different choices.
- Model dependencies of production and decay modes(5) are not really taken into account since this analysis uses a basic four fermion concept. The production of excited muons might very well depend on the underlying substructure (compositeness).

Limitations due to the use of `Pythia`:

- no gauge mediated production of μ^* is considered.
- no "CI"-like decays (due to the preon substructure) are simulated.
- this analysis only uses the $\gamma\mu$ channel with a branching fraction of $\approx \frac{1}{3}$ in the gauge mediated sector. The overall branching fraction for this decay mode, including CI decays in the calculation, strongly depends on the excited muon mass and the scale Λ (Tab. 5.1, Fig. 5.4).
- `Pythia` only implements the scale and mass dependencies of the three electroweak decay widths and the cross section of single excited muon production. The overall branching fractions must be calculated separately.

Expanding the analysis to overcome these shortcomings would require the use of another Monte Carlo generator such as CompHep/LanHep [36], in which one would have to implement the processes mentioned above.

Production via gauge mediated processes should give a rate of about 1% compared to the rate for CI-production.

Contact Interaction mediated decays indeed could, especially in the leptonic final states, give rise to a whole new spectrum of signatures and especially at collider experiments like the LHC quark final states from the CI decays could produce a significant amount of jets. Since those are not implemented in any common generator (e.g. `Pythia`) they are not used for this analysis.

CI decays at $m_{\mu^*} = \Lambda$ account for up to 93% of the decays of the excited muon which basically means that the channel with the best statistics at high masses is ignored. This opens opportunities especially for future searches as soon as the MC generators can handle these channels.

Chapter 7

Data and Monte Carlo Selection

This chapter will show which selection cuts are applied to data and Monte Carlo equally. Since the Monte Carlo samples have been explained in chapter 6 this chapter will start with an overview on the used data sample and then focus on the different selection steps.

7.1 Data Preselection

7.1.1 Data Set

The analysis is based on the data recorded by the DØ experiment between August 2002 and September 2004 The data sample corresponds to an integrated luminosity of

$$\mathcal{L} = (377 \pm 24)\ \mathrm{pb}^{-1}.$$

These events have been reconstructed with the p14 version of the reconstruction software "D0reco" [46, 47].

As described in section 4.3, every second about 50 events are recorded and reconstructed, using the Fermilab processing farm. This processing farm takes the 50Hz data stream containing events with a size of about 250kByte. The peak transfer rate is about 13 MBytes per second. The farm is reconstructing one event every 10 seconds [47].

The reconstructed events are afterwards compressed by a factor ≈ 10 and written on tape in the standard thumbnail data format (.tmb).

These data do contain all relevant physical quantities like event number and run number, energies and tracking hits as well as more advanced information like central track match for muons or jet isolation.

In order to assure an easy access to the data for every DØ user the location of the data is stored in the SAM system (Sequential data Access via Meta-data). In this system whole data sets can as easily be accessed as single files for the analysis.

The thumbnails used in this case underwent the pass2 thumbnail fixing which accounts for appliance of some corrections to the stored physics variables[72, 71]. This is basically an offline re-reconstruction of all data with improved reconstruction algorithms. In particular calorimeter noise is reduced this way.

The preselection is based on the "SKIM_2MUhighpt" data, provided by the Common Sample Group (CSG) [71] and saved as thumbnails (TMB) in the SAM database. These so called "SKIMS" are sets of events produced by the (CSG), containing preselected events stored in SAM in order to facilitate the easy use of the data sets and to reduce the size of the actually used amount of storage space for each analysis.

The SKIM used here requires at least two muons with the following criteria:

SKIM_2MUhighpt:

- 2 "loose" muons
  (*loose muon, meets 2 out of three conditions:*
  - *at least one A layer scintillator hit*
    at least two A layer wire chamber hits
  - *at least one BC layer scintillator hit*
  - *at least two BC layer wire chamber hits)*
- muons with a matched track in the central tracker
- transverse muon momentum $p_T > 15\mathrm{GeV}$
- no particular trigger requirment

This data sample contains around 180,000 events.

The data is converted into a `ROOT`[59] format with the TopAnalyze package [58] and its version "Ipanema".

7.1.2 The DiMuon Triggers

Since the final state includes two muons a set of DiMuon triggers is used. These triggers are used with a logical "or" to ensure the widest coverage. These triggers are crucial to the luminosity determination and since some of them are used in parallel, one has to be sure the same luminosity blocks are covered by each of these triggers. This is done by requiring the same Level 1 trigger in order to have the same prescale factor (sec. 4.3). The luminosity calculation is performed based on the trigger used. One cannot simply use the run duration and the average luminosity. This means that in the analysis only those events can be used, for which at least one of the chosen triggers has "fired". For this purposes the information on the fired trigger is stored together with the event data.

Since the data taking period includes about two years, the triggers have changed over time, this development can be found in the different trigger lists CMT-10.xx - CMT-13.xx [64].

The following set of dimuon triggers is used:

- `2MU_A_L2M0` (for triggerlist version CMT-10.xx and below)
  runnumber <174808
- `2MU_A_L2M0_L3L15` or `2MU_A_L2M0_TRK10` (for CMT-11.xx)
  174808 < runnumber <17822

- `2MU_A_L2M0_L3L6` or `2MU_A_L2M0_TRK5` (for CMT-12.xx)
  17822 < runnumber <194567
- `DMU1_TK5` or `DMU1_LM6` or `DMU1_2LM2` (for CMT-13.xx)
  194567 < runnumber <196585

These triggers require different Level 1,2,3 criteria:

- 2MU_A → two muons in the detector fired Level 1 scintillator trigger
- L2M0 → at least one "medium" muon found at Level 2
- L3Lx → local muon $p_T > x$ GeV or
  TRKx → track $p_T > x$ GeV requirement at Level 3

The detailed trigger requirements can be found in [64].

7.1.3 Quality Criteria and Luminosity

To perform the analysis correctly the luminosity has to be determined according to the used triggers and some data quality requirements. Only good runs are of interest for the analysis, the data quality for every run is determined. Usually the data quality of all runs is documented in the Offline Run Data Quality Database [65].

In order to ensure good data quality for the analysis events which are flagged bad or special are not used in the final analysis. The flags used for run quality in this analysis are:

- MuonQuality
  (muon system status)
- CalQuality
  (calorimeter status)
- CFTQuality
  (central fiber tracker status)
- SMTQuality
  (silicon tracker status)

In addition to theses quality criteria a list of dismissed luminosity blocks is used to exclude LBNs (Luminosity Block Number) containing events that should not be used.

The bad runs are the result of problems during the data acquisition (Global Monitoring). The bad LBN lists can be divided into two lists, first the JETMET-Bad-Luminosity block-List [66] and the "Ring of Fire" LBN list [67]. These lists account for phases with calorimeter noise where the "Ring of Fire" is a special calorimeter effect which mimics a signal due to a complete ring of active calorimeter cells.

The luminosity is calculated with the runrange_luminsoity tool [57], excluding data which corresponds to these excluded runs. This tool calculates the luminosity for a set of given triggers and run ranges within a

given data sample / skim, for triggers with the same Level 1 definition and returns a list of bad LBNs which later can be excluded.

The overall luminosity for the **SKIM_2MUhighpt** is

$$\mathcal{L} = (377 \pm 24)\mathrm{pb}^{-1},$$

as shown in Table 7.1 The error is 6.5% which is one source of the systematic error (see sect. 8.3,[30]).

Luminosity Overview				
1^{st}Run	Last Run	trigger list	luminosity[pb^{-1}]	$\sum_{version}$
162458	167015	8.2	20.28	10.28
167019	170043	9	20.48	
170230	170246	”	0.42	20.90
170247	174807	10	9.03	9.03
174845	177280	11	39.35	
177286	177312	”	0.56	
177315	177684	”	0.75	
177740	178017	”	4.45	
178080	178096	”	0.01	
178104	178559	”	12.72	
178645	178721	”	0.21	58.05
178097	178103	12	0.11	
178722	190380	”	121.06	
190381	194552	”	95.27	
194563	194566	”	0.64	217.08
194567	194573	13	1.36	
194662	196584	”	49.99	51.35
Σ_{all}				376.69 ± 24.48

Table 7.1: Luminosity split for the different triggerlists

7.2 Final Object Selection and Cuts

The final event selection requires 2 muons (Tab. 7.2), as well as an additional photon (Tab. 7.3). The cuts are chosen with respect to the considerations in section 7.3 intending to maximize the signal efficiency as well as to keep a good agreement of Data and MC and reasonable muon quality. The last requirements for the muons, concerning the track quality and the matching of local and central “track” are especially helpful to reduce the unphysical high-pt muons [50, 51].

This is a known problem, the high-pt tail cannot be described correctly, but reasonable enough. Some of the more complex cuts on the photons are performed in order to assure agreement between the Monte Carlo description and the data, and to allow the use of the photon efficiency and fake photon rate from another analysis [76].

After these selection requirements, only one last cut (Tab. 7.4, p.64), dependent on the μ^* mass, is applied to further reduce the SM background. The cut is performed on the invariant mass spectrum of the highest energetic muon and the photon.

7.2.1 Dimuon-Selection Criteria

This analysis requires two muons which are reconstructed with two different subsystems of the detector, the local muon system as well as the central tracking system. A local track inside the muon system provides the basis for the muon identification, while the central track assures the precise measurement of the p_T. This analysis uses a muon requirement as loose as possible, but to ensure good muon quality and good agreement of data and Monte Carlo, a few quality cuts have to be performed.

Muons are selected by using the cuts displayed in Table 7.2, as well as the Muon-ID group certified object identification definitions [73].

The cuts are explained further below.

DiMuon Requirements	
"medium" Quality"	
"isolated" $isolated = 1$ [58] **for at least one of the two selected muons**	"no cosmic timing cuts" $-10ns < t_{A-layer} < 10ns$ $-15ns < t_{BC-layer} < 10ns$
"transverse momentum" $p_T > 15GeV$	"pseudo rapidity" $\|\eta\| < 2.1$
"central trackmatch" $(nseg > 2)$ from `MuoCandidate` $hascentral = 1$ [58]	"track quality" central track fit: $\chi^2_{track}/dof < 3.5$ global fit : $\chi^2_{global} < 40$

Table 7.2: Dimuon requirements

"nseg $>$ 2": The nseg requirement in general describes a certain hit pattern for muons in the detector with e.g. nseg$>$ 0 standing for a muon with central track.

The nseg$>$2 requirement basically requires a track match and hits in the muon layers before (A) and after (BC) the toroid magnet. These hits are used to evaluate and fit a local track inside the muon system. This track is matched with a central track found in the central tracker.

Should the local track fit not converge, the procedure is reversed and the matching is started from the central tracker going outside to the local muon track.

An objective for this fit procedure is to generate a "global track" in order to combine all information on the muon that is possibly measured in order to determine the kinematic variables with a better resolution. Usually the central tracking detector is used to determine the muon properties since it dominates the fit due to its better resolution.

The local muon system has the function of an object identification system, to determine whether the particle which caused a track is a muon or not.

"medium" quality: The requirement of so called "medium" muons in combination with requiring a certain value for the "nseg" parameter determines how many wire and scintillator hits have to occur for this particular muon.

A medium muon with nseg>2 has at least two A layer wire hits and a minimum of one A layer scintillator hits, while the BC layer has to account for at least two wire hits and one scintillator hit. The more hits the better the local track fit, especially if there are hits before and after the toroid. The nseg>2 requirement is necessary in order to have a unique medium definition. There are parts of the detector, like the bottom hole, which could have less hits muons in this region are flagged as medium as well.

Timing cuts: The timing cuts are applied in order to reduce the cosmic muon background. The criterion is taking the time of flight based on hits in the A and BC level scintillators. To be able to reject this background one has to assure that the measured muon is actually coming from a beam collision within the detector. In order to do this, the time of flight is measured and the above mentioned cut of 10ns is applied.

The C-layer scintillators, as described in section 4.2.4, are capable of discriminating time intervals of 2.5 ns, this ensures that the muons studied really emerge from the interaction point and the real beam collision.

Even though this cut together with other track quality requirements provides a good rejection for cosmic muons, especially at high p_T cosmic muons still are an important background for the dimuon selection.

The photon requirement and the last invariant mass cut remove the last cosmics, since no events are observed in the final selection.

Pseudo-rapidity: The requirement for the pseudo rapidity range is applied to ensure that the muon is actually in the instrumented part of the muon system, since the muon system ends at $|\eta| = 2$.

Isolation: At least one muon is required to be isolated in order to reduce the QCD background, since heavy quark jets like b-jets produce muons within the cone of the jet, which are therefore normally not isolated and usually have a small transverse momentum. The second muon must not necessarily be isolated, in order to gain signal efficiency.

The isolation is a flag provided by the TopAnalyze [58] package describing the energy deposition around the muon track. The muon is flagged isolated when the following conditions are met:

- halo_p11 $< 0.08\ p_T$, where halo_p11 describes the sum of energy in calorimeter clusters in a hollow cone between $\Delta R = 0.2$ and $\Delta R = 0.4$ from the muon track. All cells of the calorimeter except the coarse hadronic cells are used in order to minimize noise effects from the coarse haronic section.
- trkcone_pt $< 0.06\ p_T$ with trkcone_pt describing the sum of p_T of all tracks withing the cone of radius $\Delta R = 0.5$ around the muon, excluding the track matched to the muon.

This leads to an isolation variable from two separate detector systems, including the tracking detector, and the calorimeter.

track quality [51, 52]: The track quality in general is meant to assure a good track fit in order to remove tracks that might mimic high p_T muons.

$\chi^2_{track}/d.o.f. < 3.5$. This cut on the quality of the central track is effective at removing in-flight decay backgrounds and poorly reconstructed tracks at higher p_T. This is basically a background from mesons, such as pions and kaons, that decay in the central tracker (in-flight decays). This produces a kinked track at the point of decay, which affects the central track reconstruction, as well as the momentum resolution. This background is reduced by this quality cut on the central track. It was shown in [51] that especially

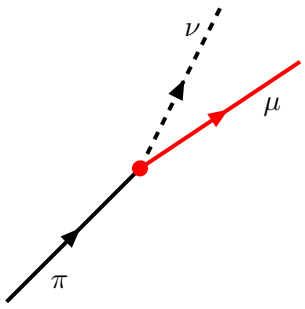

Figure 7.1: Poorly measured muon track, due to non-genuine muon.

muons with $p_T > 100$ GeV in the data show a particularly high value of χ^2 while the Monte Carlo does not reproduce this feature. This appears due to poorly measured tracks at high transverse momentum in data.

The global track-χ^2 <40 ensures a more rigid matching between the central track and the local muon system. This cut tightens the discrimination between real tracks and unphysical track matchings especially for muons with high transverse momenta. If a track cannot be assigned to a local muon with high probability the quality of the muon measurement is questionable.

Transverse Momentum: In order to use the muon trigger efficiency description of the top trigger group [62] one has to request at least one muon with p_T above 15 GeV. The cut on the transverse momentum of 15 GeV is made to suppress low energy muon signatures, since the signal itself tends to produce muons with higher energies. This cut is based on the skim requirement and leads to a well defined data sample with a reasonable file size.

7.2.2 Photon-Selection Criteria

In this section the cuts applied on the photon will be explained a bit further. Some of these cuts are taken from the analysis described in[76] in order to the photon identification efficiency and the rate for photons being misidentified jets determined in the same study [76]. An electromagnetic (EM) cluster in the central region of the calorimeter (CC) is defined as a set of activated towers in a cone with radius R=0.4 around the central tower, which is determined by an iterative cone algorithm on the basis of the tower energy content.

The towers, as have been seen in section 4.2.3, reach from the electromagnetic calorimeter up to the coarse hadronic part. Therefore in order to be qualified as an electromagnetic object, the energy deposition has to be dominated by entries in the electromagnetic calorimeter ($> 90\%$).

Photons are selected by cuts recommend by the EM-ID Group [41], which are already implemented in the TopAnalyze "EMArray" definitions. After this selection additional cuts are applied in theis analysis, which are explained in the following.

Photon Requirements	
"Isolation" iso<0.15 [58]	"no track" $spatial\_track\_c2p < 0.001$ [58]
"EM fraction" emf > 90 %	"Shower shape" $hmx7 < 50$
"transverse momentum" $p_T > 8$ GeV	"Distance to muons" $\Delta R > 0.4$
"pseudo rapidity" $\|\eta\| < 1.1$	"track-isolation" $\sum(track\_p_T) <$ 2GeV within $0.05 \leq \Delta R \leq 0.4$

Table 7.3: Photon requirements

Isolation: The search for excited muons requires a clear signature especially of the photon to suppress photons from final state radiation and QCD background sources like hadrons being identified as photons. Such background photons would be near to the hadronic energy deposition.

This leads to the necessity to ask for a reasonable isolation criterion. The isolation is defined via :

$$iso = \frac{E^{tot}(R < 0.4) \; - \; E^{elm}(R < 0.2)}{E^{elm}(R < 0.2)} < 0.15 \tag{7.1}$$

The isolation criterion describes the "cluster isolation" as displayed in Fig. 7.2 with $E^{tot}(R < 0.4)$ the total energy of the cone with radius $R = 0.4$, and E^{elm} only the electromagnetic energy inside the cone with radius R=0.2. Outside the small EM-Cone the energy deposition has to be quite small, which is the case

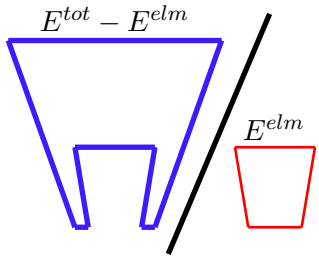

Figure 7.2: Sketch of the "cluster isolation" criterion

for a real photon. If it's a photon from hadronic processes for example, the energy deposition in the larger (blue) cone would be much bigger, which then would fail the criterion described above.

EM fraction: One of the most intuitive properties to distinguish an electromagnetic object from hadronic energy depositions is to measure the ratio of energy in the EM layers of the calorimeter and the hadronic layers, this is described by the electromagnetic fraction (EM fraction).

Every genuine EM shower is expected to deposit a large fraction of its energy inside the electromagnetic part of the Calorimeter:

$$\frac{E^{elm}(R < 0.4)}{E^{tot}(R < 0.4)} > 0.9 \tag{7.2}$$

Shower shape: Other than the energy fraction, the electromagnetic showers can be discriminated from the hadronic showers by comparison of their longitudinal and lateral dispersion. The hadronic shower is much broader and travels far deeper into the calorimeter until it is finally absorbed by the detector material after around 9 nuclear absorption lengths (λ). The electromagnetic showers are build up from Bremsstrahlung and pair production and reach their end when the last produced photon reaches an energy of two times the electron rest mass which is usually after around 20 radiation lengths (X_0). They are therefore mostly constraint to the EM calorimeter.

The evaluated variable (hmx7) is called the shower shape and is based on seven correlated variables: The four electromagnetic fractions of each EM layer inside the calorimeter, the total electromagnetic energy, the vertex position z and the transverse shower width in ϕ.

The covariance matrix of theses parameters is calculated tower wise in η using an electron Monte Carlo simulation. The inverse of this matrix is called H. Based on this matrix a χ^2-fit is performed in order to evaluate how much similarity there is compared to a genuine electron/photon shower. This analysis requires hmx7$<$50.

No trackmatch: As seen above, electrons and photons are reconstructed and identified with similar criteria. To be capable of distinguishing both, one has to evaluate the track matching criterion in the central tracker. While for electrons one would of course expect to find a matching track to the calorimeter information, the photon has no charge and therefore should normally not make a track inside the tracking detector (check Fig. 4.3).

The matching of the track in the central region is performed with a χ^2-fit:

$$\chi^2 = \left(\frac{\delta\phi}{\sigma_\phi}\right)^2 + \left(\frac{\delta z}{\sigma_z}\right)^2 + \left(\frac{\frac{E_T}{p_T} - 1}{\sigma_{E_T/p_T}}\right)^2 \tag{7.3}$$

With $\delta\phi$ and δz the distance between the extrapolated track and the position of the EM cluster at the third layer of the EM (segmentation 0.50×0.05 sec. 4.2.3). These quantities describe the spatial matching between track and calorimeter. The Energy versus transverse momentum term describes the ratio of energy deposited and measured in the electromagnetic calorimeter cluster, while the transverse momentum originates from the measurement of the matched track. The three σ_i represent the the RMS values of the experimental measured distributions.

Typically a track would count as matched if the χ^2 variable exceeds 0.01, therefore normally the exclusion of a track would require to reverse this criterion. In order to fulfill the required track exclusion necessary for the later described photon efficiency determination EM objects are only identified with photons when the χ^2 is smaller than 0.001.

The E_T/p_T requirement is used to decrease the track misidentification as can be seen in Figure 7.3. The resolution of the tracking detector declines with increasing transverse momentum. The measurement of an object with high-p_T track is more precise in the calorimeter. This means an increasing track misidentification for high momentum objects. In order to compensate this tendency the E_T/p_T criterion is decreasing this probability significantly.
Even though photons explicitly do not require any track, the more reliable the track matching criterion is, the better it is also for the reverse.

Pseudo rapidity: The geometrical cut of $|\eta| < 1.1$ is performed in the detector η which is calculated with respect to the genuine center of the detector. This is done in order to use only the best instrumented central

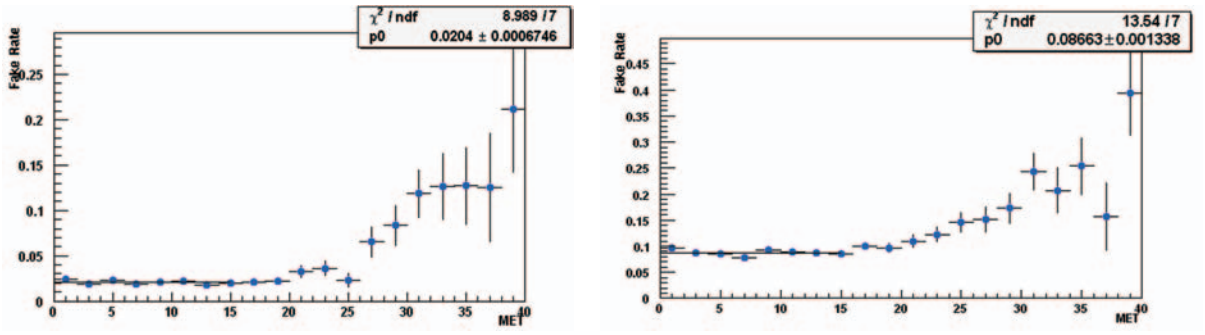

Figure 7.3: Fake rate for the track fit vs Missing Transverse Energy for the spatial track fit with (Left) and (Right) without (E/p) requirement [41]

region of the tracker for the track veto, and to comprise only photons which are measured in a homogeneous part of the detector, the CC region. This choice assures similar efficiencies for all photons taken into account for this analysis.

The EM calorimeter has cracks originating from the 32 separate modules. Photons reconstructed with energy depositions in these intermediate regions normally are excluded from the analysis. In this analysis it is assumed that the Monte Carlo describes this feature reasonably and therefore these regions are taken into account leading to a better signal efficiency.

Distance to muons and track isolation: The extra criteria $\Delta R > 0.4$ and $\sum(track_p_T) < 2$GeV (within $0.05 \leq \Delta R \leq 0.4$), on the isolation of the photon are used mainly to reduce the background emerging from QCD background due to neutral π mesons which could be mistaken as photons. These cuts are used similar as described in [76], since this analysis provides the estimation to calculate the faked photons as an additional background uncertainty.

7.2.3 The Final Cut

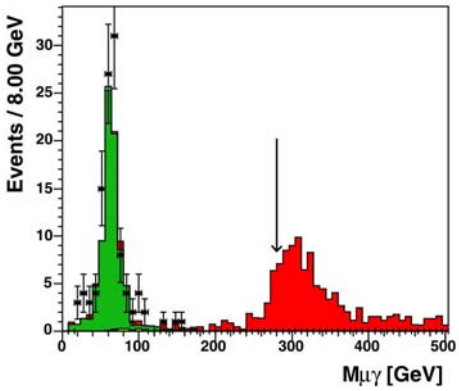

Figure 7.4: Shown is the invariant muon and photon mass for the signal point with 300 GeV excited muon mass.

This final selection cut is performed in the invariant mass spectrum of the highest energetic muon and the associated photon, as the $\mu\gamma$-mass provides a good discrimination between SM background and signal events. The signal μ^* appears as a peak in this distribution (see 7.4. A cut on the p_t of the leading photon or muon was found to be not as effective, especially at lower μ^* masses.

The choice of the mass value is based on the best $signal/\sqrt{background}$ ratio as shown in Fig. 7.5. If there happens to be some kind of plateau or more maxima, the choice was made toward better signal efficiency. This for example is the case for the signal mass of $m_{mu^*} = 200$ GeV.

Due to its relatively small invariant mass, one of the more difficult signal points is the one at 100 GeV, with a large background from $\mu\gamma$ pairs from the Z-mass region. The cut for this signal point was taken from the 200 GeV optimization, since the signal over $\sqrt{background}$ optimization itself would have given a cut value of around 400 GeV which would have decreased the signal efficiency to an intolerable level.

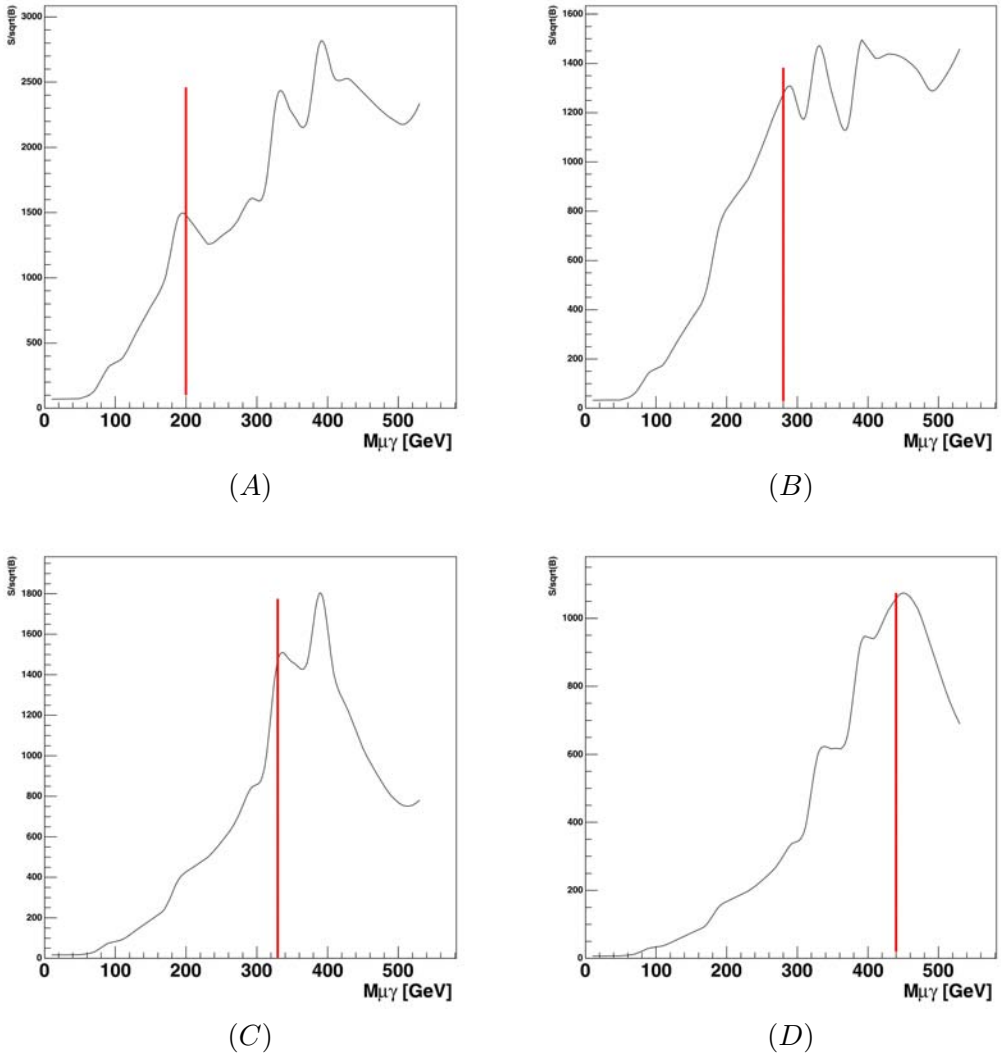

Figure 7.5: Signal over $\sqrt{background}$ ratio for signal at m_{μ^*} (A) 200 GeV, (B) 300 GeV, (C) 400 GeV and (D) 500 GeV, calculated in the invariant $\mu\gamma$ mass distribution after the kinematic fit (sec. 8.1) was applied

For every signal point above $m_{\mu^*} = 500\ GeV$ the cut was kept at a constant level to profit from the better signal efficiency.

Invariant Mass($\mu\gamma$) Cut										
Mass(μ^*)[GeV]	100	200	300	400	500	600	700	800	900	1000
Cut[GeV]	200	200	280	330	440	440	440	440	440	440

Table 7.4: Additional and Final Cut

The resulting event numbers for the different selections steps are given below, while further explanations are given in chapter 9.

Sel. →	#data dimu	#SM dimu	#data gamma	#SM gamma
MC		$\# \pm stat \pm syst$		$\# \pm stat \pm syst$
Z/γ^*	-	$24636.8 \pm 70.6 \pm 3703.8$	-	$82.11 \pm 3.84 \pm 12.6$
WZ	-	$14.9 \pm 0.6 \pm 2.1$	-	$0.15 \pm 0.06 \pm 0.02$
ZZ	-	$11.5 \pm 0.3 \pm 1.6$	-	$0.11 \pm 0.03 \pm 0.02$
$\sum$	24853	$24663.2 \pm 70.6 \pm 3707.5$	110	$82.37 \pm 3.84 \pm 12.60$ (82.37 ± 47.57)

Table 7.5: Data and SM-background events after the DiMuon and DiMuon+photon selection (with kinematic fit). The error due to faked photons (sec. 8.2.4) is applied added in parenthesis, since one cannot differentiate it for the different MCs

	Sel. →	#data final	#SM final		#data final	#SM final
Mass	MC		$\# \pm stat \pm syst$	**Mass**		$\# \pm stat \& syst$
100	Z/γ^*	-	$0.121 \pm 0.018 \pm 0.019$	**400**	-	$0.009 \pm 0.003 \pm 0.001$
&200	WZ	-	< 0.02		-	< 0.02
	ZZ	-	$0.012 \pm 0.010 \pm 0.002$		-	< 0.06
	$\sum$	0	$0.132 \pm 0.021 \pm 0.021$		0	$0.009 \pm 0.003 \pm 0.001$
300	Z/γ^*	-	$0.034 \pm 0.009 \pm 0.005$	$\geq$ **500**	-	0.002 ± 0.001
	WZ	-	< 0.02		-	< 0.02
	ZZ	-	< 0.06		-	< 0.06
	$\sum$	0	$0.034 \pm 0.009 \pm 0.005$		0	0.002 ± 0.001

Table 7.6: Data and SM-background events after the final cut on the invariant $\mu\gamma$-mass (with kinematic fit). The error due to faked photons is negligible at this stage

The WZ and ZZ sample do not have sufficient statistics, therefore an upper limit for the event number is given according to to poisson statistics, given zero observed objects [54].

7.3 The Final Cuts versus Signal Efficiency

Even though the signal efficiency with about 16% is not too low, compared to other analyses it has been a concern during the course of this analysis to understand how the signal efficiency could be improved, or why it cannot without much effort be improved further.

It would of course be of great interest to gain signal efficiency in order to get a more competitive result. Therefore it was checked if there is still potential hidden in opening certain identification / selection cuts. Several problems occurred, which averted most of the possible efficiency gains.

In the following, a short description is given of the different cut parameters which were varied and the encountered problems, leading to the final selection cuts (Sec. 7.2)

7.3.1 Concerning the "nseg" Requirement

One especially interesting parameter is the nseg requirement for the dimuon selection (Tab. 7.2), which describes the hit pattern in the muon system. It is very delicate since it is directly connected to the used trigger efficiency description [62], which is based on nseg=3 requiring measurements. Loosening this cut completely, allowing any kind of medium muons to pass the selection, would lead to a great improvement(factor 1.8) in signal efficiency. Changing this cut has a significant effect only on the MC, since the events with nseg$<$3 are cut out by the trigger routines. This improvement therefore would produce the need to recalculate the trigger efficiency for non nseg=3 muons especially in the bottom hole area of the detector, correcting for the newly added discrepancy between data and MC.

Therefore the resulting improvement might therefore is small, and the ID requirement remains at $nseg > 2$ for both muons.
Result: muon $nseg > 2$

7.3.2 Concerning the Muon Isolation

First, the muon isolation is by far the best handle to improve the signal efficiency without causing too much problematic effects. On the other hand loosening the isolation requirement for both muons causes some problems in the low pt region (QCD background). Therefore, the isolation for only one of the two muons is loosened, leading to about 10% increase in efficiency as can be seen in Tab. 7.7. Still there remains a small difference at low invariant $\mu\gamma$ mass (Fig. 9.3(A),(C)) between data and MonteCarlo, which is the result from loosening the isolation of the second muon. This can be neglected, since the region of interest for this analysis is located at much higher invariant masses.
Result: Ask for at least one muon to be isolated

Signal efficiency for different ID setups [arb. units]		
Muons isolated	$\|\eta\| < 1.1$	$\|\eta\| < 1.1$ or $1.5 < \|\eta\| < 2.2$
2	0.82	0.91
1	0.89	0.97
0	0.91	1.00

Table 7.7: Signal efficiency for different ID Cuts normalized to the most loose case(m_{μ^*}=500 GeV)

7.3.3 Concerning the Photon $|\eta|$ Range

Changing the $|\eta|$ range of the photon selection leads to about $\sim$10% improvement (Tab. 7.7), but for this area of the Tracker usually no corections due to efficiency or acceptance effects are calculated and therefore an adjustment would have to be made to compensate for these effects.
Result: $|\eta| < 1.1$

7.3.4 Conclusion

The signal efficiency is still quite "low", but after all the above mentioned changes the signal efficiency is improved by about 10% compared to earlier stages of this analysis. Adjusting all other cuts would take a lot more effort and cannot be done in the range of this analysis and wont't lead to a huge improvement in the excited muon mass limit.

Without going into details, the signal efficiency for the $\gamma\mu$ channel evolves as follows:
after DiMuon selection:$\sim$28% $\rightarrow$ after Photon selection:$\sim$18% $\rightarrow$ after final Cut:$\sim$16%

Chapter 8

Detector Effects and Systematic Uncertainties

8.1 Kinematic Fit

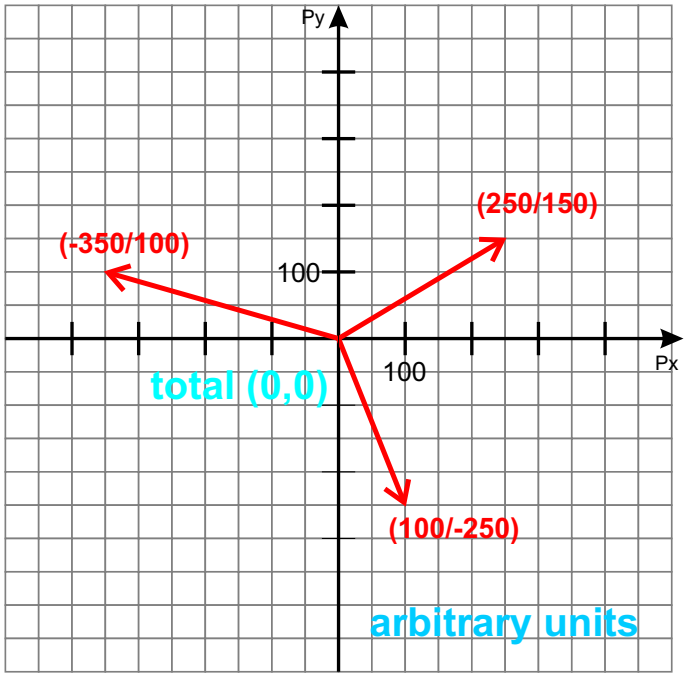

Figure 8.1: Shown is the momentum configuration of the toy model before the gaussian smearing.

The Kinematic Fit is a tool to improve the resolution of kinematic variables due to the use of extra constraints. Especially high energetic muons in this analysis suffer from a big uncertainty as described on page 32. The resolution of the DØ muon system is the most limiting factor (the transverse momentum resolution [73] for momenta above 500 GeV can be as much as 100%, concerning cuts and invariant mass resolution.

In this Analysis the knowledge about the p_T balance is used, meaning that the momenta of emerging particles should be balanced in the x-y-plane. The reason for this is obvious, since the beams at the beginning have no transverse momentum component.

To prove the viability of the approach a toy model has been used. This is presented before the actual effect on the analysis is shown.

8.1.1 Toy Model

The toy model assumes three particles. The direction is known in the x-y-plane given via the angle ϕ and the value of p_T. Since the angles are measured most accurate the direction remains unchanged, while the transverse momentum is smeared by a Gaussian. The p_T is used as the mean of a Gaussian dice and the new value is used as the input value for the fit procedure. For this example a fictional measurement of p_T has been performed 10^7 times based on the exact input momenta. This "measured" data is then undergoing the fit algorithm. Both the "diced" (measured) momenta and the fitted ones are plotted below.

Toy Model Setup
For this particular example the values of ϕ and p_T are given below in arbitrary units and the geometrical setup is shown in Figure 8.1.

- $\phi_{(1)}$=5.09
- $\phi_{(2)}$=2.86
- $\phi_{(3)}$=0.54
- $P_{T(1)}$=291,5
- $P_{T(2)}$=364,0
- $P_{T(3)}$=269,3

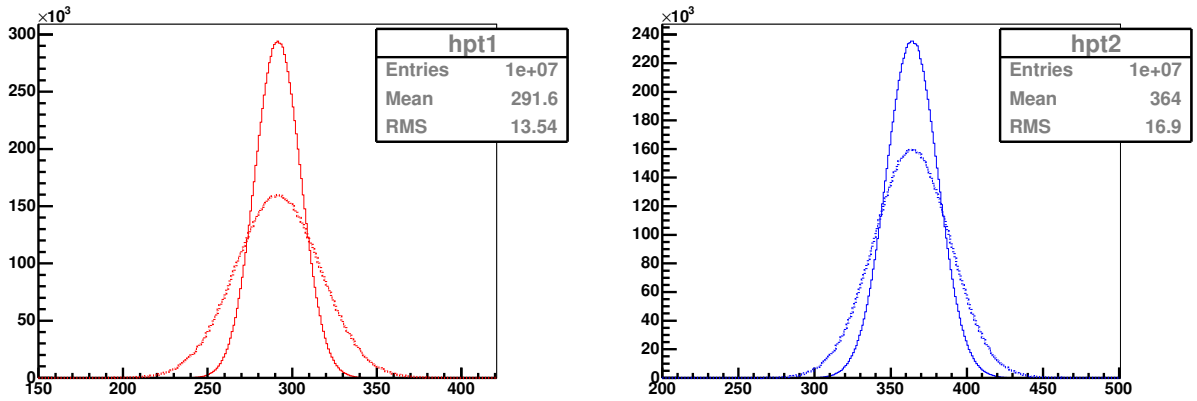

$(p_{T(1)})$ $(p_{T(2)})$

Figure 8.2: Toy model momenta, with the original p_T values (after gaussian smearing) and the much tighter peaks after the applied fit for the first two "particles" respectively

The kinematic fit is performed as shown in Equation 8.1, all p_T variables are distributed gaussian and a fixed error of 25 is used.

$$\chi^2 = \sum_{i=1}^{3} \frac{(p_T^{gauss}{}_i - p_T^{var}{}_i)^2}{\sigma^2_{p_T fix}} + f_x^2 + f_y^2 \tag{8.1}$$

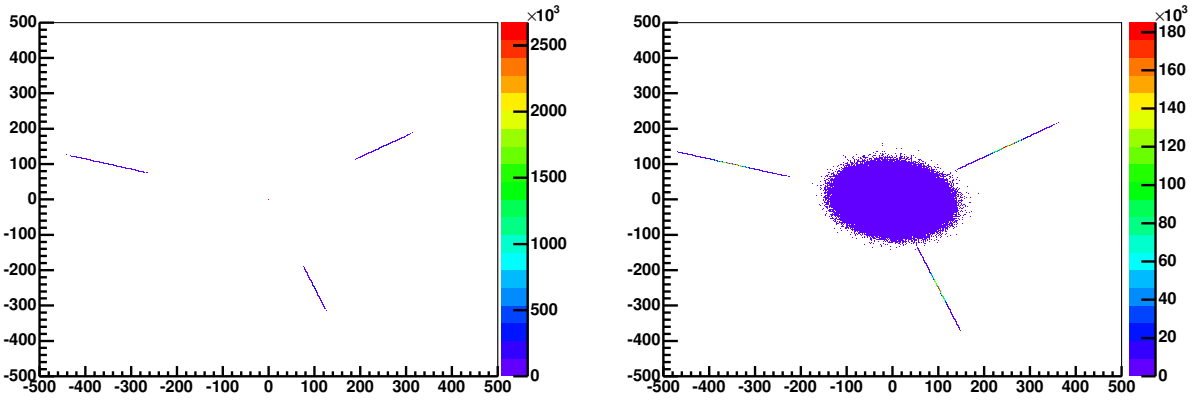

$(AFTER)$ $(BEFORE)$

Figure 8.3: Shown is the the momentum distribution in the x-y plane, as well as the vector sum of the x and y values in the middle of the two plots

The two additional terms are used to force the balancing of the momentum in the x-y plane as well as to assure reasonable values of the momentum.

$$f_x = \sum_{i=1}^{3} {p_T^{var}}_i \cdot cos(\phi_i) \tag{8.2}$$

$$f_y = \sum_{i=1}^{3} {p_T^{var}}_i \cdot sin(\phi_i) \tag{8.3}$$

As Figures 8.2 and 8.3 show, the fit works very well. The smeared ("measured") momenta are changed in order to minimize the χ^2 and this is done by forcing them to balance again in the x-y plane. The distributions narrow in Figure 8.2, and the wide distribution of the transverse vector sum in Figure 8.3 contracts to a single point.

This toy model shows that the kinematic fit works and can improve the measurement of the muon in the $\mu\mu\gamma$ analysis .

8.1.2 Kinematic Fit Concept for the Analysis

This kinematic fit exploits the fact that the $\mu\mu\gamma$ topology does not have missing transverse energy and therefore the event should always be balanced in the x-y plane.

The algorithm is a simple χ^2-fit [60] with an additional penalty term.

$$\chi^2 = \sum_{\mu} \frac{(\frac{1}{{p_T^{meas}}_i} - \frac{1}{{p_T^{var}}_i})^2}{\sigma^2_{\frac{1}{{p_T}_i}}} + \frac{({p_T^{meas}}_\gamma - {p_T^{var}}_\gamma)^2}{\sigma^2_{{p_T}_\gamma}} + \frac{1}{5\text{GeV}^2} \cdot f_x^2 + \frac{1}{5\text{GeV}^2} \cdot f_y^2 + 5000 \cdot f_{neg} \tag{8.4}$$

The last term was added in the analysis since in this case the problem of negative transverse momenta did occur.

$$f_{neg} = \sum_{i=1}^{3} \left(arctan(\frac{Cut(i)}{GeV} - \frac{{p_T^{var}}_i}{GeV}) + \frac{\pi}{2} \right) \tag{8.5}$$

The parameter Cut(i) equals 10 GeV for the two muons and 3 GeV for the reconstructed photon. It ensures reasonable positive values for the transverse momenta of the included particles after the fit. The factors in front of the penalty terms are necessary for the fit, since otherwise the fit does not converge. They have been determined through try and error.

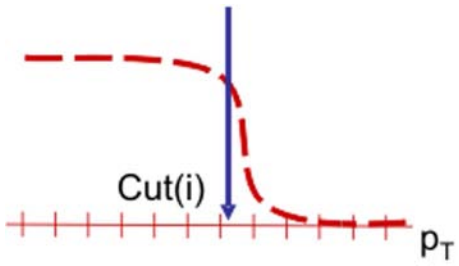

Figure 8.4: Sketch of the step function. This function assures positive and reasonably large values of the fitted transverse momenta

Uncertainties Of The Muon
The p_T measurement for muons with the DØ detector is performed inside the central tracker, since this delivers the better resolution. The p_T resolution for the central tracker is

$$\frac{\Delta p_T}{{p_T}^2} = 0.002\ GeV^{-1}$$

and is used as the estimate for the resolution of this fit.

Uncertainties Of The Photon

$$\left(\frac{\Delta E}{E}\right)^2 = C^2 + \frac{S^2}{E} + \frac{N^2}{E^2} \tag{8.6}$$

With C=0.04, S=0.2 GeV$^1/2$, N=0.29 GeV.

- C represents a systematic term including calibration errors
- S accounts for statistical uncertainties due to sampling fluctuations
- N is the noise term, describing the residual radioactivity of the uranium

8.1.3 Resulting Improvements

This kinematic fit approach leads to a major improvement in the shape of the reconstructed invariant μ^* mass peak as is shown in Fig.8.5. The fit is applied event by event.

The improvement in the invariant mass distribution means that the final cut can indeed be applied at higher values in the fitted invariant mass distribution than it would have been performed in the unchanged distribution without loosing signal efficiency.

The kinematic fit is very stable even when changing the assumed transverse momentum resolution drastically (factors up to 5).

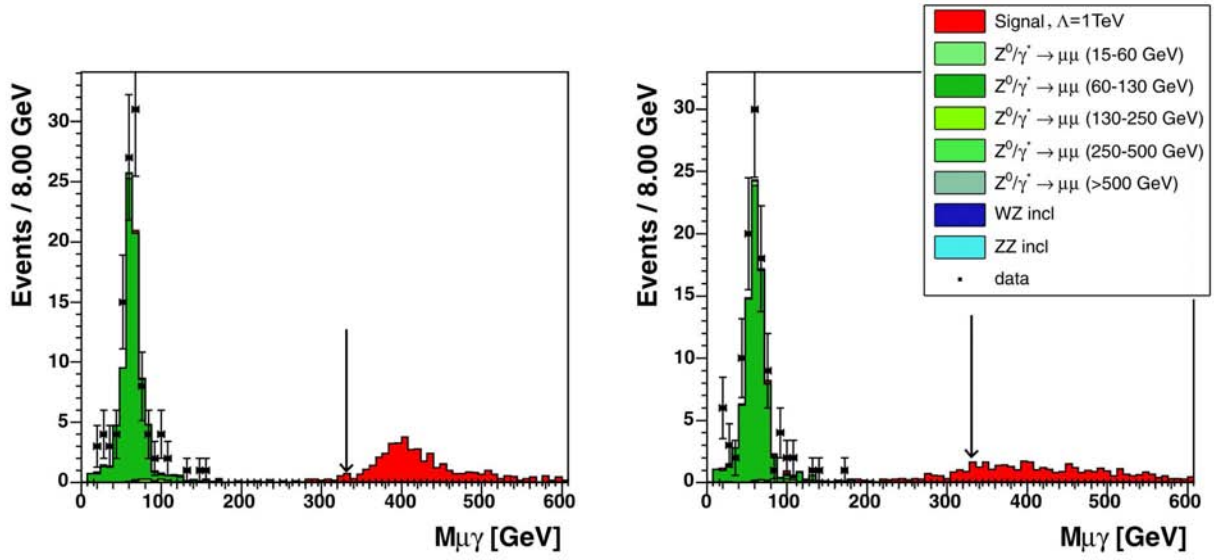

Figure 8.5: Invariant mass spectrum of $\mu\gamma$ (Left) with fit; (Right) without fit (both after dimuon+photon selections (chapt. 7).The included signal represents an excited muon mass of 400 GeV

This makes the results very robust against resolution effects and their parametrization. The results given below are based on the limits obtained from the fitted muon momenta in order to profit from the small improvement in the signal efficiency (typically 0.5-1 percentage points).

To perform the fit TMinuit [60] is used, based on the Minuit Fortran code. This package was used to realize the kinematic fit algorithm and it is linked directly to the analysis routines.

8.2 Efficiency Corrections

In general efficiency corrections are understood to correct for discrepancies between the genuine and the simulated data. If in both cases the acceptances and efficiencies would behave alike, no correction would be needed.

8.2.1 DiMuon Trigger Efficiency Correction

General Approach

Since the Monte Carlo simulation does not include a trigger simulation, the Monte Carlo Data has to be corrected for the genuine trigger efficiency. For the determination of the trigger efficiency, the TriggerEfficiency class [62] is used, based on studies from the DØ Top Group. All used Monte Carlo events are being weighed according to the kinematic event properties, like muon energy and angular distribution in order to describe the DiMuon trigger efficiency. This class calculates weight factors, event by event, to model the DiMuon trigger efficiency, on average 88.43 ± 0.07, based on the L1, L2 and L3 "turn on" curves.

Typically there are a few ways to determine the trigger efficiency including simulating trigger requirements in the MC. In this package, the di-object trigger efficiencies are calculated combining the single-object turn on curves.

The total event probability $P(L_1, L_2, L_3)$ (L_i representing the trigger levels) is given as the product of the probabilities to satisfy the requirement at each trigger level:

$$P(L_1, L_2, L_3) = P(L_1) \cdot P(L_2|L_1) \cdot P(L_3|L_1, L_2). \tag{8.7}$$

The conditional probability describes the probability for an event to pass the criteria under the condition that it has passed the earlier trigger criteria as well.

The total probability of an event to satisfy a set of trigger requirements is calculated under the assumption, that the single object probability is unaffected by the presence of other objects in the event.

Using this assumption the contribution from different types of objects to the total probability would factorize as follows:

$$P(Obj_1, Obj_2) = P(Obj_1) \cdot P(Obj_2) \tag{8.8}$$

With this assumption the probability (P) for one object to fulfill a certain trigger requirement out of a total of N objects in a single event can be written as :

$$P = 1 - \prod_{i=1}(1 - P_i) \tag{8.9}$$

The DiMuon Parametrization

Figures 8.6(A)(B) show the turn on curves for the L1 muon trigger (`mu1ptxatxx` (complete muon region, single muon scintillator trigger, without p_T requirement) as well as the eta dependency for the L2 (`MUON(1,med)` (one medium muon triggered by the L2 trigger)) requirement. For the correct application of the DiMuon trigger efficiency one has to keep in mind, that the L2 parametrization is only valid for events containing at least one medium muon with $p_T > 15\ GeV$.

The efficiencies are measured for every trigger list v9, v11, v12 and for v13 as well as for every trigger level (L1-L3).

The total trigger efficiency is given as:

$$P(L_1, L_2, L_3) = (P_{L_1} \cdot P_{L_1}) \ \cdot \ (1 - (1 - P_{L_2})^2) \cdot 1 \tag{8.10}$$

The different terms each represent one of the trigger level probabilities:

$$(P_{L_1} \cdot P_{L_1}) \ \hat{=} \ \text{prob. for L1 to find two } \mu \text{ with prob } P_{L_1} \tag{8.11}$$

$$(1 - (1 - P_{L_2})^2) \ \hat{=} \ \text{cond. prob. @ L2 to find 1 of 2 } \mu \text{ with } P_{L_2}(aft.L1) \tag{8.12}$$

$$1 \ \hat{=} \ \text{cond. prob. @ L3 to find 2 muons } (aftL2) \tag{8.13}$$

The P_{L_i} are given by Equation 8.14 and the the L3 requirement is 100% efficient.

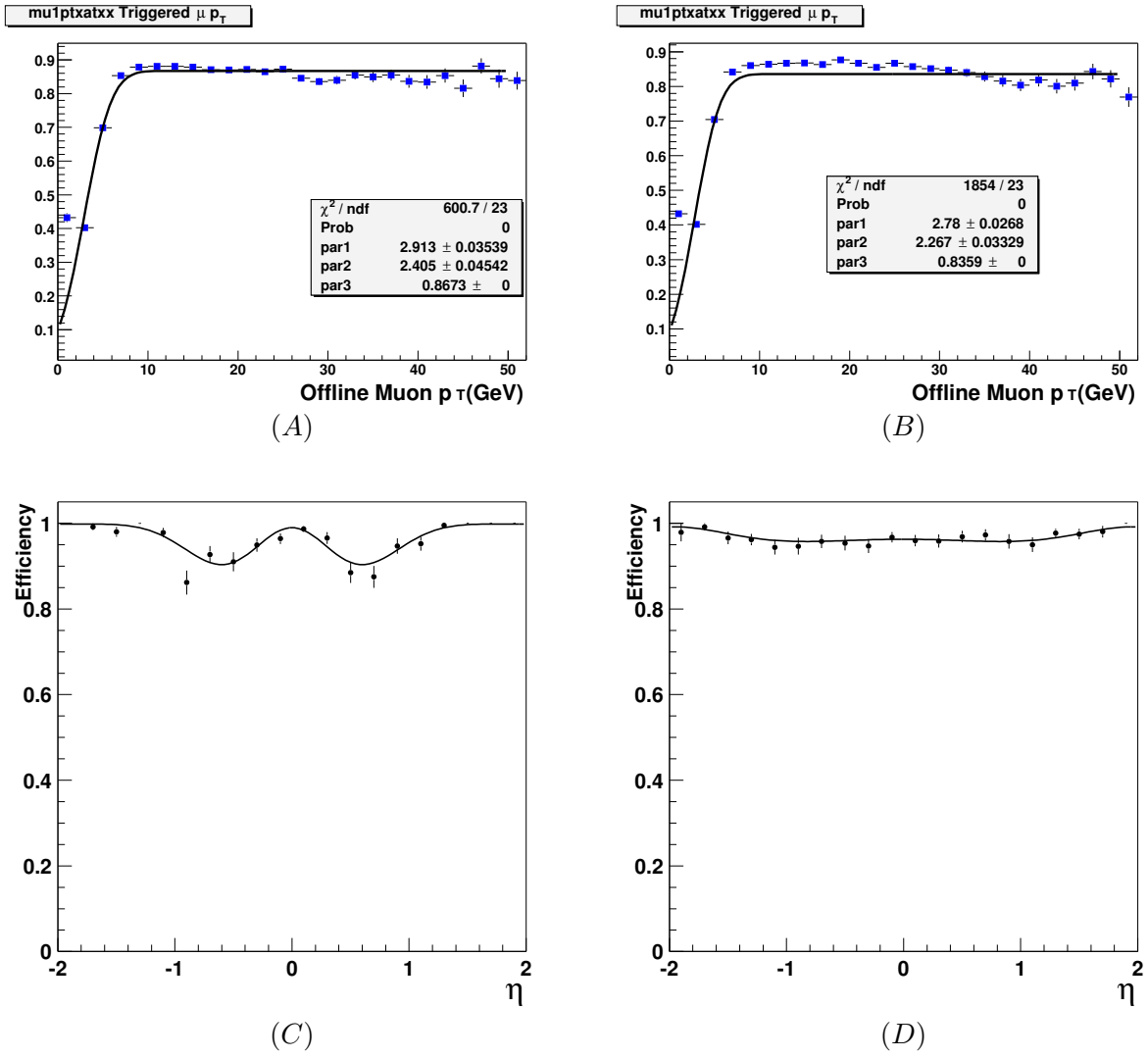

Figure 8.6: Level 1 Trigger turn on curves for the trigger `mu1ptatxx` as measured for different trigger lists v9-v11 (A) and v12 (B) [63]. (C), (D) show parameterizations of the L1 and L2 dependence for trigger list v12. (more details in [63])

The η dependency can be parameterized by [62]

$$f(\eta) = A_3 + A_0 \cdot \exp\left(-A1 \cdot (\eta^2 - A_2^2)\right) \cdot \sin\left(\eta^2 - A_2^2\right) \tag{8.14}$$

The turn-on-function has two separate parametrization for L1 requirement `mu1ptatxx` and for the L2 requirement (`MUON(1,med)`), given in Table 8.1.

trigger level	A_0	A_1	A_2	A_3
L1(`mu1ptatxx`)	-0.8 ± 0.2	2.8 ± 0.5	0.1 ± 0.1	0.99 ± 0.01
L2(`MUON(1,med)`)	0 ± 0	8.7 ± 7.0	1.779 ± 0.006	0.981 ± 0.007

Table 8.1: This table shows the parametrization results for the turn-on-function for L1 and L2 muon trigger efficiencies for data, given in 8.14. For details see DØ-Note 4512 [62].

8.2.2 Muon Efficiencies

The Monte Carlo, even though it is meant to simulate the detector completely, usually suffers from slightly different efficiencies then they are in the genuine data. In the case of this analysis most of the efficiencies used are taken from the analysis [49].

The efficiency differences are corrected by the factors summarized in Tab. 8.2. In the following the method

Effect	Correction Factor	σ
Muon trackmatching	1.027	$\pm$ 0.027
Muon isolation	0.989	$\pm$ 0.011
Muon reconstruction	0.973	$\pm$ 0.027
Muon Medium Eff.	1.016	$\pm$ 0.016

Table 8.2: Efficiency corrections [49] due to data MC differences, and their systematic errors.

of determining the correction factors will shortly be presented together with the results for the different muon efficiencies based on the analysis [49].

The method used is the commonly used "tag and probe" method. Typically for this method is the selection of data based on a set of tight selection cuts under the constraint that these cuts have to be independent of the cut for which the efficiency is calculated.

This selected sample is then probed for the requirement which is evaluated. The efficiency is then calculated as the ratio

$$\epsilon = \frac{probed}{tagged}.$$

Usually resonances like the Z-boson are used for these method to ensure a clean signature and to have a controllable background.

The efficiencies are determined separately for Monte Carlo and data and then the correction is calculated.

Reconstruction Efficiency

The efficiency for muon reconstruction describes the probability for a muon being detected as a "loose muon" by the detector muon system. A loose one must at least fulfill two of the following conditions, while a muon fulfilling all conditions would be a "medium muon".

- at least one A layer scintillator hit
  at least two A layer wire chamber hits
- at least one BC layer scintillator hit
- at least two BC layer wire chamber hits

The muon reconstruction efficiency is calculated using the Z-resonance.

The Z sample used is selected requiring at least one well measured medium, isolated and track matched muon (muon with a central track) with at least 15 GeV transverse momentum. This event mustn't contain more than one jet, and in addition anti cosmic cuts are applied.

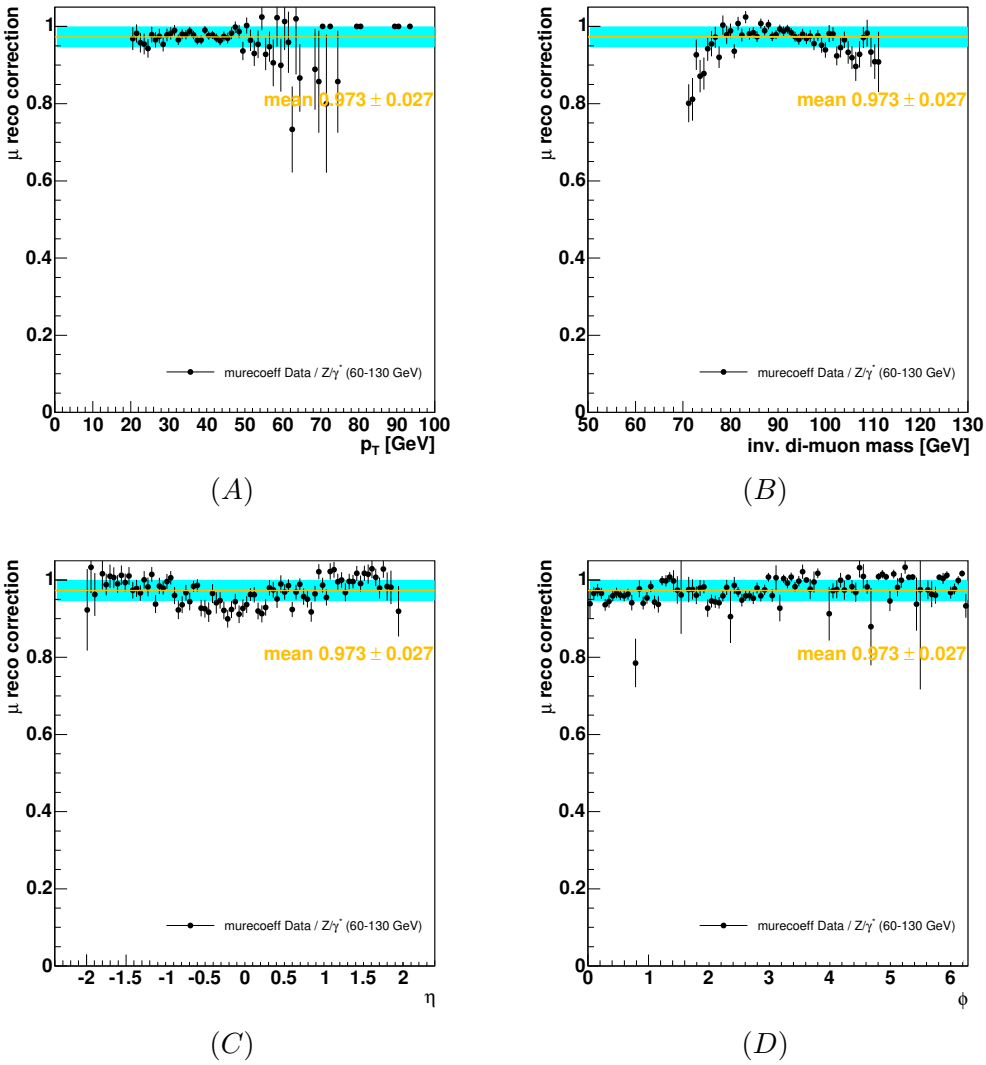

Figure 8.7: Muon reconstruction correction factor: Ratio of data and Monte Carlo muon reconstruction efficiency versus (A) p_T, (B) invariant DiMuon mass of tagged muon and the track of the muon candidate, (C) η and (D) ϕ [49]

To perform this evaluation the event also has to contain at least one well measured track opposite in ϕ to the first muon with a transverse momentum above 20 GeV. This track has to be outside the bottom hole of the DØ detector and the assigned charge has to be opposite to the charge of the first muon. Muon and track together have to match the Z mass within $\pm$ 20 GeV.

These requirements define the tagging sample, which is now probed.

There are two methods to probe for the second muon; first one can check if there is a matching loose muon within a distance of 0.5 around the track and secondly one could check if there is a loose muon matched to the track by the DØ reconstruction algorithms.

The first method delivers the reconstruction efficiency, the second one is the product of reconstruction and track matching efficiency.

This determination was based on pass 2 data samples and used the TopAnalyze version “Ipanema” (Details [49]), as well as a pass 2 Monte Carlo containing 60-130 GeV Z/γ^* events.

	Data	Monte Carlo
reco. efficiency	0.9132 ± 0.0021	0.9386 ± 0.0012
reco. $\times$ track match eff.	0.9130 ± 0.0021	0.9384 ± 0.0012

Table 8.3: Muon reconstruction efficiency in data and in the Monte Carlo simulation [49]

As shown in Table 8.3, the reconstruction efficiency is given as 0.9132 ± 0.0021 and agrees with the reconstruction times trackmatching efficiciency under the assumption of a track matching efficiency of 99.8%. This is consistent with the determination of this quantity in section 8.2.2.

A constant correction factor of 0.973 ± 0.027 is applied, calculated from the values in 8.3 and based on the distributions in Figure 8.7.

The distributions, in all four shown variables, are reasonably flat and therefore no reason is given to make a more complex approach for the correction factor.

Muon Track Finding and Matching Efficiency

Since the muon resolution is quite poor considering only the muon system itself (sec. 4.2.4), muon pt is usually measured with the tracking system requiring the identification and matching of one track belonging most likely to the muon.

In order to determine the track finding and matching efficiency, at least one well measured, medium, isolated muon with matched central track and transverse momentum above 30 GeV is required, while the "probe" muon has to have at least 20 GeV measured in the local muon system, and a separation of 2.8 in ϕ from the "tag" muon.

For this evaluation the Z-mass region is used, requiring the mass of the two objects to be in a range of 30 GeV around the nominal Z-mass.

The evaluation is based in the pass 2 2MU skim and a Z/γ^* Monte Carlo, as mentioned above, both processed with TopAnalyze "Ipanema" [58].

	Data	Monte Carlo
track efficiency	0.998 ± 0.001	0.972 ± 0.001

Table 8.4: Track finding and matching efficiency in data and in the Monte Carlo simulation [49]

The track matching and finding efficiencies in data and Monte Carlo have the same shape which leaves the correction factor to be flatly distributed, as shown in Figure 8.8.

Based on this flat distribution a constant correction factor of 1.027 ± 0.027 is applied per event and muon.

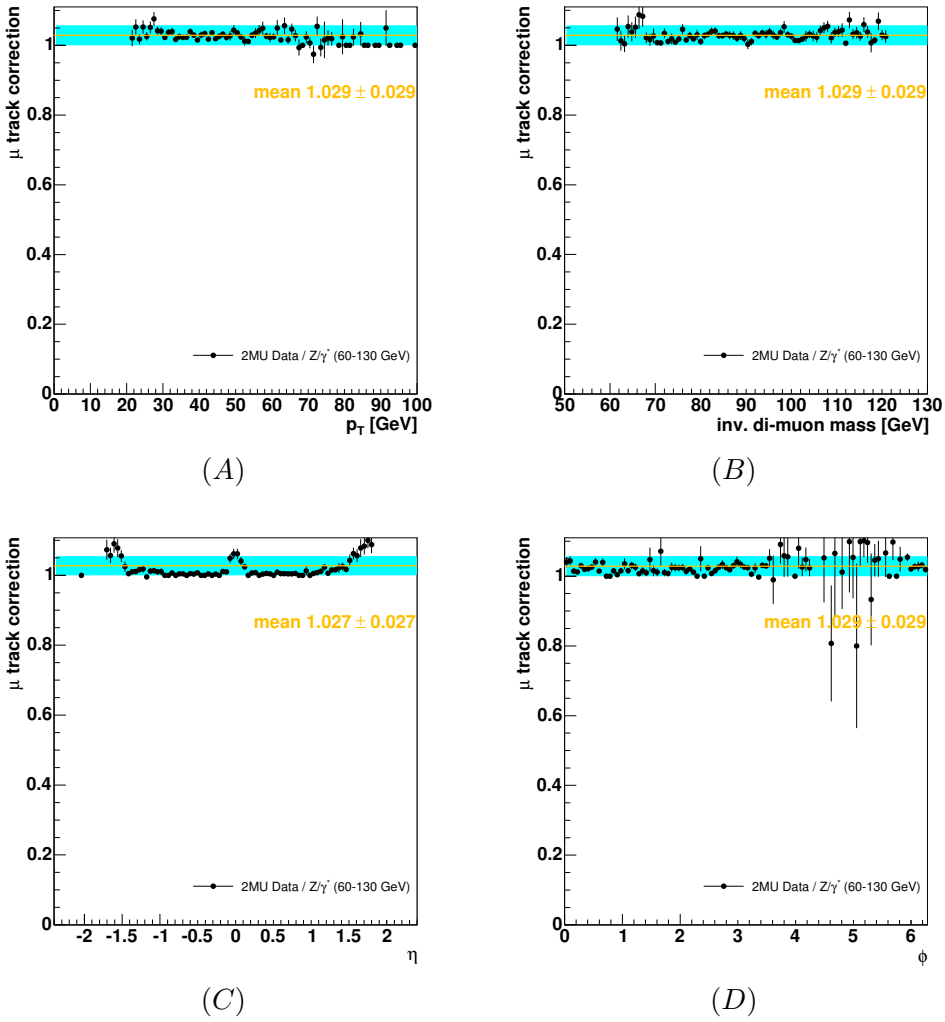

Figure 8.8: Muon track finding & matching correction factor: Ratio of data and Monte Carlo muon "track matching" efficiency versus (A) p_T, (B) invariant DiMuon mass, (C) η and (D) ϕ [49]

Isolation Efficiency

The muon isolation efficiency is evaluated similarly to the prior described track matching and finding efficiency, and the determination is based on the same data and Monte Carlo samples.

Isolation for the muons is meant as described in section 7.2.1 and describes the energy deposition around the evaluated muon.

The isolation efficiency is calculated based on events containing the tag muon with isolation requirement and a matched track and a second muon with track match (probe muon).

The invariant mass of the muons should again be in the range $|mass(\mu\mu) - 91\ GeV| < 30\ GeV$.

The transverse momentum of the tag muon and the probe muon is required to be above 8 and 15 GeV, respectively.

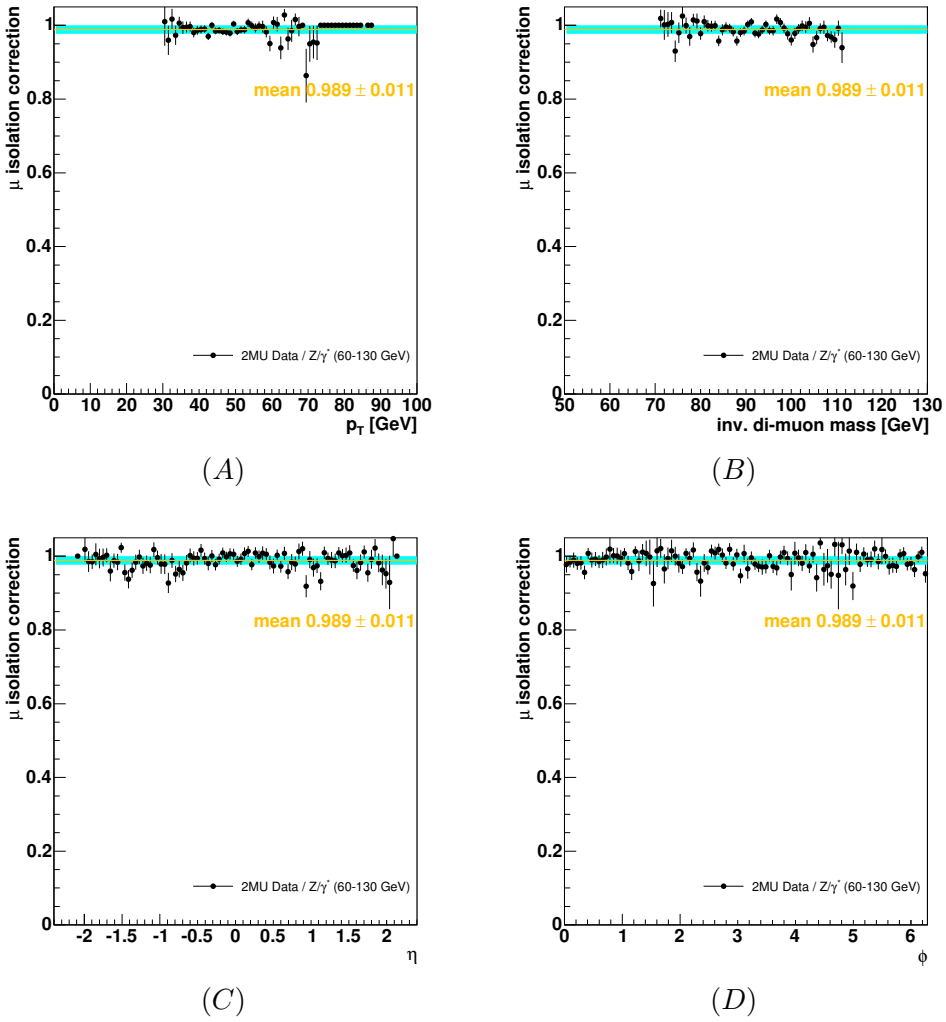

Figure 8.9: Muon isolation correction factor: Ratio of data and Monte Carlo Muon isolation efficiency versus (A) p_T, (B)invariant DiMuon mass, (C) η and (D) ϕ [49]

	Data	Monte Carlo
isolation efficiency	0.944 ± 0.002	0.956 ± 0.001

Table 8.5: Muon isolation efficiency in data and in the Monte Carlo simulation [49]

The efficiency correction calculated has reasonably flat distribution as is displayed in Figures 8.9 (A)-(D), and therefore a constant correction factor of 0.989 ± 0.011 is applied to all Monte Carlos samples.

Medium Efficiency

The "medium" efficiency is determined by tagging loose muons and probing them for medium quality with the criteria explained before and at [73]. Again the "2MU" skim data is used in combination with a Z/γ^* Monte Carlo. As described before, the Z resonance is used by asking for two well measured, isolated and

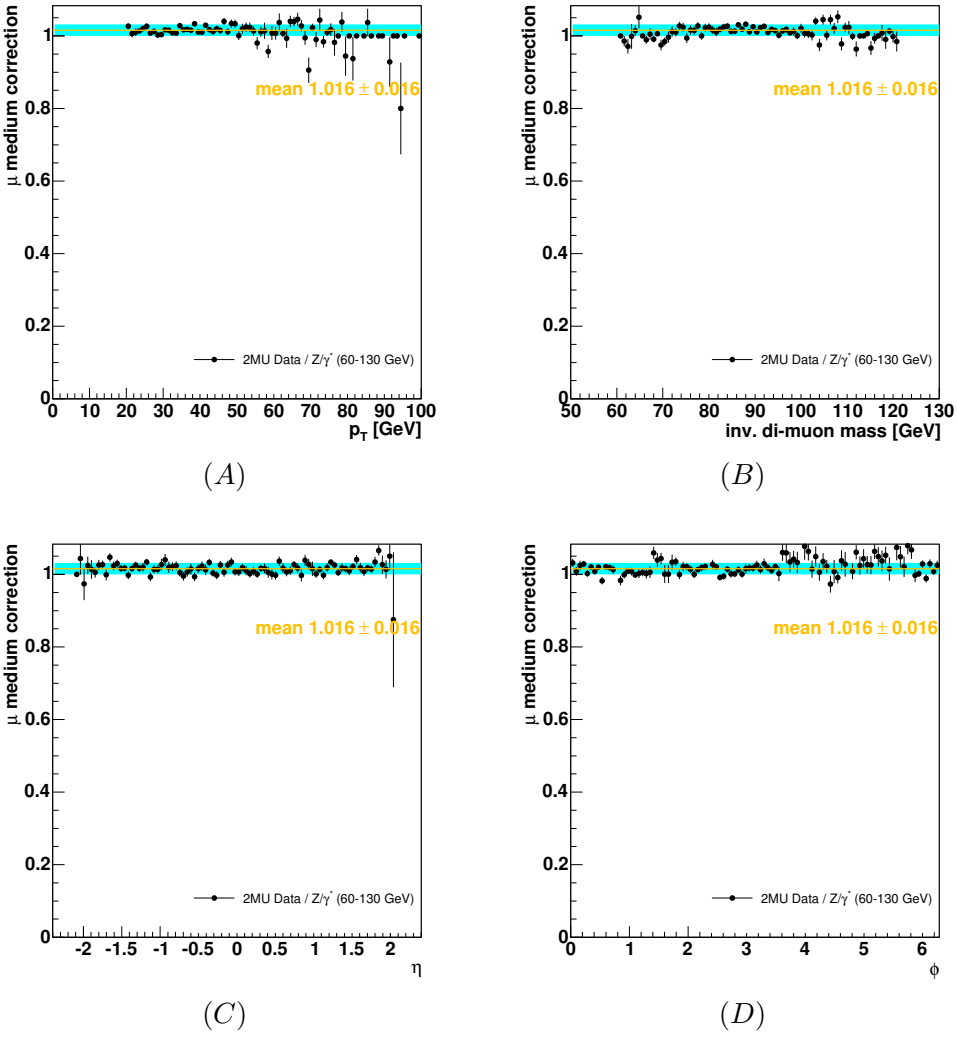

Figure 8.10: Muon medium correction factor: Ratio of data and Monte Carlo Muon medium efficiency versus (A) p_T (B)invariant DiMuon mass (C) η and (D) ϕ [49]

	Data	Monte Carlo
medium efficiency	0.971 ± 0.002	0.956 ± 0.001

Table 8.6: Medium efficiency in data and in the Monte Carlo simulation [49]

track matched muons with an invariant mass 20 GeV around the Z boson mass. In addition both muons should have a azimuthal distance of at least 2.8 in ϕ. The medium efficiency is flat distributed in ϕ, η, p_T and the invariant DiMuon mass. Similar to the previously discussed efficiencies a constant correction factor of 1.016 ± 0.016 can be applied to all Monte Carlo samples.

8.2.3 Further Corrections

The Monte Carlo has a few other deficiencies which are corrected by routines already implemented in the used TopAnalyze [58] "Ipanema" analysis package. Typically examples are the EM energy, jet energy scale corrections and muon resolution smearing.

The energy scale of the calorimeter for example the jet energy scale is necessary since the electronic response of the detector has to be interpreted as an energy measurement. In addition a jet showers in the calorimeter but only a certain amount of the total energy can actually be measured due to the inert absorbing material which is not instrumented.

The calorimeter therefore is calibrated, which means that the hardware signal is multiplied by a certain factor, the Energy scale. This energy then reflects the true physical value of the energy deposit.

These detector simulation is often insufficient to reproduce the exact data distributions therefore correction factors are applied. This leads to a smearing for the muon p_T according to [42, 50]:

$$\frac{1}{p_T'} = \frac{1}{\alpha \cdot p_T} + Gauss(0, \sigma), \tag{8.15}$$

with $\alpha = 0.991 \pm 0.003$ and $\sigma = 0.0025 \pm 0.0002\ GeV^{-1}$.

8.2.4 Photons from Misidentified Jets

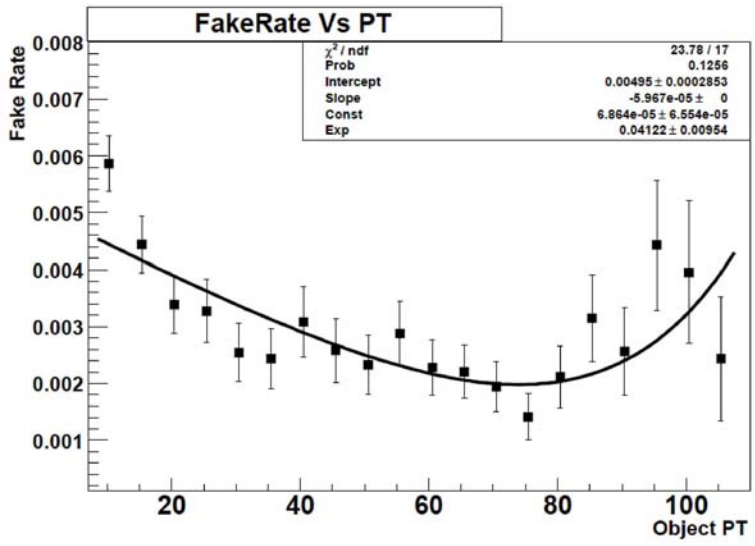

Figure 8.11: The plot shows the rate of jets being misidentified photons against the p_T of the jet [76]

Since not a clean Z data sample is used but a DiMuon skim this analysis uses the following description only as an estimation for an additional systematic uncertainty. The estimated events are in no way added to the background samples which is a conservative approach.

The description of jets faking a photon is based on [76] and uses Z+jets data to estimate the background in their analysis. The background due to Z+jets processes is estimated by measuring a rate at which a jet is reconstructed as a photon from data. The exact procedure for this is described at [77], but the basic technique is to use events where a jet triggered the event and a high quality jet is reconstructed and matched to the

trigger object. All further jets and any electromagnetic (EM) objects which pass photon id requirements are counted.

In the following a really short overview is given, to at least shed some light on the derivation of this "fake rate". This estimation was performed on the Common Sample Group QCD skim, which required jet and minimum bias triggers.

For the estimation of the fake rate on selected events that were triggered by one of the following two jet triggers:

- `Jet25_TT_NG`:Two Level 1 calorimeter towers above 5 GeV, as well as a jet reconstructed at Level 3 with minimum E_T of 25 GeV
- `Jet45_TT`: Two Level 1 calorimeter towers above 5 GeV, as well as a jet reconstructed at Level 3 with minimum E_T of 45 GeV

In order to avoid any bias from the trigger requirements the lead reconstructed jet was required to match up with the triggered jet, the Level 1 calorimeter towers were required to be matched in η and ϕ within 0.3 while the Level 3 jet transverse energy was required to be within dR $<$ 0.5 of the lead reconstructed jet.

In a order to assure a good quality lead jet additional quality criteria were applied to the lead jet which can be found at [77]. After the trigger bias is effectively avoided by this measures, the other objects are the data sample on which now the fake rate is estimated. Good jets are counted requiring certain criteria, like the EM-fraction to be in between 0.5 and 0.9 and some other jet specific parameters.

In the End the fake rate then is calculated by dividing the number of unbiased good electromagnetic objects in these events by the total number of unbiased objects(including jets and electromagnetic objects). Unbiased here indicates that due to the matching of the lead jet to all the required trigger criteria the biases due to these requirements at the trigger level are taken into account.

This rate now gives the frequency with which objects passing photon identification cuts will be produced in QCD events, such as underlying processes in the Z/γ^* samples and the DiMuon data.

This situation is slightly complicated by real final state photons that are genuinely produced at higher E_T by in this QCD processes. This fraction is excluded from the final estimation of the fake rate by using an estimation from Run I

$$P = 1 - e^{a+b\times E_T}.$$

As one can see in Figure 8.11 the fake rate is actually increasing with E_T.

The ratio of EM objects to (jets plus EM) objects is shown as a function of ET in Figure 8.11 taken from [76]. Based on their experience the low ET region is identified as being dominated by jets faking a photon, while the high transverse Energy region is dominated by initial state radiation (direct photon production). The misidentification rate is taken from the slope and intercept of the fit in Figure 8.11 and further used to estimate the uncertainty due to "fake" photons :

$$f_{QCD} = (4.95 \pm 0.29) \cdot 10^{-3} - (5.91 \pm 1.15) \cdot 10^{-5} E_T \; [GeV] \tag{8.16}$$

In case of this analysis the number of photons being misidentified jets is based on this result by counting the jets with at least 8 GeV, a distance to th emuons of δR¿0.7 and in the photon range of $|\eta| < 1.1$ in the data for every bin, (binning as shown in Figure 8.11) and then reweighing the bin entry according to the fake rate estimation. For the estimation at the final selection the events are required to pass signal point specific cuts in invariant mass of jet and muon.

The number of photons being misidentified jets is negligible in the final selection especially at high signal masses.

The number of "fake" photons is used as an additional systematic error on the background after the gamma selection. As a more conservative approach this error is only added quadratically to the existing error, without adding the number of events onto the background expectation.

Number of possibly misidentified jets for the gamma selection sample : 44.63

Number of possibly misidentified jets for the final selection sample : $\mathcal{O}(10^{-5})$

The trouble with this estimation is that it might have double counting in it, since the original estimation was performed on genuine Z+jets data and not on a sample including other jet processes which are taken into account as well, but since this estimation is only added as an error into the calculation, it should be sufficient. At least this is only problematic for the last but final selection since in the final selection the numbers are negligible in comparison.

8.2.5 Photon Efficiency

It has been observed that the description of photons in the Monte Carlo is not sufficiently precise. Therefore it is a usual procedure to compensate for different identification efficiencies between MC and Data, as for this search the results from an existing DØAnalysis of $Z\gamma$ events [76] are used, which calculated the overall photon efficiency to be

$$\varepsilon_{\gamma}^{data} = 0.82 \pm 0.03 \quad .$$

Performing an efficiency calculation based on this analysis leads to a photon efficiency of

$$\varepsilon_{\gamma}^{MC} = 0.85 \pm 0.03$$

for the used MC simulation. Therefore it is compensated for this difference by removing randomly about 4% (correction factor would be ~ 0.96) of the selected γ events from the MC during the analysis.

The photon efficiency is estimated using the signal samples, in order to have sufficient statistics. The number of genuine photons on generator level is counted, and then the number of photons passing the photon selection cuts is counted.

The uncertainty of the correction ends up to be 3% which is used as and additional systematic uncertainty for the event selections including photon requirements. The uncertainty represents the maximum deviation from the mean value for the several signal samples.

8.3 Systematic Uncertainties

The main systematic errors are due to different efficiencies in data and Monte Carlo events and all of them have been included in the final calculations The following effects are taken into account:

- the uncertainties on the trigger efficiencies varying for the different Monte Carlo samples; $\approx$ 3%-6%, depending on the MC sample
- all the uncertainties arising from the correction factors in Table 8.2 which are applied due to imperfections in the detector simulation for the MC samples:$\approx 1\% - 3\%$

- an estimated uncertainty on cross section (e.g. scale, pdf) of 10%
- the uncertainty due to the luminosity measurement : 6.5% ([30])
- the uncertainty on the correction for the photon efficiency of 3% (sec. 8.2.5)
- the uncertainty due to the estimated misidentified jets (44.64 events at photon selection) (sec. 8.2.4)

8.3.1 Efficiencies and Luminosity

The uncertainties for all detector related efficiency corrections discussed in section 8.2.1 and 8.2.2 as well as the photon efficiency uncertainty and the error on the luminosity are assumed to be statistically independent and therefore added quadratically leading to the overall uncertainty $\frac{d\varepsilon_{\text{ff}}}{\varepsilon_{\text{ff}}}$ as shown in Eqn. 8.17.

$$\begin{aligned}\left(\frac{d\varepsilon_{\text{ff}}}{\varepsilon_{\text{ff}}}\right)^2 = & \left[\frac{d\varepsilon_{trig}}{\varepsilon_{trig}}\right]^2 + \left[\frac{d\varepsilon_{lum}}{\varepsilon_{lum}}\right]^2 \\ & +2\cdot \left[\frac{d\varepsilon_{rec}}{\varepsilon_{rec}}\right]^2 +2\cdot \left[\frac{d\varepsilon_{med}}{\varepsilon_{med}}\right]^2 + 2\cdot \left[\frac{d\varepsilon_{trk}}{\varepsilon_{trk}}\right]^2 + 2\cdot \left[\frac{d\varepsilon_{iso}}{\varepsilon_{iso}}\right]^2 \\ & + \left[\frac{d\varepsilon_{pht}}{\varepsilon_{pht}}\right]^2 \quad \text{for selections including photons}\end{aligned} \tag{8.17}$$

The uncertainties are divided into uncertainties per event in case of the trigger efficiency uncertainty and the luminosity uncertainty and uncertainties per event and muon. Even though only one isolated muon is required the uncertainty is applied to both muons, since not requiring isolation for the "second" muon is at least uncertain to the degree of the isolation requirement.

The uncertainty on the photon efficiency is only added in case the selection stage required a photon to be present.

The Absolute Uncertainty The absolute systematic uncertainty is calculated by multiplying the relative one, given by Equation 8.17, with the event number derived from the analysis at the given stage of selection, including already the event weights and correction factors.

8.3.2 Misidentified Photons

Even though the uncertainty due to misidentified jets is not used in the final stage of the selection, it is added as an additional error at the gamma selection stage. In this case the error is quadratically added to the overall error as a conservative approach.

Chapter 9

Comparison of Data and Monte Carlo

In the following the event numbers and some plots are shown in comparison between the data and Monte Carlo samples.

After the initial preselection with the 2MUhighpt skim around 180,000 events are left (chapt. 7). For these events further selection cuts (sect. 7.2) have been applied during the analysis for both data and MC, including trigger requirements (data) and quality statements. Corrections for different behavior of MC and data were applied (Sect. 8.2). This lead to a sample of around 25,000 data events (Tab. 9.1/9.2).

At this stage data and SM Monte Carlo agree well (Fig.9.2-9.4).

9.1 Data and SM MC events

In the following the different stages of the selection are shown regarding the event numbers and the statistical and systematic errors. The DiMuon selection (sec. 7.2.1 as well as the photon selection (sec. 7.2.2) are the same for every used signal point. The resulting event numbers are shown in 9.1

The final cut on the other hand is dependent on the invariant mass of the excited muon given the special signal point (sec. 7.2.3). The event numbers are compared in Table 9.2

Uncertainties: The uncertainties include the systematic uncertainties as described in chapter 8, section 8.3.

The statistical error is based on the statistics of the original Monte Carlo, and then weighed according to the average event weight of the Monte Carlo sample in use. This assures the correct description of the statistical error as can be seen below.

Lets assume a Monte Carlo sample with 900 generated events, this would have a statistical error of 30 events. If one now applies a Monte Carlo weight according to luminosity and efficiency correction one might end up with a factor of e.g. 0.15. Computing the statistical error based on this reweighed sample (135 events) would give a wrong value.

The generator sample has 30 events as the statistical uncertainty according to the generator statistics. For the real error one has therefore to calculate the statistical error before applying the event weight which leads

in this case to $30 \cdot 0.15 = 4.5$, the correct value.

The correct procedure therefore is:

1. Use the generator statistic to calculate the statistical error
$$Err_{gen} = \sqrt{N_{gen}}$$
2. Use the generator events N_{gen} and the reweighed events N_w to calculate the average event weight
$$Ev_w = \frac{N_{gen}}{N_w}$$
3. Calculate the statistical error :
$$Err_w = Err_{gen} \cdot Ev_w$$

9.1.1 DiMuon and Photon Selection

Sel. →	#data dimu	#SM dimu	#data gamma	#SM gamma
MC		$\# \pm stat \pm syst$		$\# \pm stat \pm syst$
Z/γ^*	-	$24636.8 \pm 70.6 \pm 3703.8$	-	$82.11 \pm 3.84 \pm 12.6$
WZ	-	$14.9 \pm 0.6 \pm 2.1$	-	$0.15 \pm 0.06 \pm 0.02$
ZZ	-	$11.5 \pm 0.3 \pm 1.6$	-	$0.11 \pm 0.03 \pm 0.02$
$\sum$	24853	$24663.2 \pm 70.6 \pm 3707.5$	110	$82.37 \pm 3.84 \pm 12.60$ (82.37 ± 47.57)

Table 9.1: Data and SM-background events after the DiMuon and DiMuon+photon selection (with kinematic fit). The error due to faked photons (sec. 8.2.4) is at the end(value in parenthesis)

At these stages data and Monte Carlo agree well within their overall errors, which also can be seen in section 9.2 on some additional control plots. The Photon selection is not as well understood as the DiMuon selection, but shows still reasonable agreement.This arises from the need to introduce cuts in the photon selection from [76], without having had the proper time to completely examine these cuts.

In Figure 9.1 two plots are shown, especially interesting for the DiMuon and photon selection, representing the DiMuon mass distribution and the invariant mass of the two muons and the additional photon.

Both plots show good agreement between data and Monte Carlo, especially the prominent Z boson peak is clearly well described by the SM Monte Carlo processes.

The slight excess in the lower plot is a general feature arising after the photon selection. These plots only include statistical errors for the data, while the systematic errors on the SM background are not shown. When taking the systematic errors into account the agreement should be even better as one can see in the overall numbers in Table 9.1.

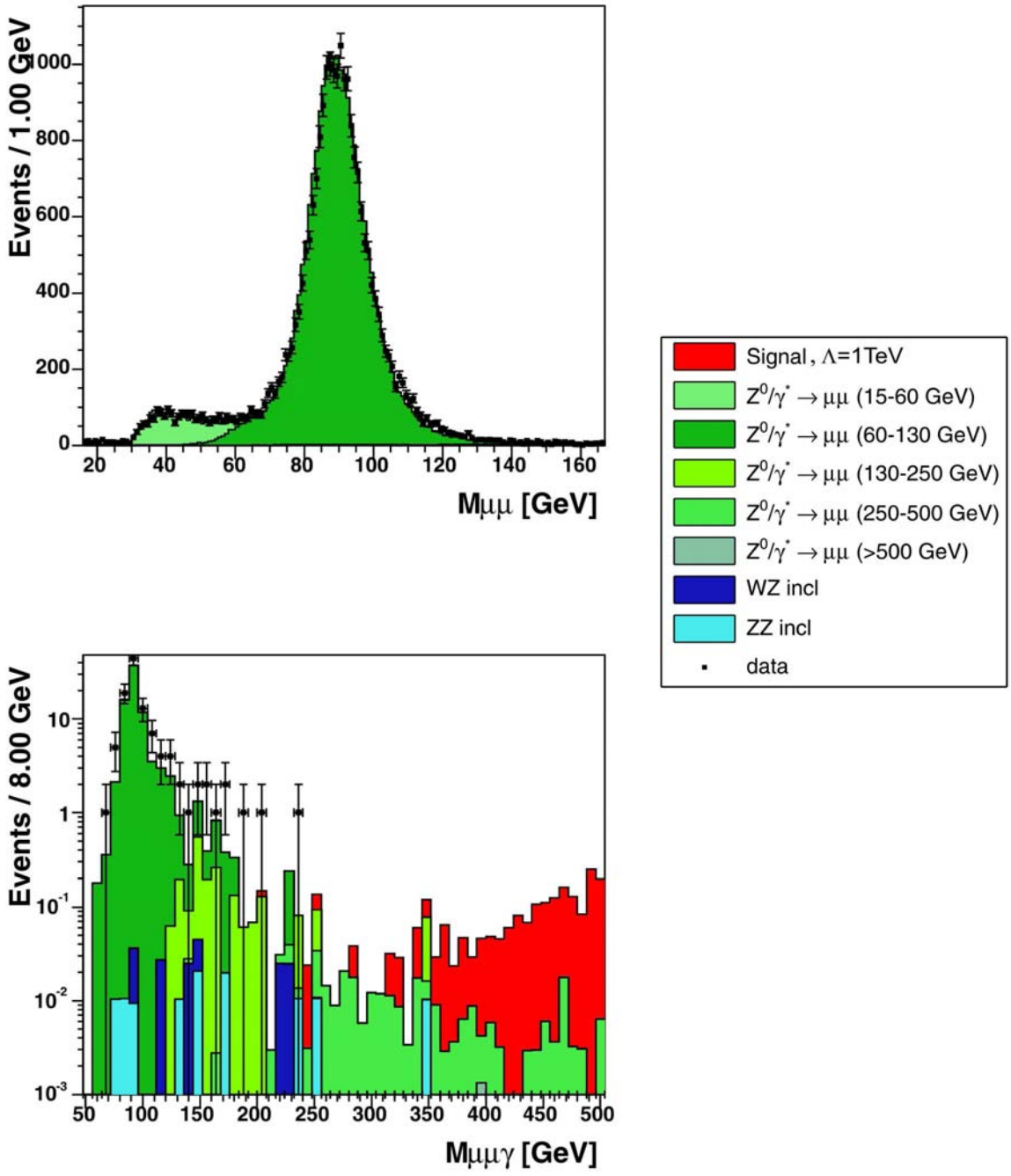

Figure 9.1: The upper plot shows the DiMuon mass distribution, reproducing the invariant mass of the Z-boson very well; The lower plot shows the invariant mass of the first two most energetic muons and the highest energetic photon

9.1.2 Final Selection

The cut flow for all signal points after the final selection is shown in Table 9.2. The first two points at aμ^* mass of 100 and 200 GeV are shown together, as well as all signal points above 500 GeV, since it was found

that the same cut should be applied for these points, respectively (7.2). The WZ and ZZ sample do not have sufficient statistics, therefore an upper limit for the event number is given according to to poisson statistics, given zero observed objects [54].

	Sel. →	#data final	#SM final		#data final	#SM final
Mass	MC		$\# \pm stat \pm syst$	**Mass**		$\# \pm stat \& syst$
100	Z/γ^*	-	$0.121 \pm 0.018 \pm 0.019$	**400**	-	$0.009 \pm 0.003 \pm 0.001$
&200	WZ	-	< 0.02		-	0.02
	ZZ	-	$0.012 \pm 0.010 \pm 0.002$		-	< 0.06
	$\sum$	0	$0.132 \pm 0.021 \pm 0.021$		0	$0.009 \pm 0.003 \pm 0.001$
300	Z/γ^*	-	$0.034 \pm 0.009 \pm 0.005$	$\geq$ **500**	-	0.002 ± 0.001
	WZ	-	< 0.02		-	< 0.02
	ZZ	-	< 0.06		-	< 0.06
	$\sum$	0	$0.034 \pm 0.009 \pm 0.005$		0	0.002 ± 0.001

Table 9.2: Data and SM-background events after the final cut on the invariant $\mu\gamma$-mass (with kinematic fit). The error due to faked photons is negligible at this stage

The Standard Model prediction from the Monte Carlo and the acquired data agree well Since the data can only have discrete events, this selection can very well have no entry on data if the statistic is not big enough.

The probability for such an event follows a poisson distribution

$$P(k) = \frac{\lambda^k}{k} \cdot e^{-\lambda} \tag{9.1}$$

In the case of the signal point with $m_{\mu^*} = 500\ GeV$ the probability would be

$$P(1) = \frac{0.002^1}{1} \cdot e^{-0.002} = 0.002$$

.

This means that having zero events has a probability of P(0)=0.998,which makes the zero events in the data quite plausible.

9.1.3 $Z/\gamma^* + \gamma \rightarrow \mu\mu + \gamma$

One of the main background processes for this search is $Z/\gamma^* + \gamma \rightarrow \mu\mu + \gamma$, this process is included in the $Z/\gamma^* \rightarrow \mu\mu$ samples, however there are concerns that the high-p_T regions may not as well simulated in `Pythia` as needed.

Since there are several difficulties concerning the comparison with a genuine $Z/\gamma^* + \gamma$ Baur-MC [68] the good agreement of data and MC (sect. 9.2) is taken as a sign that there should not be too much concern about the potential discrepancies.

Especially the invariant dimuon+gamma mass (Fig. 9.1) shows good agreement of data and MC and should be sensitive if there would be larger problems in the description of this channel.

9.2 Control Plots

In the following section a few control plots of the different kinematic properties are shown in order to display the agreement between data and Monte Carlo.

The plots in Fig. 9.2 - 9.4 show data and MC at all stages of the analysis, some with and some without the kinematic fit. Included are statistical uncertainties on the data, while the SM as well as the signal events are shown without their respective systematic errors. The Plots show the signal with correct cross section and branching ratio.

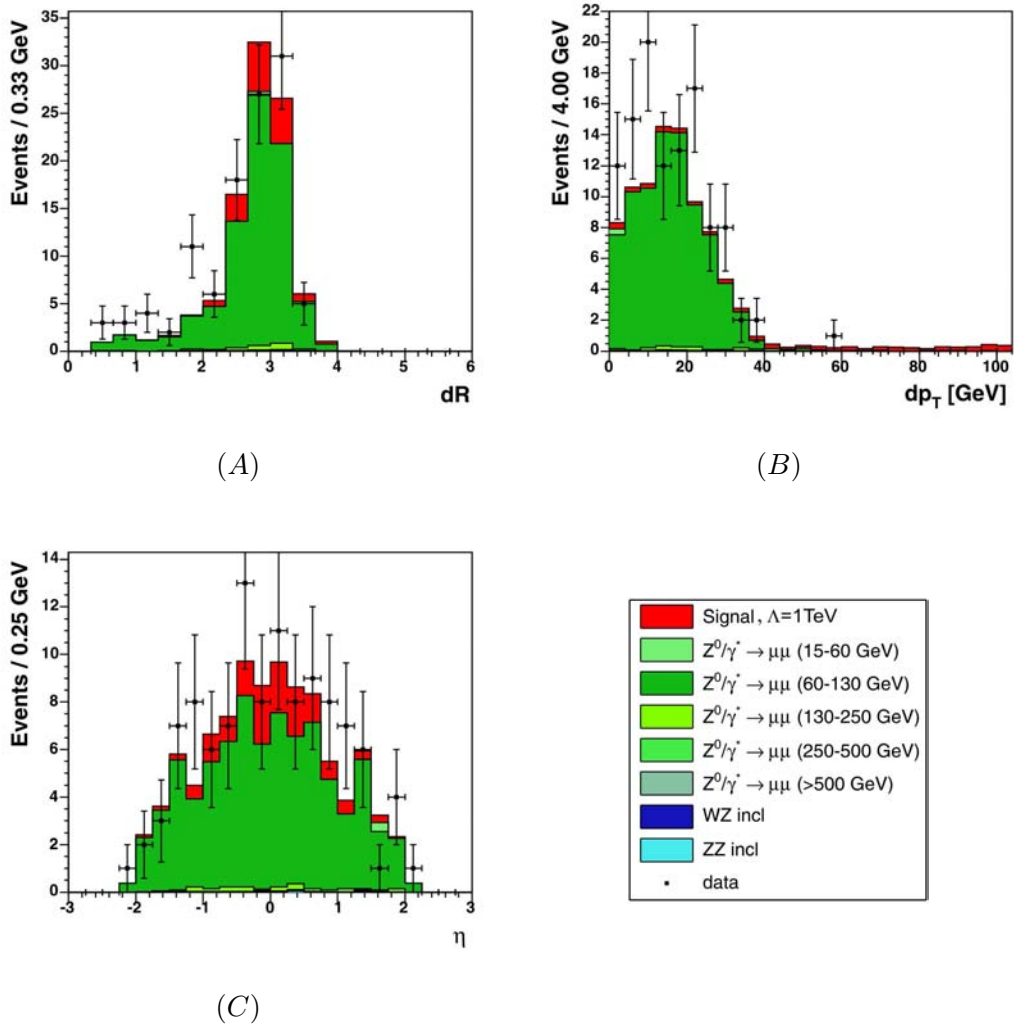

(A) (B)

(C)

Figure 9.2: (A) $dR = \sqrt{\phi^2 + \eta^2}$ of highest energetic muon and photon after the γ selection (with kinematic fit). (B) $dp_T = |p_T(\mu 1) - p_T(\mu 2)|$ values between the two highest energetic muons after the kinematic fit.((C) η distribution of highest energetic muon after the γ selection.

The Figures 9.2 (A) and (B) show the transverse momentum difference between two highest energetic muons as well as the distance dR between the two selected muons. Both distributions are shown after the kinematic fit and show good agreement between data and Monte Carlo.

The sminor excess in (B) is small enough to be covered by the systematic uncertainties. The plot in (C) represents the pseudo rapidity of the highest energetic muon, which is well describe in data and Monte Carlo. The plots in Figure 9.3 (above) show the DiMuon mass and invariant mass of photon and muon respectively.

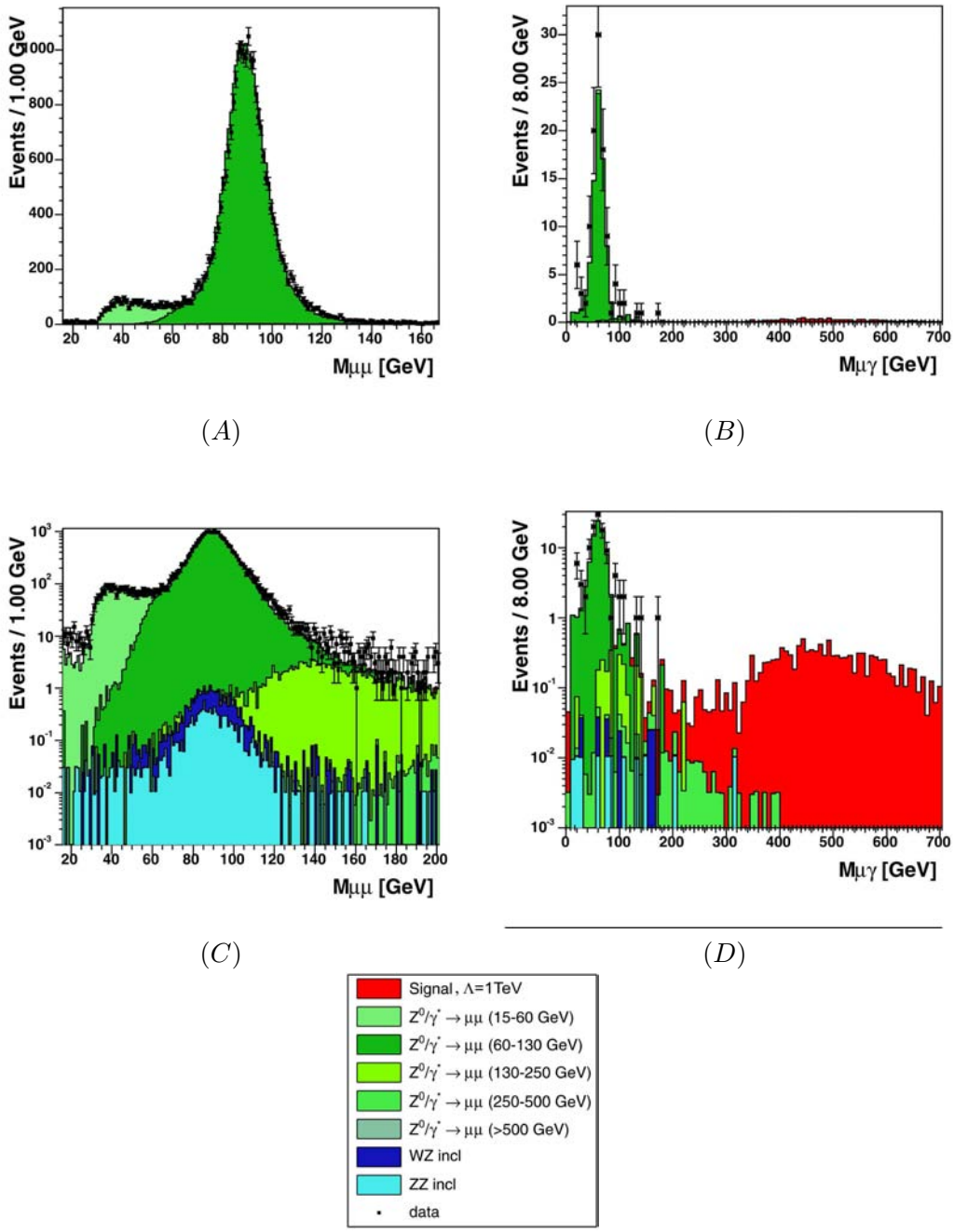

Figure 9.3: (A,C) Invariant dimuon mass after dimuon selection; (B,D) Reconstructed $\mu\gamma$ mass (with the highest energetic muon) after dimuon+photon selection, without kinematic fit. The plots are shown twice, once linear and once with log. scale.

The upper row shows the linear, the lower row the logarithmic plots. In both cases the agreement within statistical errors is reasonable.

The excess in data in (C) for small masses exists due to the requirement of only one isolated muon, which leaves the data with a small QCD contribution in this area. The excess in the the plots (B) and (D) is quite small and gets even smaller if accounting for the systematic uncertainties as well. It seems that the photon selection is not as well understood as the DiMuon selection.

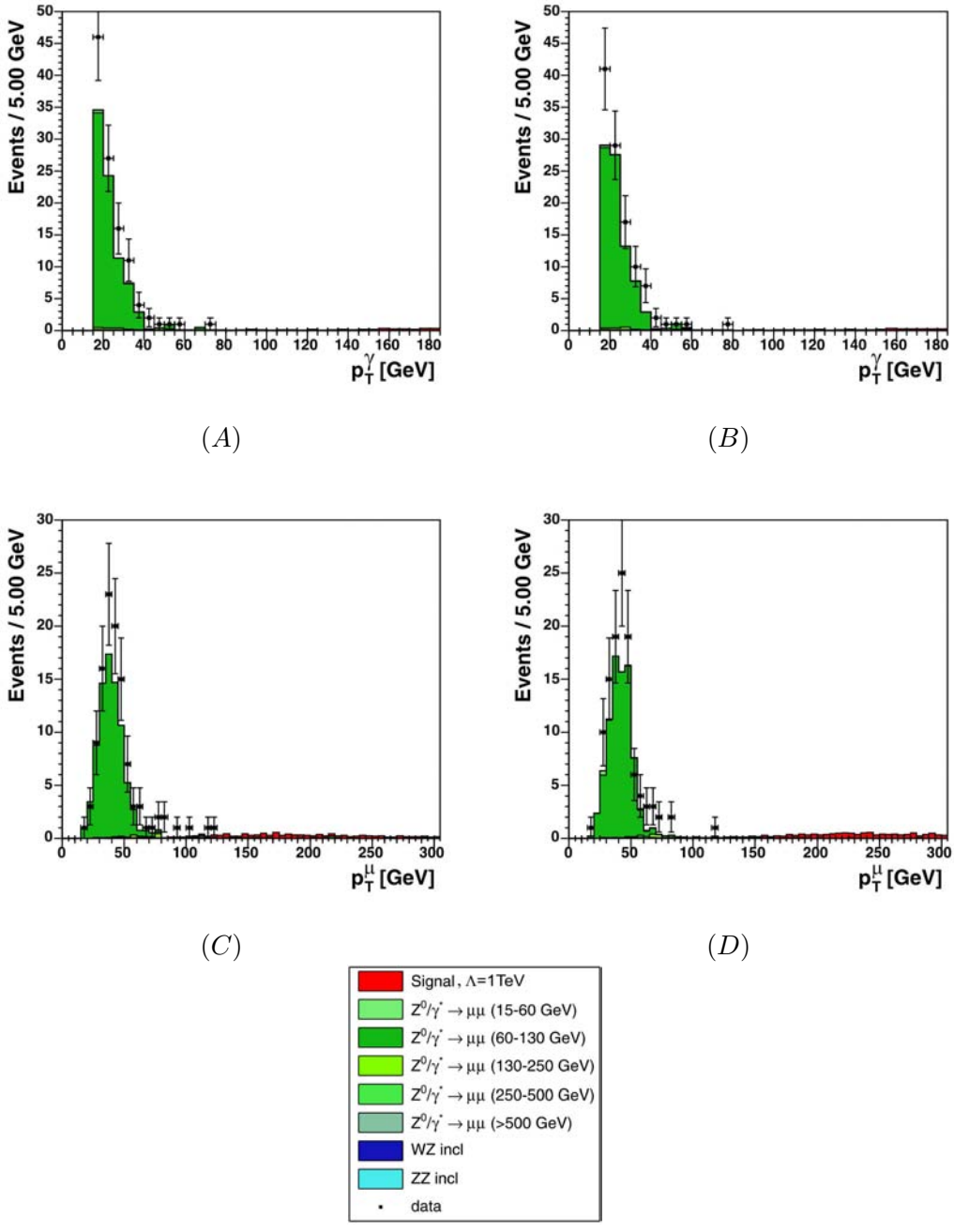

Figure 9.4: (A) p_T distribution of highest energetic photon after the γ selection. (B)p_T distribution of highest energetic photon after the γ selection, with kinematic fit. (C) p_T distribution of highest energetic muon after the γ selection.(C) p_T distribution of primary muon after the γ selection with fit. Plots include signal events with M(μ^*)=500 GeV and Λ=1TeV.

Figure 9.4 shows the transverse momenta for the highest energetic muon ((C)&(D)) and photon ((A)&(B)) before and after the kinematic fit. The agreement agreement within statistical errors is reasonable, but these

plots show that the muon momenta as well as the momenta of the photon are only slightly adjusted by the kinematic fit, no harsh changes have been made in these distributions.

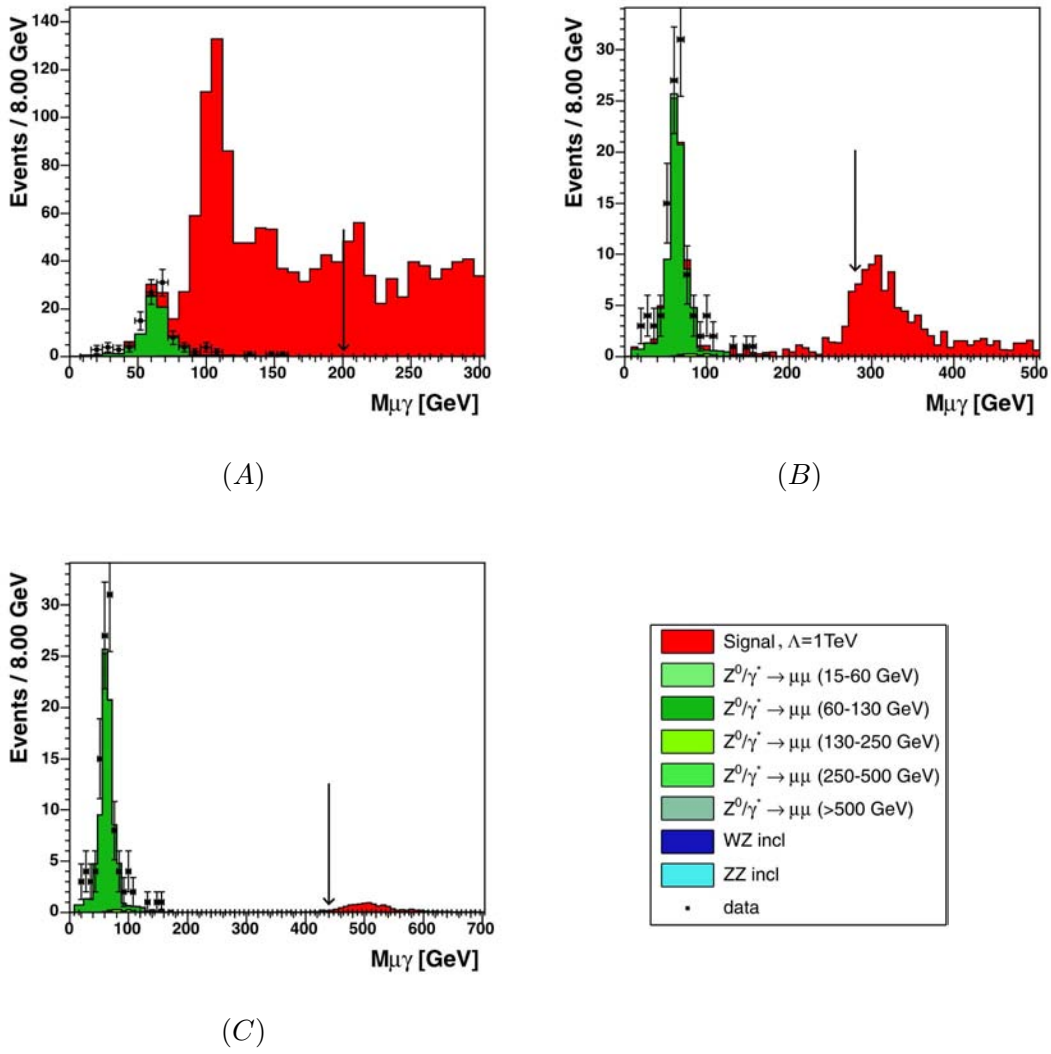

Figure 9.5: Shown is the invariant muon and photon mass for the signal points 100 GeV, 300 GeV, 500 GeV after the kinematic fit was applied.The arrows indicate the values for the final cut.

The invariant mass spectra displayed in Figure 9.5 show the agreement of data and Monte Carlo as shown before in Figure 9.3.

More important, they show the signal invariant mass distributions together with the data and SM Monte Carlo. The Signal Monte Carlo clearly peaks at the denominated values, and there is no signal in the data.

Chapter 10

Results

Since no excess is observed in data, upper limits on the cross section and lower limits on the μ^* mass are calculated as described in chapter A, using the Bayesian approach and poisson statistics for the actual calculation, with the program limit_calc [78].

Systematic uncertainties originating from e.g efficiency corrections [49] (Sect. 8.2) are correctly included according to section 8.3. The final event numbers and signal efficiencies are shown in Table 10.1.

The resulting cross section limits can be found in Table 10.2 and Figure 10.1, leading to a mass limit for the excited muon of

696 GeV at 95 % CL., for $\Lambda = m_{\mu^*}$

For the interpretation of these results one has to consider four things:

1. The theoretical NNLO corrections [39] to the cross section,
2. the actual branching ratio for gauge mediated decays, depending on m_{μ^*}/Λ(sec. 5.3),
3. the scale Λ for which the mass limit is calculated (typically $\Lambda = m_{\mu^*}$),
4. the method to calculate the intersection of experimental limit and theoretical prediction,

The first three depends strictly on the `Pythia` [33, 37] implementation as well as the branching ratio calculations, and can be recalculated independently from the experimental cross section limits. To correct the LO `Pythia` cross section a k-factor according to Table 6.3 is used, leading to a slightly higher limit (696 GeV instead of 685 GeV with LO).

The last dependency is a more subtle one: In this calculation, the limits as well as the theoretical cross section points are linear interpolations [59]. This leads to intersections, which mark the μ^* mass limit, which therefore depend on the method used for interpolation.

10.1 Final Event Sample and Signal Efficiency

These are the final numbers for this analysis, representing every signal mass with its efficiency and the data and background events.

All points have a very similar signal efficiency except the lower mass point at 100 GeV, which is - as explained before - special due to the position near the Z-peak. For this low mass point the simple cut based analysis is made to cut hard into the background distribution.

Signal m_{μ^*}[GeV]	data events	SM background events	Signal eff.[%]
100	0	0.132 ± 0.041	8.8 ± 1.1
200	0	0.132 ± 0.041	13.8 ± 1.7
300	0	0.034 ± 0.014	14.0 ± 1.8
400	0	0.009 ± 0.004	17.0 ± 2.1
500	0	0.002 ± 0.001	15.6 ± 2.0
600	0	0.002 ± 0.001	16.9 ± 2.1
700	0	0.002 ± 0.001	15.6 ± 1.9
800	0	0.002 ± 0.001	15.9 ± 2.0
900	0	0.002 ± 0.001	15.5 ± 2.0
1000	0	0.002 ± 0.001	15.5 ± 1.9

Table 10.1: Data, SM background and signal efficiency after final cuts with fit. The error include statistics as well as systematics with the error due to photons from misidentified jets being negligible at this stage.

10.2 Limits

10.2.1 $\sigma \times BR$ Limits for Excited Muon Production

Signal (m_{μ^*})[GeV]	$\sigma \times BR$ @ 95% CL (w. fit)[pb]	$\sigma \times BR$ @ 95% CL (w/o fit)[pb]
100	0.096	0.107
200	0.061	0.065
300	0.060	0.068
400	0.049	0.056
500	0.054	0.069
600	0.050	0.056
700	0.054	0.060
800	0.053	0.056
900	0.054	0.056
1000	0.054	0.056

Table 10.2: Upper Limits on the excited muon $\sigma \times BR$ at different signal points; Signal MC was produced with $\Lambda = 1TeV$

Since there are many different viewing points onto excited muon production one can calculate the different mass limits for varying couplings F and Λ. Therefore Table 10.2 gives the experimental limits on $\sigma \times BR$

used to calculate the mass limit at F'=F=1 and $\Lambda = m_{\mu^*}$. What can be seen, is that the limit is distributed quite flatly and is slightly better for the results using the kinematic fit, which results in a slightly better limit for the mass limit as well, shown in the following section.

10.2.2 Limits on the Excited Lepton Mass

.

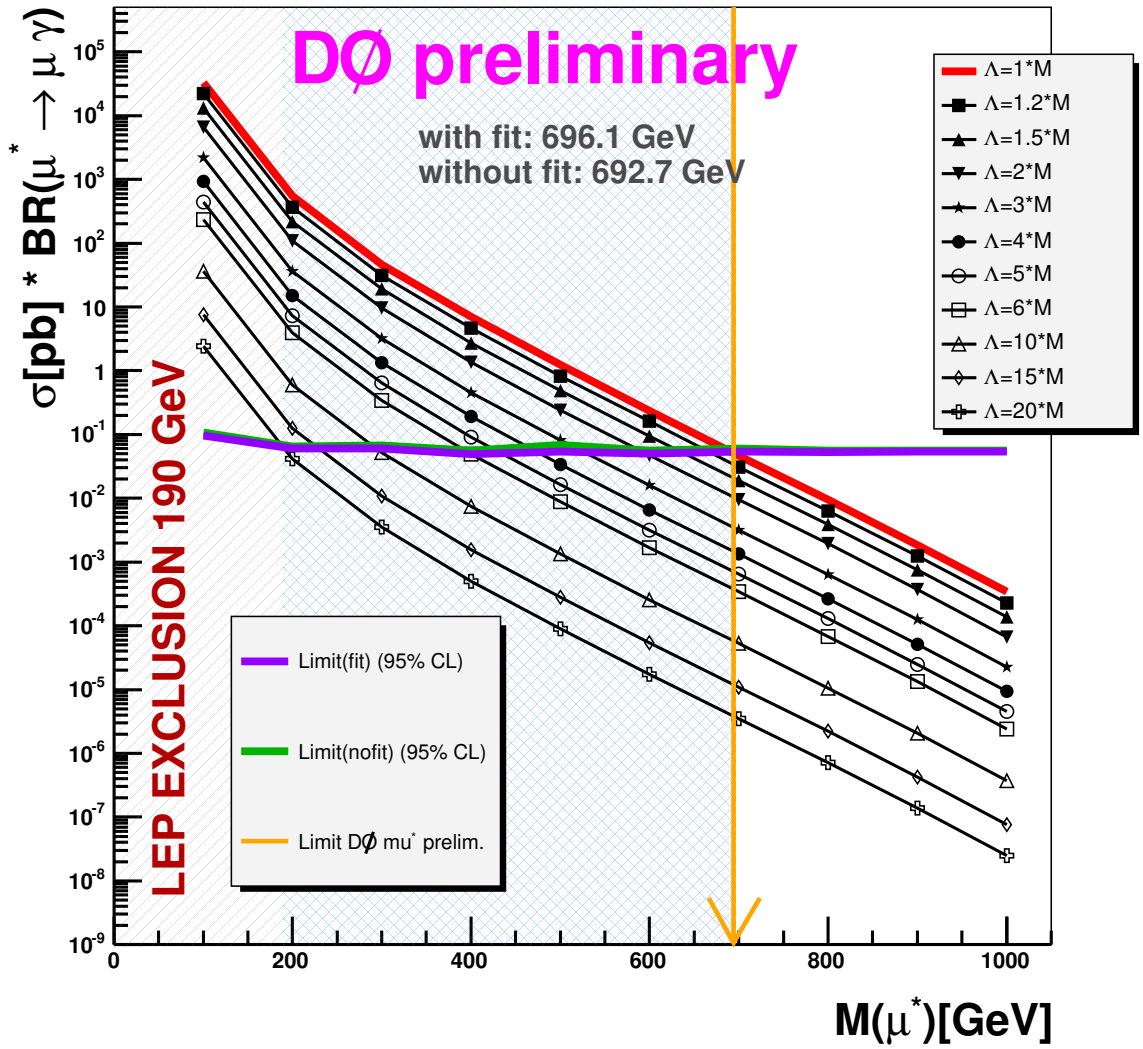

Figure 10.1: The plot shows the usual approach, comparing the calculated 95% CL limit with the theoretical σ_{prod} at scale values $\Lambda = n \cdot m_{\mu^*}$ (With included overall BRs).

Figure 10.1 and 10.2 shows the cross section and mass limits as well as an exclusion region for single μ^* production with $m_{\mu^*} = \Lambda$ from the LEP collider [54, 55] for $F = F' = \Lambda/m_{\mu^*}$.

Figure 10.1 shows the usual approach setting the limit at $m_{\mu^*} = \Lambda$. Since it has been shown that the branching ratio depends strongly on the ratio of these parameters, one can see that the mass limit strongly depends on the choice of m_{μ^*}/Λ.

In order to give a feeling what the actually dependence on the scale is, Figure 10.1 shows the same plot with the difference that the theoretical cross section is shown at several fixed values of Λ. All these different theoretical curves together with the measurements are combined in Figure 10.3.

The Figures 10.1 - 10.3 contain theoretical cross sections all correctly adapted to the displayed parameters m_{μ^*} and Λ. The correct branching fractions have been calculated as described in section 5.3 [6, 7].

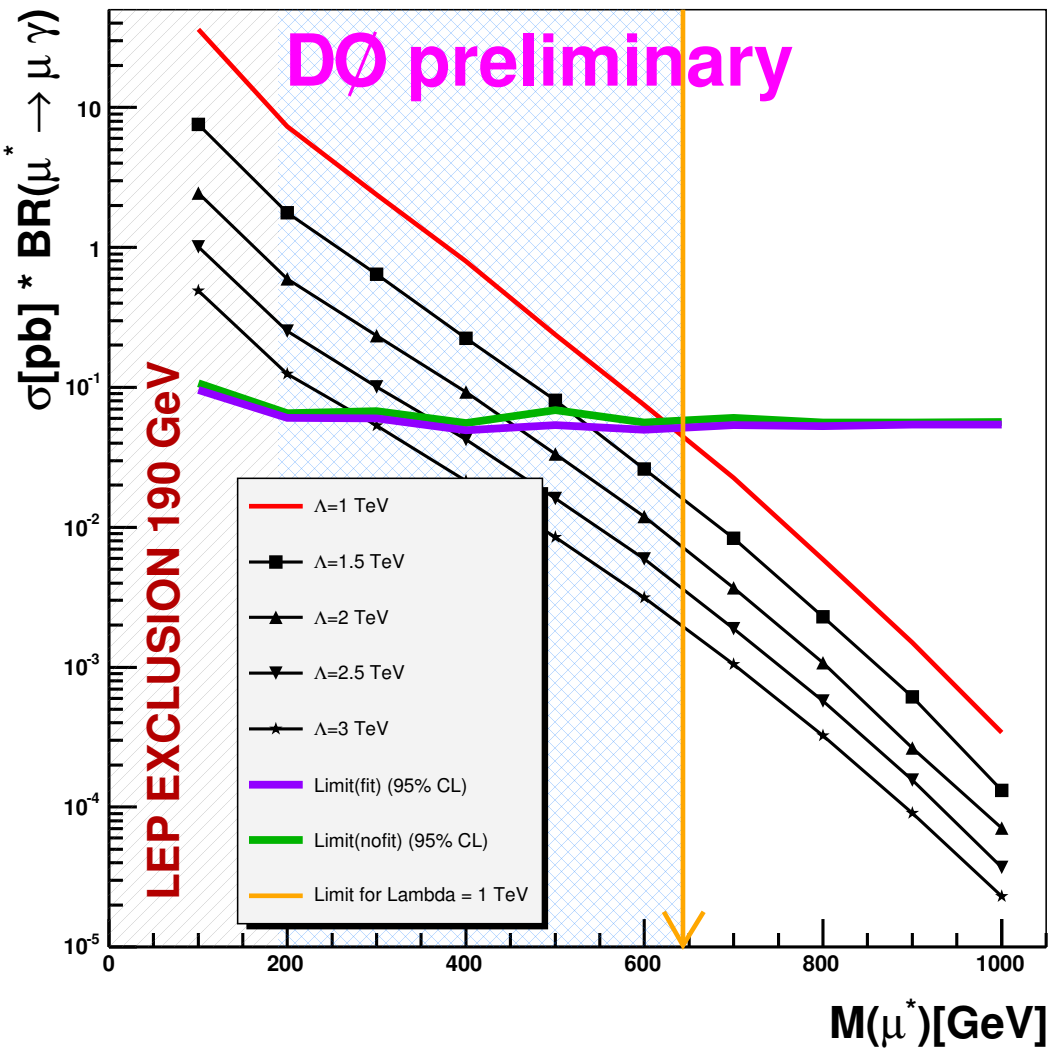

Figure 10.2: The plot displays the limit for fixed values of Λ (With included overall BRs).

10.2.3 Limits on the Scale Λ

Another interpretation of this analysis can be obtained from the various intersections of theory graphs and calculated limits in Fig. 10.1 and 10.2, the result is displayed in Fig. 10.3. One can exclude scale values Λ depending on the μ^* mass. Both parameters should be considered equally important as one wants to know if there is a substructure, at which scale and how this substructure represents itself (e.g. as an excited lepton).

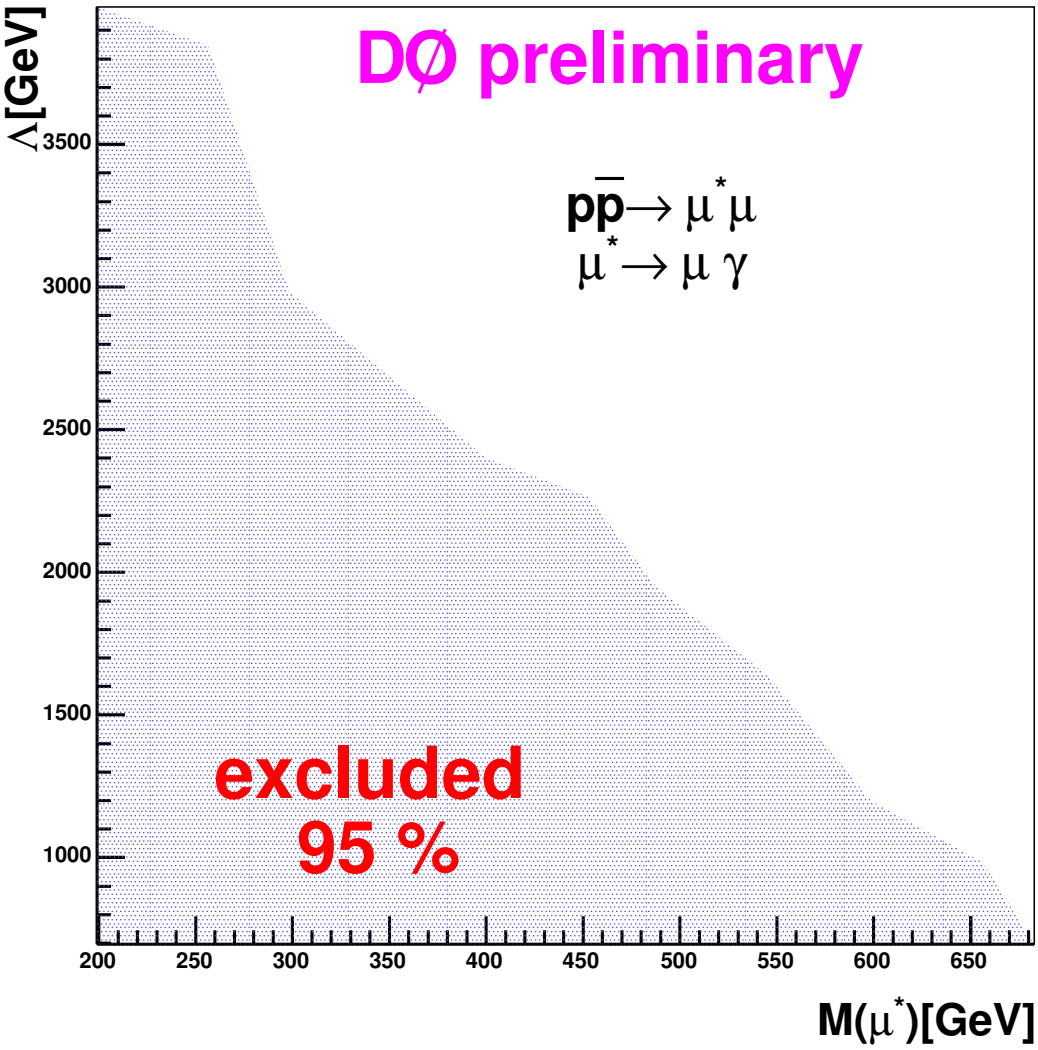

Figure 10.3: 95% CL exclusion limit on Λ as a function of m_{μ^*}, based on the intersections of theory and experimental cross section in Fig. 10.1.

On the other hand this can as well be seen as a plot presenting the different mass limits for different scales: The lower the scale the higher the excluded mass limit, while for large scales only small excited muon masses can be excluded.

Remarks on the CDF e* limit of 879 GeV: The other Tevatron Experiment, CDF, published a result on excited electrons in 2004 [80], which should be comparable to this analysis, since the model used for both excited leptons is quite the same except for the signature which would incorporate electrons and a photon instead of muons. Therefore during the evolution of this analysis a few comparisons have been made, revealing some intriguing problems.

In order to compare the DØ and the CDF analyses [80] one has to take several things into account.

The CDF limit for excited electrons at $\Lambda = m_{e^*}$ is m_{e^*}= 879 GeV via the CI production process [80], using an older version of Pythia and assuming gauge mediated decays for the e^* only. Meaning all excited electrons decay via gauge mediation and the three channels have a branching fraction according to the electroweak decay width. For the excited electron with masses above 300 GeV the $e\gamma$ decay mode has a branching fraction of 0.3.

Since all versions of Pythia below 6.211 have an extra factor of two included in the cross section implementation [34] the limit is about 30 GeV too high just by accounting for this factor.

As mentioned above an additional difficulty is caused by the implicit assumption that gauge mediated decays would dominate the decay of excited muons, which, as is shown in section 5.3 is not true in most cases. The assumption is only correct if $m_{e^*/\mu^*} << \Lambda$, as one can crosscheck with Fig. 5.4.

Only $\sim 8\%$ of the μ^* decays are gauge mediated for $\mu^* = \Lambda$ and therefore the branching ratio for the $\mu\gamma$ is not $\sim 30\%$ channel but $\sim 2.4\%$ leading to a much lower mass limit. In case of the analysis at hand the μ^* limit would rise drastically to ~ 890 GeV if adjusting for the two factors and ~ 860 GeV if assuming dominant gauge mediated decay, generated with the correct `Pythia`.

Chapter 11

Summary

11.1 Conclusion

This analysis presented the first search for excited muons at the DØ experiment in RunII. Single excited muon production via contact interactions was examined. The final state $\mu\mu\gamma$ in the gauge mediated decay mode was the observed signature.

Since no excess is observed in data, upper limits on the $\sigma \times BR$ as well as lower limits on the excited muon mass are calculated based on [6, 7].

An improvement of the limit with more data is possible.

The presented mass limit excludes excited muon production for masses below 696 GeV for $\Lambda = m_{\mu^*}$ and F=F'=1, at 95 % CL. The limit represents the use of the current knowledge on the excited muon production via contact interaction included in the `PYTHIA` routines and takes into account the branching ratios for the gauge mediated processes as a whole, which has not been done before in a search for excited muons.

One of the first critical parts of this analysis was the implementation of excited muon production into a given Monte Carlo generator and into the experimental framework.

This implementation was quite successful and the customized version of `Pythia` is now used in a diploma thesis for the CMS detector at the future LHC as well, which is observing the same channel.

The data and Monte Carlo selection as shown is well understood. The part with the most potential for adjustments seems to be the photon selection. The final selection reveals that no signal can yet be seen, and the only thing possible is to set limits.

One always has to keep in mind that the mass limit is dependent on the scale at which one assumes Contact Interactions to take place. For higher scales the mass limit is far smaller.

11.2 Outlook

Even though this analysis is finished with this Diploma, there a few remarks on the future of excited muons or leptons. Excited leptons are an interesting field of research especially at the coming accelerators like LHC and ILC, since at both of these machines the possible Contact Interactions could play an important role. If there is such a thing like compositeness of the fundamental fermions, it seems possible that the LHC should be able to detect it since its center of mass energy is far higher, and therefore much higher scales can be covered.

Regarding this analysis there are still a few things that could not been done in the time of a diploma theses and should be covered in a next analysis:

- the gauge mediation process could be analyzed
- the deviations in the photon selection should be analysed more carefully
- the analysis has to be performed for the LHC (C. Zeidler) and ILC and then cover higher masses and scales
- the analysis on excited electrons (A. Meyer, V. Vorwerk) should be combined with results presented here

This corner of physics beyond the Standard Model is quite interesting due to its clear signature, but since this analysis uses a simple four fermion model its limited to a general search.

Especially if a signal is found in data, one has to take steps in order to cover the different approaches of compositeness and determine what the true nature of the underlying structure and the new interaction is like.

Chapter 12

Acknowledgement

First of all, I would like to express my deepest gratitude to my parents who had never any doubt in my abilities and always supported me in life and work. Even during the hardest of times in the last 2 years both of them always found the right words and strength.

My special thank you goes to Prof.Dr.T Hebbeker, who offered me the possibility to write my thesis in his group,not to mention the many different opportunities to step into the world of experimental particle physics, like visiting the DØ experiment at Fermilab. He always was able to help with his patience and his fruitful contributions.

I would like to extend my thank you Prof. Dr. M. Erdmann for agreeing to be the second examiner.

For the great advice and support of my colleagues in the local DØ group i am very grateful: Arnd Meyer Steffen Kappler Christian Autermann, Philip Biallass, Carsten Magass, Oliver Kraff and Patrick Eraerds, as well as many people at Fermilab and other Institutions around the world, who helped with various aspects of my thesis.

I am especially grateful to Daniela Käfer, who always found time and patience to help me even in the most panicking times.

I owe special thanks to my twin-brother Björn for his ongoing support and help during the last years. Without him I would have never gotten that far. My gratitude also goes to my fellow students and friends especially to Stefan Bargel for his help during many hours of exercises and exams and to Patrick Marche and Jan-F. Schorr for their support.

A somewhat outstanding and unusual 'Thank You' goes to Eugene W. Roddenberry for his inspirational work enabling me 'to boldly go" where i have "never gone before".

I hope that the new diploma students like Volker Vorwerk enjoy their work at DØ and take great pleasure in working with such great people.

Bibliography

[1] H. Terazawa, Y. Chikashige and K. Akama, Phys. Rev. D 15 (1977) 480

[2] Y. Ne'eman, Phys. Lett. B 82(1979) 69

[3] Luminosity ID Documentation, http://www-d0.fnal.gov/phys_id/luminosity/notes

[4] "The Upgraded DØ Detector", Nucl. Instr. and Methods xxxx (2005), hep-physics/0507191; Fermilab-Pub-05/341-E

[5] H. Terazawa, M. Yasue, K. Akama, M. Hayashi: Phys.Lett.B 112(1982) 387
F.M. Renard: Il Nuovo Cimento, 77A 1983) 1
A. De Rujula, L. Maiani and R Petronzio: Phys. Lett. B 140 (1984) 253
E.J. Eichten K.D. Lane, and M.E. Peskin: Phys. Rev. Lett 50 (1983) 811

[6] U. Baur, M. Spira and P.M. Zerwas, "Excited-quark and Lepton Production at Hadron Colliders", Phys. Rev. D 42,3(1990)

[7] O. Cakir, C. Leroy, R. Mehdiyev, A. Belayev, "Production and Decay of excited electrons at the LHC", Eur Phys J C 30, d01 (2003) 005

[8] K. Hagiwara, S. Komamiya, and D Zeppenfeld, "Excited Lepton Production at LEP and HERA", Z. Phys. C 29, 115-122 (1985)

[9] F.Boudjema, A. Djouadi and J.L. Kneur, "Excited Fermions at e^+e^- and eP Colliders", Z. Phys. C 57, 425 (1992)

[10] http://www-sk.icrr.u-tokyo.ac.jp/doc/sk/

[11] T. Hebbeker, Lecture: "Elementarteilchenphysik I & II", RWTH, SS 2004 & WS 04/05

[12] F.Halzen and A.Martin, "Quarks & Leptons:An Introductory Course into modern particle Physics", John Wiley & Sons

[13] S. Chekanov et al., "ZEUS next-to-leading-order QCD analysis of data on deep inelastic scattering", Phys. Rev. D 67 ,012007 (2003)

[14] http://d0server1.fnal.gov/projects/Silicon/www/silicon.html

[15] http://d0server1.fnal.gov/projects/SciFi/cft_home.html

[16] http://www-d0.fnal.gov/hardware/upgrade/
muon_upgrade/muon_upgrade.html

[17] http://www-d0online.fnal.gov/www/groups/cal/cal_main.html

[18] "DØ Silicon Tracker Technical Design Report"
http://d0server1.fnal.gov/projects/silicon/www/tdr_final.ps

[19] The DØ Collaboration, S. Abachi et al: 'FERMILAB-PUB-93/179-E'
Nucl. Instr. Methods, A338,185 (1994)

[20] The DØ Collaboration, S. Abachi et al: "The DØ Upgrade, The Detector and its Physics" 1996

[21] GoogleEarth: http://earth.google.com/

[22] Fermilab Visual Media Services, http://www-visualmedia.fnal.gov/

[23] http://www-d0.fnal.gov/Run2Physics/WWW/drawings.htm

[24] http://www-d0.fnal.gov/Run2Physics/displays/presentations/

[25] http://isnpx0162.in2p3.fr/d0/documentation/
materiel/figure_d02/schemas/

[26] http://d0server1.fnal.gov/projects/SciFi/
pictures/CFT_Detector.html

[27] http://www-d0.fnal.gov/∼hagopian/muon_run2_detector.ps

[28] http://d0server1.fnal.gov/users/qianj/CPS/doc/dn3104.pdf

[29] "The Run II Handbook", http://www-bd.fnal.gov/runII/index.html

[30] "The updated DØ luminosity determination, short", DØ-Note 4328

[31] T. Sjöstrand "The PYTHIA Event Generator" , CERN and Lund University
http://www-cpd.fnal.gov/personal/mrenna/041207_pythia_tutorial/
01_041207_pythia_tutorial_TS_1_intro4.pdf

[32] K. Lane, "Electroweak and Flavor Dynamics at Hadron Colliders", hep-ph/9605257

[33] T. Sjöstrand et al, Computer Phys. Commun. 135 (2001) 238.
T. Sjöstrand, L. Lönnblad, S. Mrenna, P. Skands (2002): "Pythia 6.2 - Physics and Manual",
http://www.thep.lu.se/∼torbjorn/Pythia.html
Pythia Version 6.225

[34] Pythia 6.211 : 22 October 2002,
http://www.thep.lu.se/∼torbjorn/pythia/pythia6228.update

[35] CTEQ Parton distributions, http://zebu.uoregon.edu/∼parton/partonCTEQ.html

[36] CompHEP - a package for evaluation of Feynman diagrams and integration over multi-particle phase space, http://www.ifh.de/∼pukhov/comphep.html
A. Semenov. Nucl.Inst.&Meth. A393 (1997) p. 293, http://theory.sinp.msu.ru/∼semenov/lanhep.html

[37] J. W. Coenen, Customization of Pythia 6.225 and Integration Into the DØ-Framework,
private communication with A. Meyer, G. Brooijmanns("stripping" Pythia routines) (2004)
(see this Thesis)

[38] T. Nunnemann, "NNLO Crossection for Drell Yan, Z and W Production using Modern Parton Distribution Functions", DØ Note 4476 (2004), http://www-clued0.fnal.gov/∼nunne/
cross-sections/dy_cross-sections.html

[39] private communication with A. Daleo (Spring '05)

[40] R. Hamberg, W.L. van Neerven and T. Matsuura, "ZPROD", 'Nucl. Phys. B359 (1991) 343.'

[41] DØ EM-ID Group,
http://www-d0.fnal.gov/phys_id/emid/d0_private/emid.html

[42] Muon smearing. http://www-d0.fnal.gov/Run2Physics/top/
d0_private/wg/production/analysis_summer04/muon_smearing.txt.

[43] DØgstar
http://www-d0.fnal.gov/computing/MonteCarlo/simulation/d0gstar.html

[44] DØsim
http://www-d0.fnal.gov/computing/MonteCarlo/simulation/d0sim.html

[45] GEANT - Detector Description and Simulation Tool
http://wwwasd.web.cern.ch/wwwasd/geant/

[46] D0 Run II Monte Carlo Simulations
http://www-d0.fnal.gov/computing/MonteCarlo/MonteCarlo.html

[47] D0 Farm Production Page
http://www-d0.fnal.gov/computing/production/

[48] H.K. Gerberich, Search for Excited Or Exotic Electron Production using the di-electron + photon Signature at CDF in Run II, Duke University, 2004

[49] C. Autermann, private communication
D. Kaefer, D0 Note in preparation (2005)

[50] P.A. Biallass, O. Kraff, T. Hebbeker ,"Model Independent Search for New Physics"
'D0 Note 4719' , 2005

[51] P.A. Biallass, "Model Independent Search for New Physics"
"Diploma Thesis", RWTH, 2004

[52] F. Deliot and G. Hesketh. "Measurement of $\sigma(p\bar{p} \rightarrow WX) \times (W \rightarrow \mu\nu)$ at $\sqrt{s} = 1.96TeV$"
DØ-Note 4749

[53] J.M. Campell and R.K.Ellis,"An update on vector boson pair production at hadron colliders",
Phys. Rev. D 60,113006 (1999), DØ Note 4476 (2004)

[54] Particle Data Group, Review of Particle Physics, Phys. Lett. B 592 (2004) 1

[55] The Opal Collaboration, "Search for Excited Leptons in e^+e^- Collisons at $\sqrt{s} = 183 - 209$ GeV",
Phys.Lett.B 544:57-72(2002)

[56] R. Hauser, A. Yurkewicz:"Thumbnail Streaming"' (2002)
http://www-d0.fnal.gov/d0dist/dist/packages/np_tmb_stream/
devel/doc/tmb_streaming.pdf

[57] H Schellmann and M Verzocchi,
http://www-d0.fnal.gov/phys_id/luminosity/data_access/
lm_access/doc/runrangeluminosity.html

[58] M. Klute, L. Phaf and D. Whiteson, "TopAnalyze - A Framework Analyze Package for Top Group Analyses", http://www-d0-fnal.gov/Run2Physics/top/d0_private/wg/top_analyze/Ipanema/Ipanema.html, DØ Note 4122

[59] R. Brun et al., Root version 4.00/08, http://root.cern.ch/root/html400/TGraph.html

[60] http://root.cern.ch/root/html400/TMinuit.html

[61] J.A.M. Vermaseren: "Axodraw", Comp. Phys. Comm. 83:45-58, (1994) http://www.nikhef.nl/~t68/axodraw/

[62] B. Vachon et al., DØ-Note 4512, http://www-d0.fnal.gov/Run2Physics/top/d0_private/wg/triggers/TriggerEfficiency/TriggerEfficiency.html http://www-d0.fnal.gov/cgi-bin/cvsweb.cgi/top_trigger/doc/top_trigger.html http://www-d0.fnal.gov/Run2Physics/top/d0_private/wg/triggers/

[63] TriggerEfficiency documentation http://www-d0.fnal.gov/cgi-bin/cvsweb.cgi/top_trigger/doc/

[64] Triggermeisters Webpage http://www-d0online.fnal.gov/www/groups/tm/tm_main.html

[65] Offline Run Quality Database http://d0db-prd.fnal.gov/qualitygrabber/qualQueries.html

[66] JET/MET Run & Lumi-Block Selection http://www-d0.fnal.gov/computing/algorithms/calgo/jet_met/runsel.html

[67] Bad Ring-of-Fire lumi blocks http://d0-france.in2p3.fr/WORKING_GROUPS/DQ/RF/lum_blocks_mht30_bad.dat

[68] Baur and E.L. Berger, "Probing the WWγ vertex at the Tevatron Collide", Phys. Rev. D 41, 1476 (1990)

[69] MC_RUNJOB http://www-clued0.fnal.gov/runjob/

[70] RunII Stores and Runs, http://www-d0online.fnal.gov/www/groups/tm/daqrates/current_store_autoupdate.html

[71] Common Sample Group main page, http://www-d0.fnal.gov/Run2Physics/cs/ index.html http://www-d0.fnal.gov/Run2Physics/cs/skimming/pass2.html

[72] TMB Fixing, http://www-d0.fnal.gov/Run2Physics/cs/fixing/fixing.html

[73] Muon ID/ Algorithms group, http://www-d0.fnal.gov/~hedin/mures.jpg http://www-d0.fnal.gov/phys_id/muon_id/d0_private/muon_id.html

[74] The Top Physics Working Group of the DØ Collaboration. DØ top analysis and data sample for the winter conferences 2004. DØ-Note 4419.

[75] Bing Zhou, Quichun Xu, and James Degenhardt. Parameterized monte carlo simulation muon package. DØ-Note 4065.

[76] A. Alton, A. Askew et al., http://www-d0.fnal.gov/Run2Physics/d0_private/eb/Run2EB_016/ Z-gamma/D0Note-drafts/z_gamma_v2.0.pdf, DØ-Note 4488

[77] A. Alton, A. Askew et al., Measurement of W γ Events in DØ RunII Data, DØ-Note 4410 v0.3

[78] J. Hobbs, G. Landsberg, http://www-d0.fnal.gov/∼hobbs/limit_calc.html, DØ-Note 3476

[79] V. Büsher , J-F. Grivaz, J. Hobbs, "Recommendation of the Ad-Hoc Committee on Limit-Setting Procedure to be Used by DØ in Run II", DØ- Note 4629

[80] CDF Collaboration, "Search for Excited and Exotic Electrons in the $e\gamma$ Decay Channel in $p\bar{p}$ Collisions at $\sqrt{1.96}$ TeV", Phys.Rev.Lett 94 (101802) 2005

[81] The LEP collaborations: "Combination procedure for the precise determination of Z boson parameters from results of the LEP experiments", hep-ex/0101027 (2001)

[82] ALEPH Collaboration, DELPHI Collaboration, L3 Collaboration, OPAL Collaboration and The LEP Working Group for Higgs Boson Searches: "Search for the Standard Model Higgs boson at LEP" Phys. Lett. B 565 (2003) 61

[83] The DØ Collaboration: "A precision measurement of the mass of the top quark", Nature, Vol. 429, 10, June 2004

[84] "CMS Broschure" http://cmsinfo.cern.ch/Welcome.html/CMSdocuments/CMSbrochure/CMS-Brochure03.pdf

List of Figures

List of Tables

Appendix A

Limit Calculation

The following chapter is meant to give a short introduction into the concept of limit calculation with the bayesian approach. This overview is based on the Particle Data Groups' "Review of Particle Physics"[54] as well as on references [78, 79].

A.1 General Statistics - Probabilities

Since the definition of a probability is a tricky thing without using words like 'probable' etc., in the following a quite abstract definition is used. This definition can be given by considering a set S called the sample space and possible subsamples $A, B, ...$, for which no interpretation will be given.

The probability P is a real-valued function defined by 3 axioms first proposed by Kolmogorov as :

1. For every subset A in S, $P(A) \geq 0$.
2. or disjoint subsets (i.e. $A \cap B = \varnothing$), $P(A \cup B) = P(A) + P(B)$.
3. $P(S) = 1$

In order to deal with conditional states one introduces the conditional probability $P(A|B)$ (P of A given B) defined as:

$$P(A|B) = \frac{P(A \cap B)}{P(B)} \tag{A.1}$$

Form this definition one easily obtains the Bayesian theorem, since $A \cap B$ equals $B \cap A$ and hence

$$P(A \cap B) \; = \; P(A|B)P(B) \; = \; P(B|A)P(A) \; = \; P(B \cap A).$$

$$P(A|B) = \frac{P(B|A)P(A)}{P(B)} \quad (Bayes' \; theorem) \tag{A.2}$$

From this and the three axioms one obtains the law of total probability:

$$P(B) = \sum_i P(B|A_i)P(A_i) \tag{A.3}$$

for any subset B and for disjoint sets A_i with $\cup_i A_i = S$. which now leads to the generalized form of bayes' theorem:

$$P(A|B) = \frac{P(B|A)P(A)}{\sum_i P(B|A_i)P(A_i)} \quad (Bayes' \; theorem) \tag{A.4}$$

The subsets of the sample space can be interpreted as hypotheses, i.e., statements which might either be true or false. Such a statement may refer to the mass of a particle or to a cross section. In this approach P(A) is a subjective probability and can be interpreted as a degree of belief that the hypothesis A is actually true.

This approach is used in Bayessian statistics leading to :

$$P(\text{theory}|\text{data}) \propto P(\text{data}|\text{theory})P(\text{theory}) \tag{A.5}$$

With:

- P(theory) the *prior* representing the a priori probability for the outcome of the measurement.
- P(data|theory) the *likelihood*, the probability to have gotten the data actually obtained for the given theory

A.2 Confidence Intervals and Limits - Bayesian Approach

As pointed out above a typical approach to make any inferences about a set of parameters is made using Bayes' theorem. In a search for new particles one defines *parameter of interest*, the cross section for example (σ) and a set of *nuisance parameters* (λ) that typically influence the deduction of the actual *parameter of interest*.In the case of this analysis e.g. signal efficiencies and acceptances and background would be nuisance parameters.

Bayes' theorem can be written as:

$$p(\sigma, \lambda|\mathbf{x}) = \frac{\mathbf{p}(\mathbf{x}|\sigma, \lambda)\pi(\sigma, \lambda)}{\int\int \mathbf{p}(\mathbf{x}|\sigma, \lambda)\pi(\sigma, \lambda)\mathbf{d}\lambda\mathbf{d}\sigma} \quad (Bayes' \; theorem) \tag{A.6}$$

The function $p(\sigma, \lambda)$ represents the *posterior density function*, while $\mathbf{p}(\mathbf{x}|\sigma, \lambda)$ and $\pi(\sigma, \lambda)$ in this notation represent *model* density and *prior* density, respectively.

In this case continuous variables are used which one might notice as a difference to the previously explained notation.

Cross Section: The canonical model density for a cross section measurement is

$$\mathbf{p}(\mathbf{n}|\sigma,\lambda) \;=\; \prod_{i=1}^{K} \text{Poisson}(\mathbf{n_i}, \mathbf{a_i}\sigma + \mathbf{b_i}), \tag{A.7}$$

for K channels with n_i observed events, signal acceptance a_i and background b_i. In this model a and b would be the nuisance parameters (λ).

The prior can be factorized

$$\pi(\sigma,\lambda) = \pi(\lambda|\sigma)\cdot\pi(\sigma).$$

$\pi(\sigma)$ represents a prior that only involves the cross section, while $\pi(\lambda|\sigma)$ gives the prior for the nuisance parameters given a certain cross section (conditional).

Usually it is not clear what kind of function should be used for the prior, as a matter of convention at DØ a flat prior for the cross section in an Interval $[0, \sigma_{max}]$ is used.

After integrating over the nuisance parameters one obtains a posterior density function $p(\sigma, \mathbf{n})$ which can be used to obtain an upper limit (σ^u) on the cross section or any other parameter of interest.

For a given desired Confidence Level one can write:

$$CL = \int_0^{\sigma^u} p(\sigma, \mathbf{n}) \tag{A.8}$$

In case of this analysis CL= 0.95 is required, meaning that the probability to reproduce this analysis and finding the same cross section is 95%.

In cases of different priors this upper limit on the cross section is quite sensitive to pathological cases in which producing an upper limit might not be a well understood procedure. It can be shown that the limit can vary "by as much as 30% for reasonable choices of different priors, as long as data is insufficient to justify a deinitive statement"[79].

The actually code, used for this analysis is described at [78]. It is possible to use this package when performing a single channel counting experiment and is used in a number of other DØ analyses.

A.3 Mass Limits

After calculating the limits on the cross section the next step would be to interpret this in the context of a theoretical model, leading to an upper or lower limit on the mass of the searched particle.

Figure A.1 shows the basic principle in case of a lower limit. In order to derive a mass limit this analysis involves the following steps:

1. the theoretical cross section is calculated using `PYTHIA`
2. the cross section is corrected for NNLO effects (Tab. 6.3)
3. the correct branching ratio for the EW decay modes is applied (Tab. 5.1)
4. the cross section points are intrapolated linearly

5. the measured cross section is used to calculate the crossing point between measurement and theoretical curves

6. the crossing point marks the lower limit for the mass

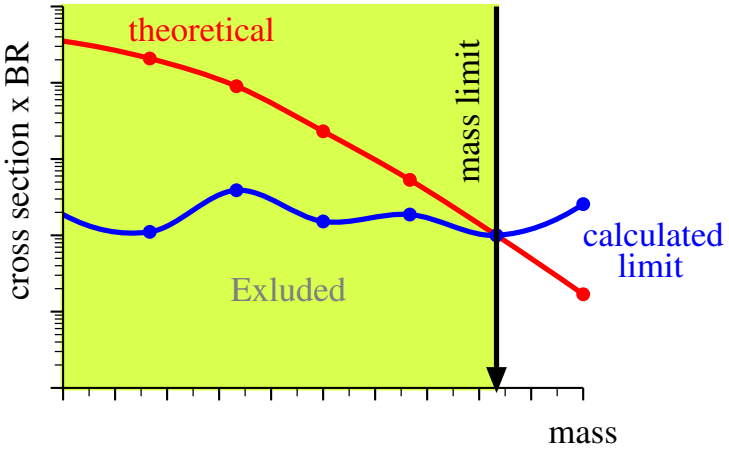

Figure A.1: Simple sketch of the determination of a lower mass limit

This is a straightforward method to calculate the mass limit from the measured cross sections for any number of different theoretical assumptions.

Appendix B

Details on the Customization of Pythia

This Appendix will explain to some extend the work that has be done in order to produce the necessary Excited Muon Monta Carlo. It should be seen in addtion to section 6.4

B.1 Particle Parameters

This section explains the steps toward introducing an excited muon into `Pythia` and give an explanation of the introduced parameters which are stored in `Fortran Common Blocks`. The main work in order to do the excited muon implementation correctly, was to identify all the needed parameters, therefore for interested readers a few more details are given below.

First one introduces a new particle at position KC=500 of the internal `Pythia` particle listing (KC) with charge one (KCHG(500,1)=3). The last value is chosen in order to improve the lucidity of the following changes.

KCHG(KC,1) : three times particle/parton charge for compressed code KC.

The next change is to introduce the excited muon as a color singlet similar to the excited electron (KCHG(500,2)=0) and convince `Pythia` to accept the excited muon as well was its anti-particle (KCHG(500,3)=1)

KCHG(KC,2) : colour information for compressed code KC.
0 : colour-singlet particle. 1 : quark or antidiquark. -1 : antiquark or diquark. 2 : gluon.

KCHG(KC,3) : particle/antiparticle distinction for compressed code KC.
0 : the particle is its own antiparticle. 1 : a nonidentical antiparticle exists.

Since Pythia uses an internal particle listing with numbers from KC=0 up to the last value 500 one now has to define the Particle Data Group particle code which is used consistently throughout the program. An excited(4000000) muon(13) has the value KCHG(500,3)=4000013.

KCHG(KC,4) : equals the uncompressed particle code KF (always with a positive sign).

After the particle is basically implemented a few default values based on the excited electron implementation are set, including the excited muon mass which is set to 425 GeV as the default(analogue to the excited electron). Like every parameter of this default introduction this can later be controlled by card-files for the actual MC production.

PMAS(KC,1) : particle/parton mass m (in GeV) for compressed code KC.

B.2 Particle Decay

The implementation of the decays begins with making the excited muon able to decay by setting the parameter MDCY(500,1) to one and then set the entry point into the decay table for the excited muon. The entry point is chosen to be at the end of the decay table MDCY(500,2)=7998 to improve the lucidity of the changes. *MDCY(KC,1) : switch to tell whether a particle with compressed code KC may be allowed to decay or not.*

0 : the particle is not allowed to decay. 1 : the particle is allowed to decay

MDCY(KC,2) : gives the entry point into the decay channel table for compressed particle code KC. Is 0 if no decay channels have been defined.

MDCY(KC,3) : gives the total number of decay channels defined for compressed particle code KC, independently of whether they have been assigned a non-vanishing branching ratio or not. Thus the decay channels are found at MDCY(KC,2) to MDCY(KC,2)+MDCY(KC,3)-1.

The number of decay channels is MDCY(500,3)=3 located at MDCY(500,2):

$$\mu^* \rightarrow \mu\gamma(7998)$$
$$\mu^* \rightarrow \mu Z(7999)$$
$$\mu^* \rightarrow \nu W(8000).$$

By default, all three decay channels are activated by setting MDME(IDC,1) equal to “1” for the IDCs 7998-8000. The branching ratios BRAT(IDC,1) are set to the default values according to the default excited muon mass.

In order to “teach” Pythia which decay products a decay channel would produce the common blocks KFDP(I,1) and KFDP(I,1) store the information on the first and second particle for each decay mode respectively. In the case of the excited muon’s decay these would be the above mentioned ($\mu\gamma$, μZ, νW).

These steps now simply introduce logical connections for the production and decay routines to find the right choice.

The introduction of the excited muon and the decay channels still does not implement the production process and the decay of the generated excited muon.

B.3 Single Excited Muon Production and Decay Routines

In order to implement the actual production, a new subprocess with the number 170 (internally called ISUB) was implemented into the related common block.

The excited electron routine is copied to be used for single excited muon production:

```
ELSEIF(ISUB.EQ.170) THEN
C...q + qbar -> mu + mu* (excited lepton)
          KFQSTR=KFPR(ISUB,2)
          KFQEXC=MOD(KFQSTR,KEXCIT)
          JS=MINT(2)
          MINT(20+JS)=ISIGN(KFQSTR,MINT(14+JS))
          MINT(23-JS)=ISIGN(KFQEXC,MINT(17-JS))
          JS=3-JS
```

In order to describe the decays correctly the excited electron decay routine is adapted to match the particle code (4000013) of the excited muon and is then reintegrated into the `Pythia` code, as shown below.

```
      ELSEIF(KFLA.EQ.KEXCIT+13) THEN
C...mu* excited lepton.
        FAC=(SH/RTCM(41)**2)*SHR
        DO 465 I=1,MDCY(KC,3)
          IDC=I+MDCY(KC,2)-1
          IF(MDME(IDC,1).LT.0) GOTO 465
          RM1=PMAS(PYCOMP(KFDP(IDC,1)),1)**2/SH
          RM2=PMAS(PYCOMP(KFDP(IDC,2)),1)**2/SH
          IF(SQRT(RM1)+SQRT(RM2).GT.1D0) GOTO 465
          WID2=1D0
          IF(I.EQ.1) THEN
C...mu* -> gamma + mu.
            QF=-RTCM(43)/2D0-RTCM(44)/2D0
            WDTP(I)=FAC*AEM*QF**2/4D0
            WID2=1D0
          ELSEIF(I.EQ.2) THEN
C...mu* -> Z0 + mu.
            QF=-RTCM(43)*XW1/2D0+RTCM(44)*XW/2D0
            WDTP(I)=FAC*AEM*QF**2/(8D0*XW*XW1)*
     &       (1D0-RM1)**2*(2D0+RM1)
            WID2=WIDS(23,2)
          ELSEIF(I.EQ.3) THEN
C...mu* -> W- + nu.
            WDTP(I)=FAC*AEM*RTCM(43)**2/(16D0*XW)*
     &       (1D0-RM1)**2*(2D0+RM1)
            IF(KFLR.GT.0) WID2=WIDS(24,3)
            IF(KFLR.LT.0) WID2=WIDS(24,2)
          ENDIF
          WDTP(I)=FUDGE*WDTP(I)
          WDTP(0)=WDTP(0)+WDTP(I)
          IF(MDME(IDC,1).GT.0) THEN
            WDTE(I,MDME(IDC,1))=WDTP(I)*WID2
            WDTE(0,MDME(IDC,1))=WDTE(0,MDME(IDC,1))
     &       +WDTE(I,MDME(IDC,1))
            WDTE(I,0)=WDTE(I,MDME(IDC,1))
            WDTE(0,0)=WDTE(0,0)+WDTE(I,0)
          ENDIF
 465      CONTINUE
```